UC Berkeley
UC Berkeley Previously Published Works

Title

Serpentinization as a Tape Recorder of (Dis)Continuous Mantle Exhumation along the Alpine Tethys Ocean-Continent-Transition

Permalink

https://escholarship.org/uc/item/2w616573

Journal

Journal of Petrology, 65(7)

ISSN

0022-3530

Authors

Hochscheid, Flora

Ulrich, Marc

Muñoz, Manuel

et al.

Publication Date

2024-07-01

DOI

10.1093/petrology/egae063

Peer reviewed

Serpentinization as a Tape Recorder of (Dis)Continuous Mantle Exhumation along the Alpine Tethys Ocean-Continent-Transition

FLORA HOCHSCHEID [iD][1,†,*], MARC ULRICH[1], MANUEL MUñOZ[2], PHILIPPE BOULVAIS[3] and GIANRETO MANATSCHAL[1]

[1]Institut Terre et Environnement de Strasbourg, Université de Strasbourg, CNRS UMR 7063, 5 rue Descartes, 67084 Strasbourg, France
[2]Géosciences Montpellier, Université de Montpellier, CNRS UMR 5243, Campus Triolet, 34095 Montpellier, France
[3]Géosciences Rennes, CNRS UMR 6118, Université de Rennes, 35000 Rennes, France

*Corresponding author address: Department of Earth and Planetary Science, University of California, Berkeley, CA 94720 USA E-mail: fhochscheid@berkeley.edu

Serpentinization has been widely documented and investigated at mid-ocean ridges (MOR) and subduction zones. In contrast, at magma-poor rifted margins serpentinization has received much less attention, despite its importance in controlling rheology and mass fluxes during breakup and establishing of a steady-state MOR. In this study, we present new petrological and geochemical data on subcontinental exhumed serpentinized peridotites from the spectacularly exposed Platta, Tasna and Totalp nappes in the Eastern Central Alps in SE Switzerland, belonging to the Alpine Tethys Ocean Continent Transition (OCT). The results testify of a complex history of fluid–rock interactions recorded by several serpentinization events starting with lizardite mesh and bastite textures (S1), subsequently followed by a succession of serpentine-filling veins with distinct textures and serpentine polysomes that include spherical polyhedral serpentine (S2); chrysotile ± polygonal ± lizardite banded veins (S3); lamellar antigorite veins and patches (S4) and chrysotile crack-seal (S5). The serpentinization sequence differs at proximal (i.e. continentwards) and distal (i.e. oceanwards) domains of the OCT. At proximal domains of the OCT (Upper Platta, Tasna) serpentinites record the complete serpentinization sequence (S1 to S5), whereas at distal domains (Lower Platta) serpentinization is restricted to pseudomorphic mesh and bastite (S1) and chrysotile crack-seal (S5). We attribute this discrepancy to contrasted mechanisms of mantle exhumation along the OCT. While at proximal domains mantle is unroofed along continuous and single large offset detachment faults allowing for the formation of all serpentine generations, mantle exhumation at distal domains is a more discontinuous process, controlled by sequential out-of-sequence detachment and flip-flop faults preventing the full development of all serpentine generations. In this frame, the nature and order of formation of the serpentine polysomes are directly controlled by the conditions of serpentinization (i.e. temperature, mantle composition and fluid/rock ratio). We propose that this new conceptual model can be extrapolated to serpentinization at slow to ultra-slow MORs, where close similarities in the serpentinization sequences have been recently reported.

Key words: serpentinization; magma-poor rifted margin; mantle exhumation; serpentine geochemistry; fluid–rock interaction

INTRODUCTION

At slow and ultra-slow spreading ridges (<40 mm•yr^{-1}), mantle peridotites are either exhumed at the seafloor along large offset normal faults, also referred to as detachment faults (Karson & Rona, 1990; Cannat, 1993; Cann *et al.*, 1997; Lavier *et al.*, 1999; Smith *et al.*, 2006), or flip-flop faults (Sauter *et al.*, 2013). Mantle exhumation at MORs is closely linked to hydrothermal activity that significantly modifies the mineralogy of mantle peridotites, turning them into serpentinites (e.g. Bonatti, 1968; Aumento & Loubat, 1971; Früh-Green *et al.*, 1990, 1996; Paulick *et al.*, 2006; Bach *et al.*, 2004, 2006; Schwarzenbach *et al.*, 2016, 2021). The serpentinization process stores about 13 wt % H$_2$O, leading to a strong volume expansion (up to ~40%, O'Hanley, 1992; Klein & Roux, 2020), and a density drop from 3.3 to 2.6 g•cm^{-3}. Serpentinization also results in strain localization along faults and the subsequent rapid exhumation from depths of 3 to 4 km to the seafloor (Raleigh & Paterson, 1965; Christensen, 1972, 2004; Reinen *et al.*, 1994; Escartin *et al.*, 1997, 2001; Morrow *et al.*, 2000).

While serpentinization and mantle-fluid interactions at Mid-Ocean Ridges (MORs) were largely documented over the past two decades, at magma-poor Ocean-Continent Transitions (OCT) these processes remain less well understood, despite the ubiquity of serpentinites at these settings. The presence of serpentinites at OCTs was first proposed from the Apennines (Boccaletti *et al.*, 1971) before it has been proofed along the Iberia margin (ODP Leg 103, Boillot *et al.*, 1980, 1989). Since then, more and more occurrences have been reported and described from present-day OCTs (Agrinier *et al.*, 1996; Albers *et al.*, 2021; Beslier *et al.*, 2004; Bonatti, 1976; Hopkinson *et al.*, 2004; Kodolányi *et al.*, 2012; Nicholls *et al.*, 1981) as well as from fossil examples (Lagabrielle & Bodinier, 2008; Manatschal & Müntener, 2009; Picazo *et al.*, 2013). At present, it is assumed that ~50% of the world rifted margins are formed by serpentinized exhumed mantle (Minshull, 2009).

Similar to MOR settings, serpentinization plays also at OCTs a key-role during mantle exhumation (e.g. Whitmarsh *et al.*, 2001; Gillard *et al.*, 2019). However, the nature of the mantle strongly differs between the two settings: while lherzolites are common in OCTs, harzburgites are dominant in MORs. How far the more fertile, pyroxene-rich composition of the mantle at OCTs controls the serpentization pathways and the nature of secondary mineral phases is yet little understood and will be discussed in this

paper. Previous studies have demonstrated that temperature of serpentinization also differs between OCTs and MORs. At slow spreading centers, seawater-mantle interaction takes place in the range of 200°C to 400°C (e.g. Früh-Green *et al.,* 2004; Barnes *et al.,* 2009; Vesin *et al.,* 2024), while serpentinization at OCT is assumed to occur at T < 250°C (Agrinier *et al.,* 1996; Schwarzen-bach *et al.,* 2013, 2016; Vesin *et al.,* 2023). This discrepancy is mainly attributed to the presence of punctual gabbroic intrusions in the mantle section at slow spreading centers that significantly increase the local geothermal gradient that can range between 45 and 150°C•km^{-1} (Bach *et al.,* 2011; Cannat *et al.,* 2019). At OCTs, the volume of intrusive magma increases oceanward, suggesting that the thermal gradient increases in the same direction reaching at its oceanward termination similar conditions like those at ultraslow MORs (Cannat *et al.,* 2009, 2019). The extent of serpentinization is likely controlled by access of seawater at depth, which is influenced by the presence or absence of magma. Low temperature of serpentinization was estimated from samples from the Iberia Abyssal Plain OCT (60–190°C, e.g. Agrinier *et al.,* 1996; Vesin *et al.,* 2023) and the Newfoundland OCT (100–130°C, Vesin *et al.,* 2023). Higher temperatures of serpentinization were primary reported at the MAR (>350°, e.g. Agrinier & Cannat, 1997), but recent in-situ oxygen data in MOR serpentinites indicate lower temperatures (~290 and 115°C; Vesin *et al.,* 2024). These new temperatures only partly cover the range of those expected at OCTs. As the mantle composition, geothermal gradients and depths of fluid penetration differ between OCTs and MORs, these two systems may record distinct histories of fluid–rock interaction, mass fluxes and deformation. However, to date, only very few studies looking more systematically at serpentinization reactions and sequences exist at OCTs.

The large variety of serpentine textures reported for MOR settings has been interpreted in terms of variation in the conditions and mechanisms of serpentinization, including temperature, fluid/rock ratio, fluid chemistry and/or tectonic unroofing (e.g. Dilek *et al.,* 1997; Andréani *et al.,* 2007; Rouméjon *et al.,* 2015, 2019). To date, detailed investigations of serpentine textures at magma-poor OCTs remain scarce and mostly incomplete, mainly due to the limited accessibility of the exhumed mantle in present-day OCTs and the complexity of restoring remnants of fossil OCTs emplaced in collisional orogens back to their pre-orogenic position (Albers *et al.,* 2021; Tichadou *et al.,* 2021).

In this study we investigate serpentinized peridotites from the Jurassic OCT of the Alpine Tethys realm now exposed in the southeastern Swiss Alps. We discuss the serpentine textures in terms of fluid/rock ratio, fluid chemical composition, mass fluxes and temperature conditions, and integrate the importance of tectonic modes during the exhumation of subcontinental mantle at the seafloor. We propose a conceptual model to explain serpentinization sequences at OCTs and discuss how our results can reconcile observations made at MORs.

GEOLOGICAL SETTING

Remnants of the Jurassic OCT of the Alpine Tethys are exposed as so called ophiolitic nappes in the Central Alps in southeastern Switzerland (Fig. 1A and C; Manatschal & Nievergelt, 1997; Müntener *et al.,* 2004, 2010). They represent remnants of the Adriatic-European conjugate margins (Fig. 1B; Florineth & Froitzheim, 1994; Manatschal, 2004). In our study, we focus on three sites, the Platta and Totalp nappes, both deriving from the SE OCT of the Adriatic margin, and the Tasna nappe, which derives from

the conjugate European margin (Manatschal & Müntener, 2009; Fig. 1).

The Platta nappe

The Platta nappe belongs to the lower Austro-Alpine and South Pennine nappe stack that was emplaced during Late Cretaceous along top to the NW thrust faults (Fig. 1C). The Platta nappe is subdivided into two units separated by a main reactivated pre-Alpine shear zone (Fig. 1D; Epin *et al.,* 2019). The Upper Platta Unit, in the hanging wall, was originally located in a more proximal position in the OCT (Fig. 1D). This unit consists of mantle rocks (the Upper Serpentinite Unit; Fig. 2A) derived from the inherited subcontinental Adriatic mantle (i.e. Schaltegger *et al.,* 2002; Müntener *et al.,* 2004, 2010; Picazo *et al.,* 2016; Epin *et al.,* 2019). The Lower Platta Unit, in the footwall of the main shear zone, was originally located in a more distal position (Fig. 1D). This unit consists of a large mantle domain (i.e. the Lower Serpentinite Unit, Fig. 2A) locally intruded by gabbros dated at 161 ± 1 Ma (Schaltegger *et al.,* 2002) and covered by lavas of late Middle to early Late Jurassic age (165 to ~155 Ma; Desmurs *et al.,* 2001; Amann *et al.,* 2020). Contrarily to peridotites from the Upper Platta Unit that are almost free from any syn-exhumation melt imprint and equilibrated at ~920°C, peridotites from the Lower Platta Unit have been largely percolated by MORB-type melts during final rifting and breakup, leading to a significantly higher equilibrium temperature of 1100 ± 50°C (Müntener *et al.,* 2010). Slivers of continental origin also occur in the Platta nappe and have been interpreted as extensional allochthons (Froitzheim & Manatschal, 1996). Mantle rocks in the Platta nappe display ophicalcites at their contact with mafic rocks and deep-water sediments (Fig. 2C; Dietrich, 1970, Coltat *et al.,* 2021), and were weakly affected by Alpine metamorphism (lower greenschist facies, <350°C; Trommsdorff & BW, 1974, Frey & Ferreiro Mählmann, 1999, Coltat *et al.,* 2021). However, an increase in Alpine metamorphism from north to south is documented by the transition from lizardite-chrysotile to antigorite. In the northern Platta nappe, temperatures were assumed to remain below 150°C, whereas in the Malenco nappe, south of the Engadine line, temperatures reached up to 400°C (Fig. 1C; Dietrich, 1969; Trommsdorff & Evans, 1977; Trommsdorff, 1983; Burkhard & O'Neil, 1988; Vils *et al.,* 2011).

The Totalp nappe

The Totalp nappe is located to the north of the Platta nappe (Fig. 1B). It belongs to the Late Cretaceous Upper Austro-Alpine and South Pennine nappe stack that was thrust northward over the Middle and Lower Pennine units during the late Eocene, (Froitzheim & Manatschal, 1996; Fig. 1C). The slightly more complex polyphase Alpine tectonic overprint makes that its position in the former OCT is less well defined than that of the Platta nappe. However, there is consensus in admitting that the Totalp nappe is derived from the SE OCT of the Alpine Tethys (Weissert & Bernoulli, 1985). The Totalp nappe consists of serpentinized spinel lherzolites, locally containing pyroxenites and ophicalcites, resulting from the carbonation of serpentine under static conditions at the seafloor. The ophicalcites preserve depositional contacts with Upper Jurassic to Lower Cretaceous pelagic sediments (Fig. 3; Picazo *et al.,* 2013). Magmatic rocks are very rare and mainly consist of flaser gabbros and dolerite dykes (Peters & Mathews, 1963). The Alpine metamorphic overprint is below prehnite pumpellyite facies at around 250°C (Peters, 1965). Serpentinized mantle is often crosscut by calcite veins, and similarly to the Platta nappe, relics of the pre-Alpine contacts between exhumed mantle rocks, ophicalcites and deep-water sediments are locally
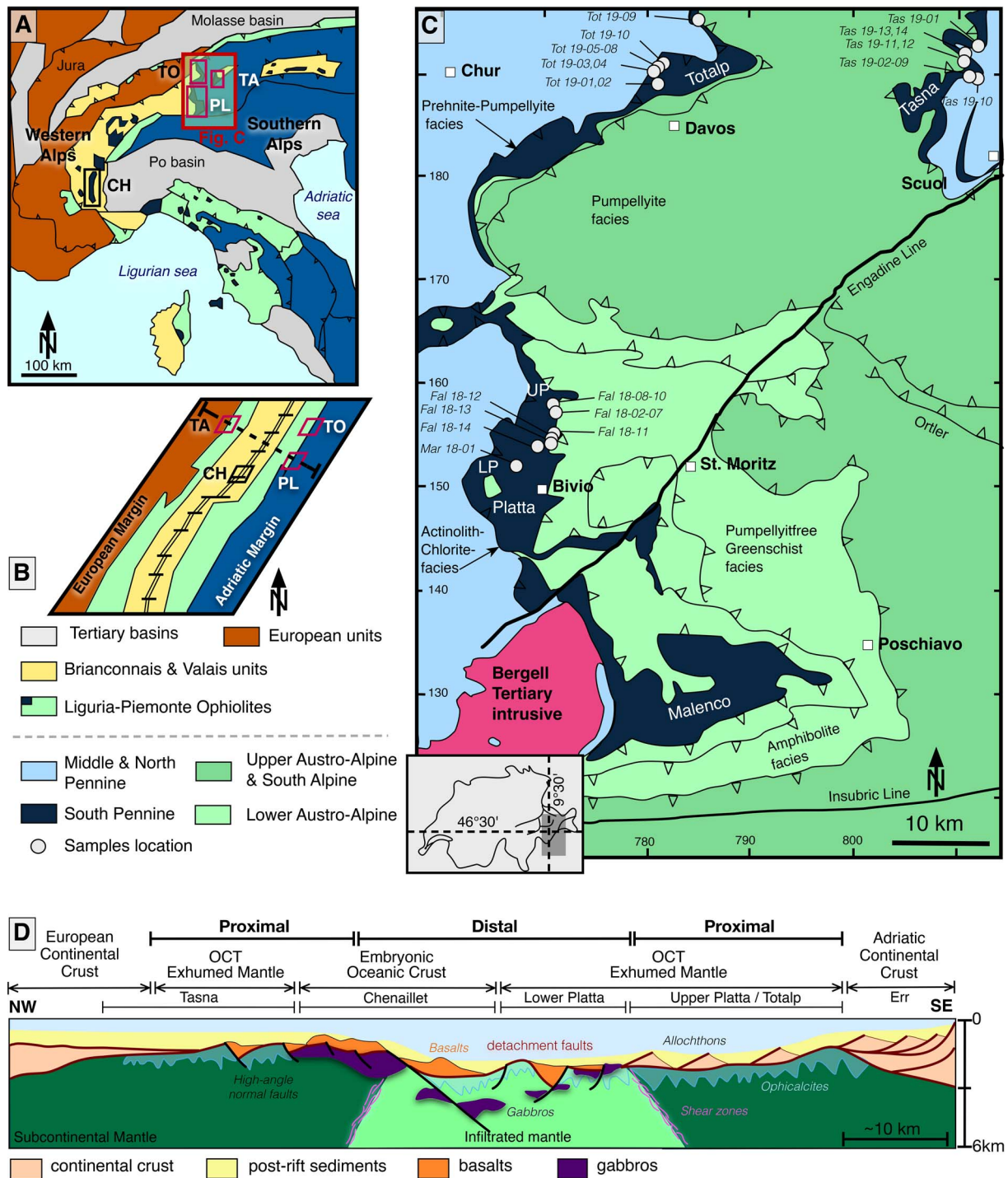
Fig. 1. (A) Present-day location of ophiolitic units of the Central–Western Alps and Apennines (modified after Manatschal & Müntener, 2009). (B) Schematic reconstruction of the Piemonte–Ligurian oceanic basin at Late Jurassic time, with the location of the major ophiolitic sequences (modified after Manatschal & Müntener, 2009). (C) Simplified geological map of the Pennine and Austro-Alpine nappes showing sample locations (modified after Froitzheim et al., 1994). D) Distribution of subcontinental and infiltrated mantle domains along the ocean-continent-transition of the Alpine Tethys (modified after Müntener & Piccardo, 2004). CH, Chenaillet; PL, Platta; TA,: Tasna; TO, Totalp.

well-preserved (Bernoulli & Weissert, 1985; Weissert & Bernoulli, 1985; Picazo et al., 2013). Results from $^{40}Ar/^{39}Ar$ dating on phlogopite from pyroxenites gave a cooling temperature $\leq 300°C$ and exhumation age of 160 ± 8 Ma (Peters & Stettler, 1987a, 1987b).

The Tasna nappe

The Tasna nappe was derived from the European OCT (Fig. 1B; Florineth & Froitzheim, 1994; Manatschal et al., 2006; Ribes et al.,

2020). It belongs to the Tertiary Alpine nappe stack made of Austro-Alpine and Pennine units (Fig. 1C) emplaced during the Eocene to Oligocene (Ribes et al., 2020). As for the Platta and Total nappes, the Tasna nappe exposes primary contacts between exhumed and serpentinized mantle rocks and sediments (Fig. 3). The Alpine metamorphism did not exceed 350°C (greenschist facies; Florineth & Froitzheim, 1994; Bousquet et al., 2008). The Tasna nappe is made of a wedge of continental crust separated
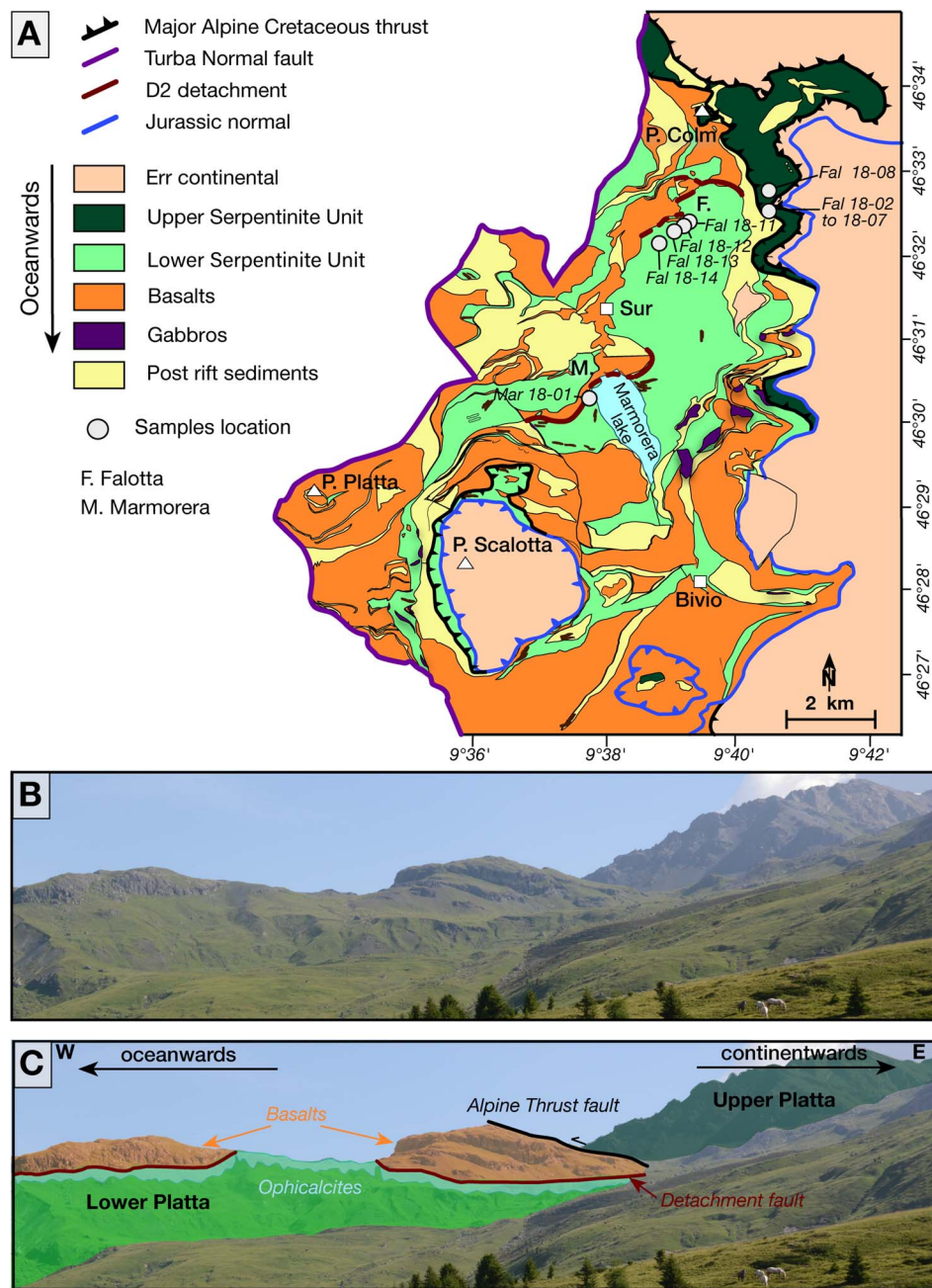
Fig. 2. (A) Geological map of the Platta nappe with sample locations (modified after Schaltegger *et al.*, 2002). (B) Photograph of the Falotta area, and (C) interpretative drawing of the Falotta area showing the various lithologies and their respective structural relations (the basalts overlie the lower Platta Unit made of serpentinized mantle separated by a rift-related detachment surface.

from the underlying mantle by a detachment fault, referred to as the Lower Tasna Detachment (LTD; Froitzheim & Rubatto, 1998, Fig. 4C).a The Upper Tasna Detachment (UTD) is the top-basement fault responsible for the exhumation of the crust and mantle rocks at the seafloor (Froitzheim & Rubatto, 1998, Manatschal et al., 2004, 2006). It is overlain by the undeformed post-rift sediments (Fig. 4C) interpreted as Upper Jurassic (Ribes *et al.*, 2020). Mantle rocks consist of highly serpentinized spinel lherzolites with abundant spinel websterite layers and preserving a high temperature foliation marked by spinel grains (Manatschal *et al.*, 2006). The $^{40}Ar/^{39}Ar$ dating of phlogopite provides an age of 170.5 ± 0.4 Ma (Manatschal *et al.*, 2006), similar to that obtained for mantle exhumation at Totalp (160 ± 8 Ma; Peters & Stettler, 1987a).

The clinopyroxene compositions and the calculated equilibrium temperatures of mantle peridotites from Tasna are similar to those from the Upper Platta unit and Totalp, demonstrating that all of these ultramafic units belonged to the same, inherited mantle domain (Manatschal *et al.*, 2006; Picazo *et al.*, 2016).

MATERIALS AND METHODS
Sampling and analytical strategies
A total of 40 moderately to completely serpentinized peridotites have been sampled (Table 1). The sampling was done with the aim of characterizing fluid–rock interactions at the two opposed positions along the OCT of the former Alpine Tethys, i.e. at the proximal domain (continentwards, Upper Platta, Tasna and Totalp) and
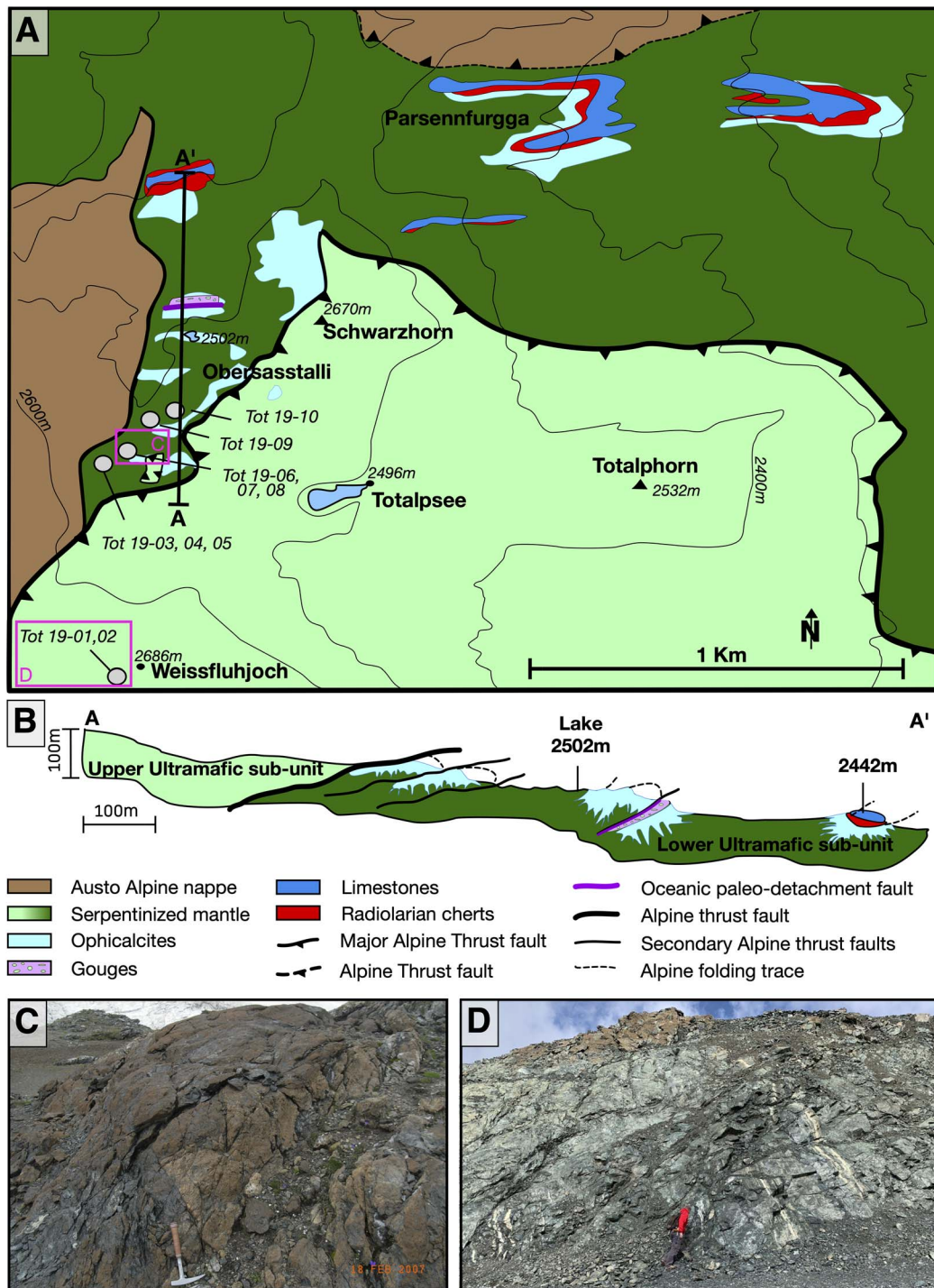
Fig. 3. (A) Geological map of the Totalp area with sample locations (modified after Picazo *et al.,* 2013). (B) South–north oriented cross-section across the Totalp area showing Alpine thrusts and folds. (C) Photograph of massive serpentinite outcrop. D) Photograph of the serpentinite wall near Weissfluhjoch (samples Tot 19–01,02).

the distal domain (oceanwards, Lower Platta; Fig. 1D). A comprehensive set of petrographical and geochemical analyzes was performed on each sample, including: i) petrographic observations in thin sections; ii) X-ray diffraction, to identify minerals and their respective proportions in serpentinites; iii) bulk-rock major and trace element analyses. Among the samples, 18 were selected for: i) Raman spectroscopy to identify serpentine polysomes, and ii) in situ major and trace element analyses to constrain fluid–rock interactions during mantle exhumation.

X-ray diffraction

XRD analyses were performed on sample powders using a Bruker D8 advance Eco diffractometer at the Institut Terre et Environnement de Strasbourg (ITES, University of Strasbourg). A large X-ray beam was emitted by a copper source with a 40-kV accelerating voltage and a 25-mA current. Intensities were recorded at 0.014° 2θ step intervals from 3 to 80° 2θ, with a dwell time of 0.8 s. Size of the divergence slit was 0.4°. Table 1 provides the quantitative mineralogical compositions determined by Rietveld refinement using Profex-BGMN software (Doebelin & Kleeberg, 2015),

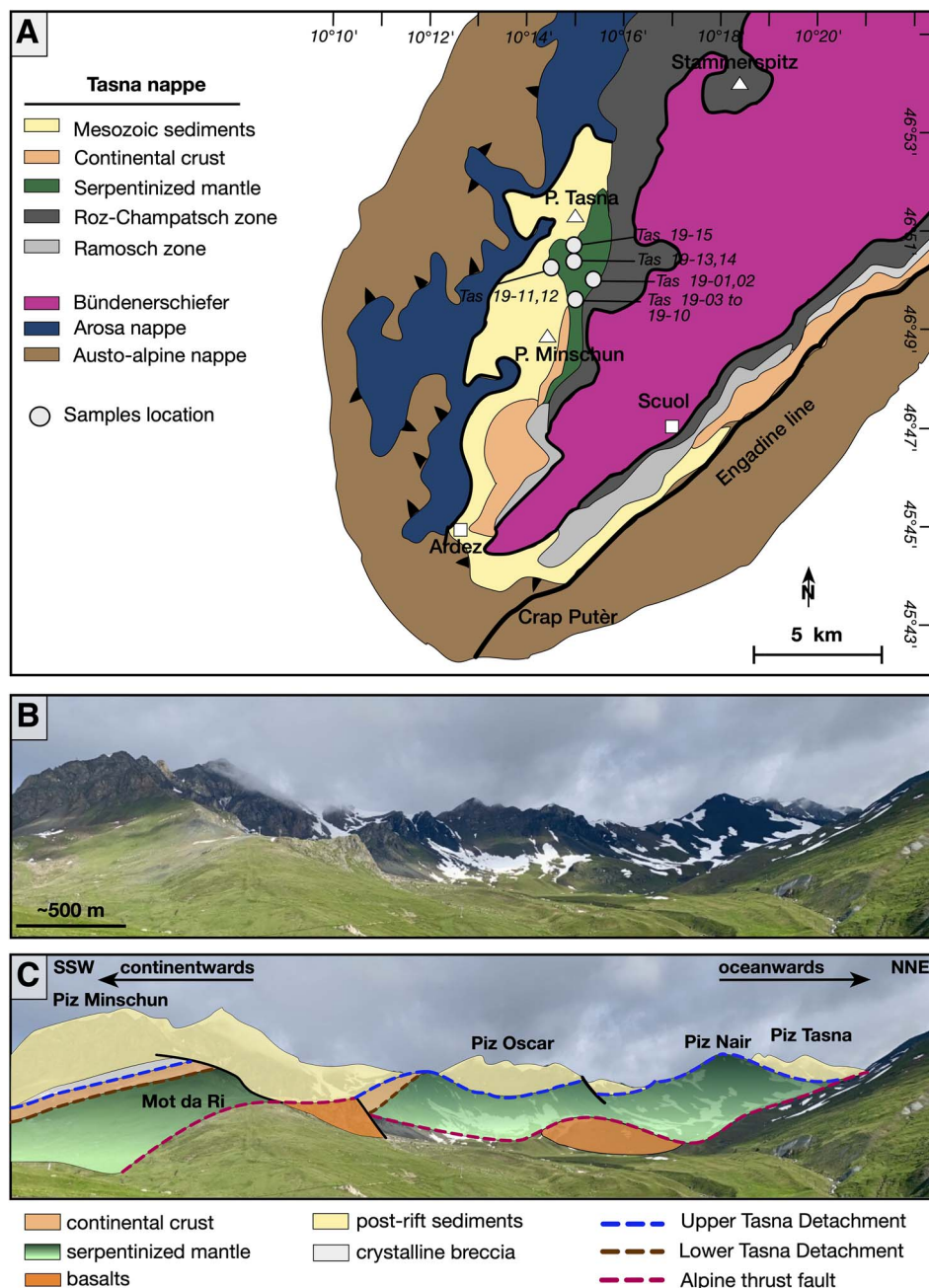**Fig. 4.** (A) Simplified geological map of the western Engadine window in SE Switzerland and Austria and location of the Tasna nappe (modified after Trümpy & Dössegger, 1972; Florineth & Froitzheim, 1994; Manatschal et al., 2006). (B) Panoramic view of the Tasna Ocean–Continent Zone. (C) Geological interpretation of the Tasna area showing the serpentinized mantle that is separated from the continental crust (in the SSW) and post-rift sediments (in the NNE) by rift-related detachment faults. The base of the mantle is an Alpine thrust fault (modified from Florineth & Froitzheim, 1994; Manatschal et al., 2006).

as well as the list of the reference structures used for refinement. The diffraction patterns, Rietveld refinements and the references of mineral structures used for the refinements are given in supplementary materials.

Raman spectroscopy

Raman spectra were acquired on 30 μm thick polished thin sections, using a HORIBA LabRAM ARAMIS spectrometer at the Laboratoire des sciences de l'ingénieur, de l'informatique et de l'imagerie (ICube, University of Strasbourg). A 100× objective (Olympus) and a 632-nm (Ar+) laser at 9 mW were used, resulting in a laser spot size of ~1 μm. All analyses were performed

using integration times of 15 or 30 s to optimize the signal/noise ratio. Raman spectra were recorded in two wavelength intervals: $100–1120$ cm^{-1} for structural bonding characterization and $3500–3750$ cm^{-1} for the characterization of hydroxyl bonds. The serpentine polysomes were identified by comparison with reference spectra taken from the literature, in particular on the stretching range of the OH groups (e.g. Auzende et al., 2004; Groppo et al., 2006; Tarling et al., 2018; Compagnoni et al., 2021).

Bulk-rock chemistry

The major element concentrations were measured on pressed pellets of calcined powder (i.e. after loss on ignition) using a micro-

Table 1: Location and description of the 40 serpentinized peridotites and serpentinites from the Eastern central Alps analyzed in this study

Unit Rietveld references	Sample	Texture	Latitude	Longitude	Srp chrysotile 2 M1 ICCD, lizardite 1 T Mellini	Mag profex-BGMN database	Cal profex-BGMN database	Clc profex-BGMN database
Upper Platta	Fal 18-02a*	Vein	46°32'51.17"N	9°40'9.42'E	99.9	-	-	-
	Fal 18-02b	Massive + veins	46°32'51.17"N	9°40'9.42'E	97.8	1.8	<1	-
	Fal 18-03*	Massive	46°32'51.08"N	9°40'10.14"E	99.6	<1	<1	-
	Fal 18-04	Vein	46°32'51.12"N	9°40'9.94'E	99.9	-	-	-
	Fal 18-05	Vein	46°32'51.13"N	9°40'9.92'E	99.7	<1	-	-
	Fal 18-06*	Massive	46°32'51.25"N	9°40'10.02''E	95.0	5	<1	-
	Fal 18-07	Massive	46°32'51.25"N	9°40'10.02''E	81.0	1.3	-	-
	Fal 18-08	Massive + veins	46°32'56.63"N	9°4'7.09''E	97.0	2.3	-	-
	Fal 18-09	Massive	46°32'56.63"N	9°4'7.09''E	99.8	<1	-	-
	Fal 18-10	Massive + veins	46°32'56.63"N	9°4'7.09''E	98.9	1.1	-	-
Lower Platta	Fal 18-11*	Massive	46°32'44.74"N	9°39'38.65''E	99.3	<1	-	-
	Fal 18-12	Massive	46°32'43.75"N	9°39'33.72''E	85.7	<1	1.6	8.1
	Fal 18-13*	Massive	46°32'42.24"N	9°39'34.87''E	99.5	<1	<1	-
	Fal 18-14	Massive	46°32'29.95"N	9°39'40.02''E	99.9	<1	-	-
	Mar 18-01*	Massive + veins	46°30'19.19"N	9°37'41.28"E	98.8	1.2	<1	-
Totalp	Tot 19-01	Massive	46°49' 56.97" N	9°48' 18.71'' E	58.9	1	-	-
	Tot 19-02*	Massive	46°49' 56.97" N	9°48' 18.71'' E	91.1	-	-	-
	Tot 19-03a*	Massive + veins	46°50' 18.49" N	9°48' 13.85'' E	92.0	<1	-	-
	Tot 19-03b	Vein	46°50' 18.55" N	9°48' 13.94'' E	99.9	-	-	-
	Tot 19-04*	Massive + veins	46°50' 18.40" N	9°48' 14.23'' E	96.7	0.38	-	-
	Tot 19-05	Massive	46°50' 18.40" N	9°48' 14.23'' E	90.8	<1	-	-
	Tot 19-07*	Massive	46°50' 19.58" N	9°48' 16.68'' E				
	Tot 19-09*	Massive	46°54' 56.61" N	9°51' 27.98'' E	97.1	<1	-	-
	Tot 19-10a	Foliated	46°50' 23.31" N	9°48' 24.48'' E	95.9	<1	-	-
	Tot 19-10b*	Massive	46°50' 24.37" N	9°48' 26.62'' E	98.7	<1	<1	-
Tasna	Tas 19-01	Massive	46°50'17.28" N	10°15' 37.79' E	94.0	1.3	<1	-
	Tas 19-02*	Foliated	46°49' 24.33" N	10°15' 6.11'' E	98.7	<1	<1	-
	Tas 19-03*	Massive	46°49' 35.23" N	10°15' 4.26'' E	96.3	<1	<1	-
	Tas 19-04*	Massive + veins	46°49' 35.08" N	10°15' 4.12'' E	94.1	<1	<1	-
	Tas 19-06a	Vein	46°49' 34.70" N	10°15' 4.69'' E	99.9	-	-	-
	Tas 19-06b	Massive + veins	46°49' 34.70" N	10°15' 4.69'' E	98.2	<1	<1	-
	Tas 19-07	Vein	46°49' 34.73" N	10°15' 5.02'' E	99.9	-	-	-
	Tas 19-08*	Massive + veins	46°49' 34.59" N	10°15' 4.74'' E	99.4	<1	<1	-
	Tas 19-09	Vein	46°49' 34.38" N	10°15' 4.30'' E	99.9	-	-	-
	Tas 19-10*	Massive + viens	46°49' 27.28" N	10°16' 9.17'' E	98.5	<1	-	-
	Tas 19-11	Vein	46°49' 54.23" N	10°14' 56.57'' E	97.9	<1	-	-
	Tas 19-12	Massive	46°49' 54.06" N	10°14' 56.78'' E	98.7	<1	<1	-
	Tas 19-13	Massive	46°50' 0.71" N	10°15' 9.73'' E	99.7	<1	-	-
	Tas 19-14	Massive	46°50' 1.07'' N	10°15' 9.70'' E	90.1	<1	<1	-
	Tas 19-15	Massive	46°50' 1.07'' N	10°15' 9.70'' E	99.5	<1	-	-

Table 1: Continued

Adr profex-BGMN database	Tr profex-BGMN database	Ol Forsterite profex-BGMN database	Cpx diopside profex-BGMN database	Opx enstatite profex-BGMN database	Spl profex-BGMN database	Pseudomorphic textures	Veins texture	Antigorite
-	-	-	-	-	-	-	b, g, s	
-	-	-	-	-	<1	X	b	
-	-	-	-	-	-	X	b, g, l, s	
-	-	-	-	-	-	-	b	
-	-	-	-	-	-	-	b	
-	-	<1	-	-	<1	X	l, f	X
-	-	<1	10.9	6.1	<1	X	b, g	
-	-	-	-	-	-	-	b, g	
-	-	-	-	-	<1	X	f	
-	4.5	-	-	-	<1	X	b, g, f	
-	-	-	-	-	<1	X	f	
-	-	-	-	-	-	X	f	
-	-	-	-	-	<1	X	b, f, s	
-	-	-	-	-	<1	X	f	
-	-	-	-	-	-	X	b, l, f	X
2.3	-	30.2	7.6	2.2	<1	X	b, s	
3	-	<1	6.8	-	-	X	b, s	
-	-	-	3.5	<1	<1	X	b	
-	-	-	-	-	-	-	b	
-	-	<1	2.92	1.8	<1	X	b, s	
-	-	-	5.8	-	-	X	b, s	
-	-	-	-	-	-	X	b	
3.7	-	1.5	<1	-	<1	X	b, s	
-	-	-	-	-	-	X	s	
-	2.2	-	-	-	-	X	b, s	
-	-	-	-	-	-	X	b	
-	<1	<1	1.3	-	<1	X	b, g, f	X
<1	1.2	-	3.3	-	<1	X	b, g, f, s	
<1	-	-	-	-	-	X	b, g, l	X
-	-	-	-	-	-	-	b	
-	-	-	-	-	-	-	b	
-	-	-	-	-	-	X	-	
-	-	-	<1	-	-	-	b	
-	-	-	-	-	-	X	-	
-	-	-	-	-	-	-	b	
-	-	<1	2.7	-	<1	X	b, l, s	
-	-	-	-	-	<1	X	b, f, s	
-	-	-	<1	-	-	X	b, f	
-	-	2	6.7	-	-	X	b, f, s	X
-	-	-	-	-	-	X	b	

Mineral phases and their respective proportions (in wt %) were obtained by X-ray diffraction on sample powders and estimated by Rietveld refinement using Profex software (Doebelin et al., 2015). Srp, serpentine; Mgt, magnetite; Cc, calcite; Chl, chlorite; And, andradite; Tr, tremolite; Ol, olivine; Cpx, clinopyroxene; Opx, orthopyroxene; Spl, spinel; b, banded; f, fibrous; g, granular; l, lamellar; s, spherical. *Selected samples for detailed mineralogical and geochemical investigations.

X-ray fluorescence (μ-XRF) Bruker M4 Tornado at ITES. For each sample, 10 measurements were performed at random location on each pellet to ensure the reproducibility at the pellet surface. A collimated Rh source operating at 700 μA with an accelerating voltage of 50 kV was used, resulting in a 1-mm spot-size in diameter at the sample surface. Two energy-dispersive silicon drift detectors of 125 eV resolution, and with an active area of 60 mm^2 each were used to measure fluorescence spectra (300 s counting time per spectrum). Measurements were performed in a vacuum chamber at 2 mbar to minimize air absorption and ensure the best signal/noise ratio.

The bulk-rock trace element concentrations were determined at ITES using an Inductively Coupled Plasma Mass Spectrometry (ICP-MS) Thermo Scientific X series II instrument and ICAP RQ Thermo Scientific instrument. The analytical procedure was adapted from the method of Chauvel et al. (2011): about 100 mg of rock powder was precisely weighed and dissolved in Savillex beakers in a HF-HNO$_3$-HClO$_4$ (5:1:1) mixture, during a minimum of 7 days at 140°C on a hot plate. The solution was then evaporated, and the residue was taken in a 3:1 3 M HCl–H$_3$BO$_3$ mixture for 12 hours in a hot plate at 90°C to avoid any fluoride precipitation. This mixture was then evaporated and further dissolved in concentrated HNO$_3$. After another evaporation, the residue was finally diluted in 40 ml of 7 M HNO$_3$.

Analyzes performed on international standard are consistent with preferred reference values from GeoREM for UB-N serpentinite (Govindaraju, 1982). Differences between reference values from the literature and our analyses of UB-N are ±1.1% for all other major oxides except for Na$_2$O, K$_2$O, P$_2$O$_5$ and TiO$_2$ which are present in very low concentrations. For most trace element concentration, the deviation from the reference value of UB-N is in average ± 5% (see Supplementary Table S3).

Mineral chemistry

The major element concentrations were measured on 30 μm-thick polished sections using a μ-XRF Bruker M4 Tornado at ITES. Measurements were performed using a Rh anode operating at 400 μA with an accelerating voltage of 50 kV. Polycapillary lenses were used to focus the X-ray beam down to 20 μm full-width-at-half-maximum at the sample surface. The counting time per point was set to 180 s. μ-XRF spectra were calibrated after repeated analyses of Smithsonian National Museum of Natural History mineral standards (Jarosewich et al., 1980) of diopside (NMNH 117733) and San Carlos olivine (NMNH 111312–44), and some in-house mineral standards of clinochlore, chrysotile and antigorite. Total Fe content was calculated on a divalent basis, as FeO$_{tot}$.

The structural formulae for lizardite, chrysotile, polygonal and polyhedral serpentines was calculated on the basis of 7 oxygens. Antigorite has a distinct formula Mg$_{3m-3}$Si$_{2m}$O$_{5m}$(OH)$_{4m-6}$ that slightly differs from the idealized serpentine formula (Mg$_3$SiO$_5$(OH)$_4$), where m is the number of tetrahedra along an entire wavelength of the crystalline structure. Here, the structural formula of antigorite was calculated based on $m = 17$ (Mellini et al., 1987). The Fe^{2+} and Fe^{3+} contents of serpentine mineral were estimated following the approach of Ulrich et al. (2020) based on the initial study of Beard & Frost (2017). The calculations assume a full dioctahedral substitution, i.e. ferric iron is accommodated in the serpentine by substitution for divalent cation plus the addition of a vacancy in the octahedral sheet.

Serpentine trace element compositions were acquired on 30 μm polished thin sections by laser ablation inductively coupled plasma mass spectrometry (LA-ICP-MS) at Géosciences Montpellier (University of Montpellier, AETE regional facility of the OSU OREME). The instrument includes a pulsed 193 nm ArF excimer laser (Compex 102 instrument from LambdaPhysik) coupled to a ThermoScientific Element XR mass spectrometer. Laser ablation was performed with an energy density of 12 J/cm^2 at a frequency of 6 Hz. Few laser pulses with a spot size of 130 μm were applied before each ablation to clean up the sample surface. Then each acquisition was performed with a total of 240 pulses with a spot size of 110 μm, sufficient to obtain a long and stable signal for integration. The ablated material was transported using a constant He flow of 1 l/min and mixed with Ar flow of 0.6 l/min in a cyclone coaxial mixer before entering the ICP torch and being ionized. The ions are then sampled, accelerated and focused before being separated and analyzed in the mass spectrometer. ^{29}Si content known from prior μ-XRF analyses were used as internal standard and concentrations were calibrated against the NIST 612 rhyolitic glass using reference values from Pearce et al., 1997. In order to evaluate the precision of the measurements the reference basalt glass BIR-1G was analyzed repeatedly each 5 samples to (the complete dataset, including standard reference values, is available in supplementary materials). Data reduction was operated with Matlab-based SILLS program (Guillong et al., 2008), following the standard methods of Pettke et al. (2012). Detection limits were between 1 ppb and <0.3 ppm for most trace elements.

RESULTS
Petrographic description

All samples analyzed in this study derived from the proximal domain (Tasna, Totalp and Upper Platta) are spinel-lherzolites, while those from the distal domain (Lower Platta) are dominantly plagioclase-bearing lherzolites. Macroscopically, all samples are extensively serpentinized (Fig. 5). This is confirmed by microscopic observations (Fig. 6) and Rietveld refinements made on X-Ray diffraction patterns (Table 1), showing that most of the samples contain ~96% (n = 40) serpentine. Rare exceptions were found at Tasna and mostly Totalp, where relics of primary clinopyroxene and more occasionally olivine are preserved.

The serpentinites from the Lower and Upper Platta nappe are typically of a dark green color (Massive serpentinite; Fig. 5A). Serpentinites from the Lower Platta, display rare imprint of several serpentine veins. Some serpentinites contain clasts of massive dark serpentinite that are locally embedded in a fibrous and light-green colored serpentine matrix (Fig. 5B). For the Upper Platta (proximal domain) serpentinites are occasionally crosscut by centimeter-thick light green serpentine veins (Fig. 5A), and most samples are characterized by several generations of serpentine veins (Fig. 5C). At Tasna (Fig. 5D, E) and Totalp (Fig. 5F), massive serpentinites are locally surrounded by a late foliated serpentinite, characterized by a light blueish color and a fibrous aspect. At Totalp, some relics of primary minerals are present, like olivine in the center of mesh texture (Fig. 5G) or clinopyroxene in massive dark serpentinite (Fig. 5H). It should be noted that some samples contain minute amounts of calcite (<1%, Table 1) when picked up in the vicinity of ophicalcites (e.g. Picazo et al., 2013).

Based on microscopic observations and Raman spectra made on thin sections, we firstly described the textures and determined the polysomes of serpentine. Secondly, we attributed the succession of serpentine to a sequential evolution regarding the position along the OCT, i.e. proximal and distal domains.
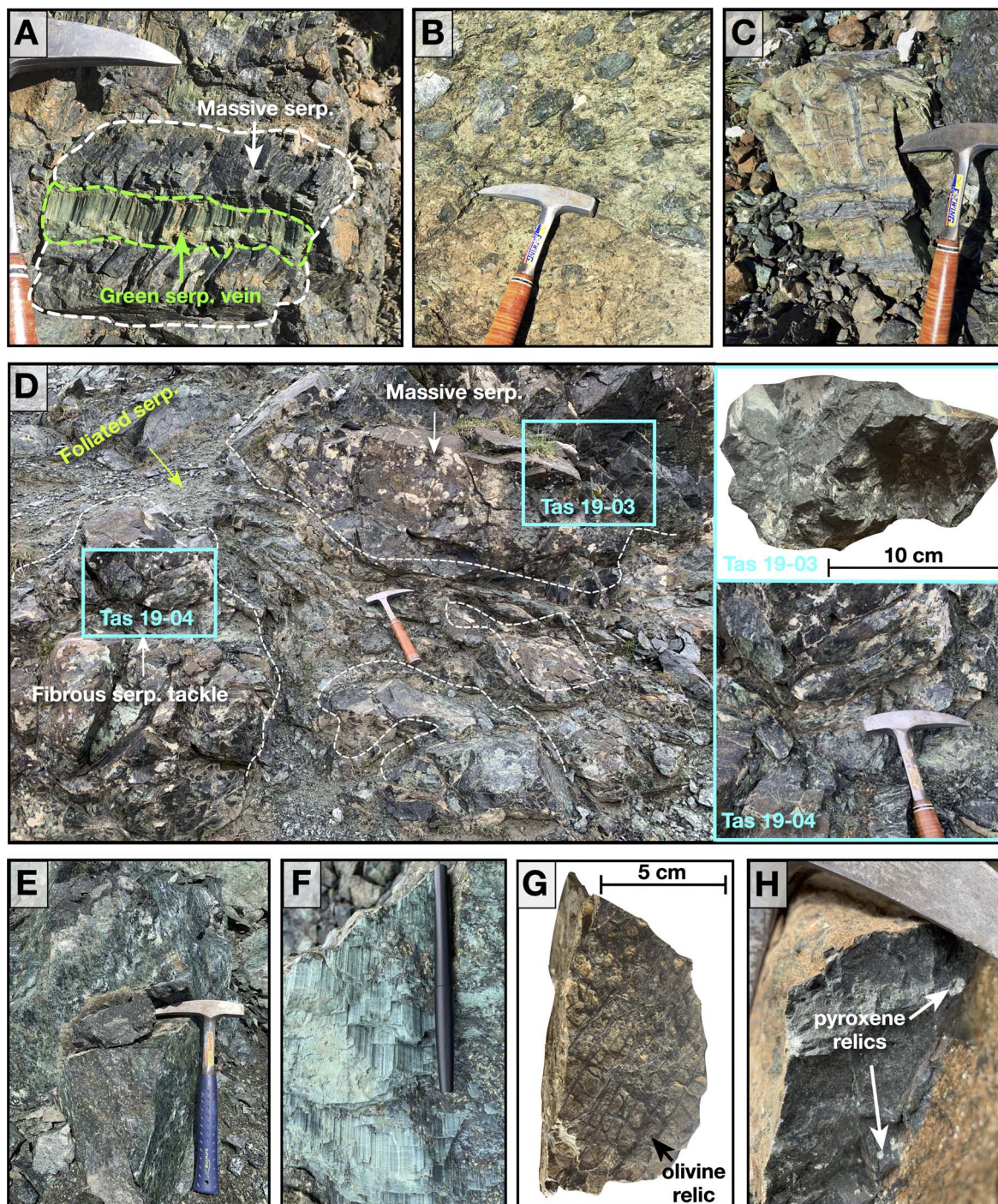
Fig. 5. Representative photographs of the diversity of textures in serpentinites sampled in the three distinct sites (Platta, Totalp, Tasna). (A) Massive dark green serpentinite crosscut by a fibrous serpentine vein of pale green color (Fal 18-02, Upper Platta unit). (B) Clasts of massive dark serpentinite embedded in a serpentine matrix of a fibrous texture (Fal 18-12, Lower Platta Unit). (C) Green serpentinite crosscut by several generations of thick dark and thin green pale serpentine veins (Fal 18-08, Upper Platta unit). (D) Massive dark green serpentinite (Tas 19-03) surrounded by a foliated pale green fibrous serpentinite (Tas 19-04, Tasna Unit). (E) Massive green serpentinite from Totalp (Tot 19–01). (F) Blueish serpentine fibers (Tot 19-04). (G) Massive serpentinite sample crosscut by thick dark serpentine veins forming a mesh texture (Tot 19-05, Totalp Unit). (H) Pyroxene relics in a massive dark green serpentinite (Tot 19-09).

Serpentine mesh and bastite textures S1

Serpentine mesh and bastite textures constitute the bulk and first generation of serpentinization in most samples from all domains. They correspond to the pseudomorphic replacement of olivine and pyroxenes by serpentine mesh (Fig. 6 A, B) and bastite textures (Fig. 6 C, D). Some relics of primary minerals, especially clinopyroxene and to a lesser extent olivine, can be occasionally preserved in samples from Totalp (Fig. 6B, E). In these samples, olivine is preserved within the mesh network and hydration of clinopyroxene has progressed with the development of serpentine veins along cleavages. Orthopyroxene relics are scarcely observed in our samples, at the opposite of spinel grains which are preserved even in the most serpentinized samples and only show minor evidence of hydrothermal alteration with the
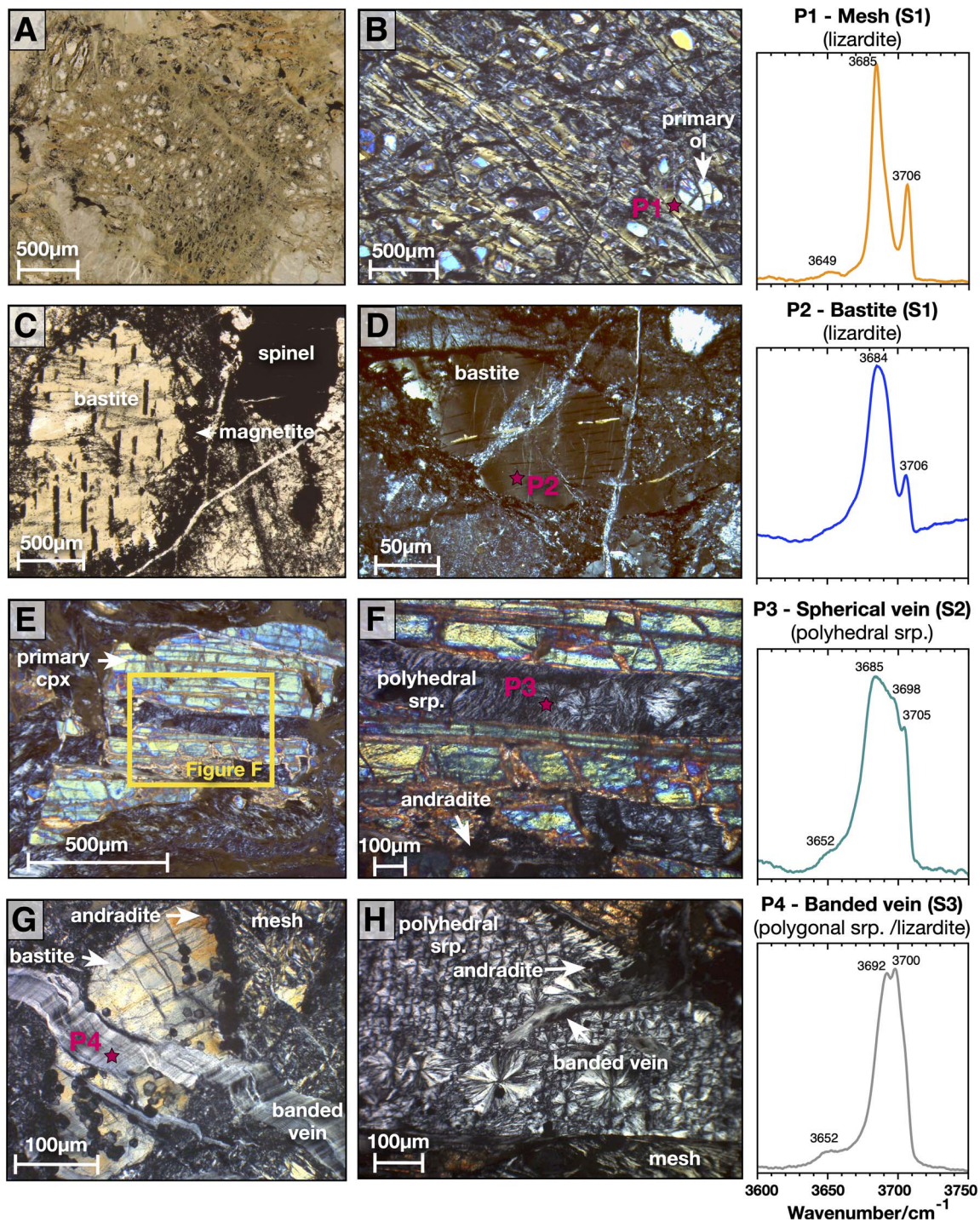
Fig. 6. Photomicrographs of serpentinite thin sections showing the diversity of serpentine textures and their respective Raman spectra. P, point where the Raman spectra was done. All photos were taken under plane-polarized light (PPL; A, C) or cross-polarized light (XPL; B, D to H). (A–B) First generation of serpentine (S1) made of lizardite, forming a typical mesh texture replacing olivine grains, or (C) Bastite texture replacing primary pyroxene associated with magnetite grains. (D) Bastite under XPL, cut by serpentine veins. (E) Second generation of serpentine formed of polyhedral serpentine (S2) in clinopyroxene cleavage. (F) Focus on S2 serpentine vein in clinopyroxene cleavage showing the close association of this serpentine polysome and the formation of andradite grains. (G) Third generation of serpentine (S3) with a typical banded vein texture made of polygonal serpentine crosscutting the bastite and mesh textures (S1). (H) Polyhedral serpentine (S2) and andradite at rims of bastite (S1), cut by a banded vein (S3).

local formation of chlorite aureoles. The dominant serpentine polysome is lizardite, as shown by the typical OH stretching bands at 3685 cm^{-1} and 3707 cm^{-1} on Raman spectra (Fig. 6). In all these samples, magnetite is ubiquitous, with amounts between 0.38 and 5% (Table 1). Magnetite mainly occurs as small grains (<5 μm) disseminated along the mesh rims, and also observed in cleavages and surrounding the bastite grains (Figs. 5 and 6C).

Serpentine veins

The background mesh and bastite textures (S1, lizardite type) are usually crosscut by at least one generation of serpentine veins in
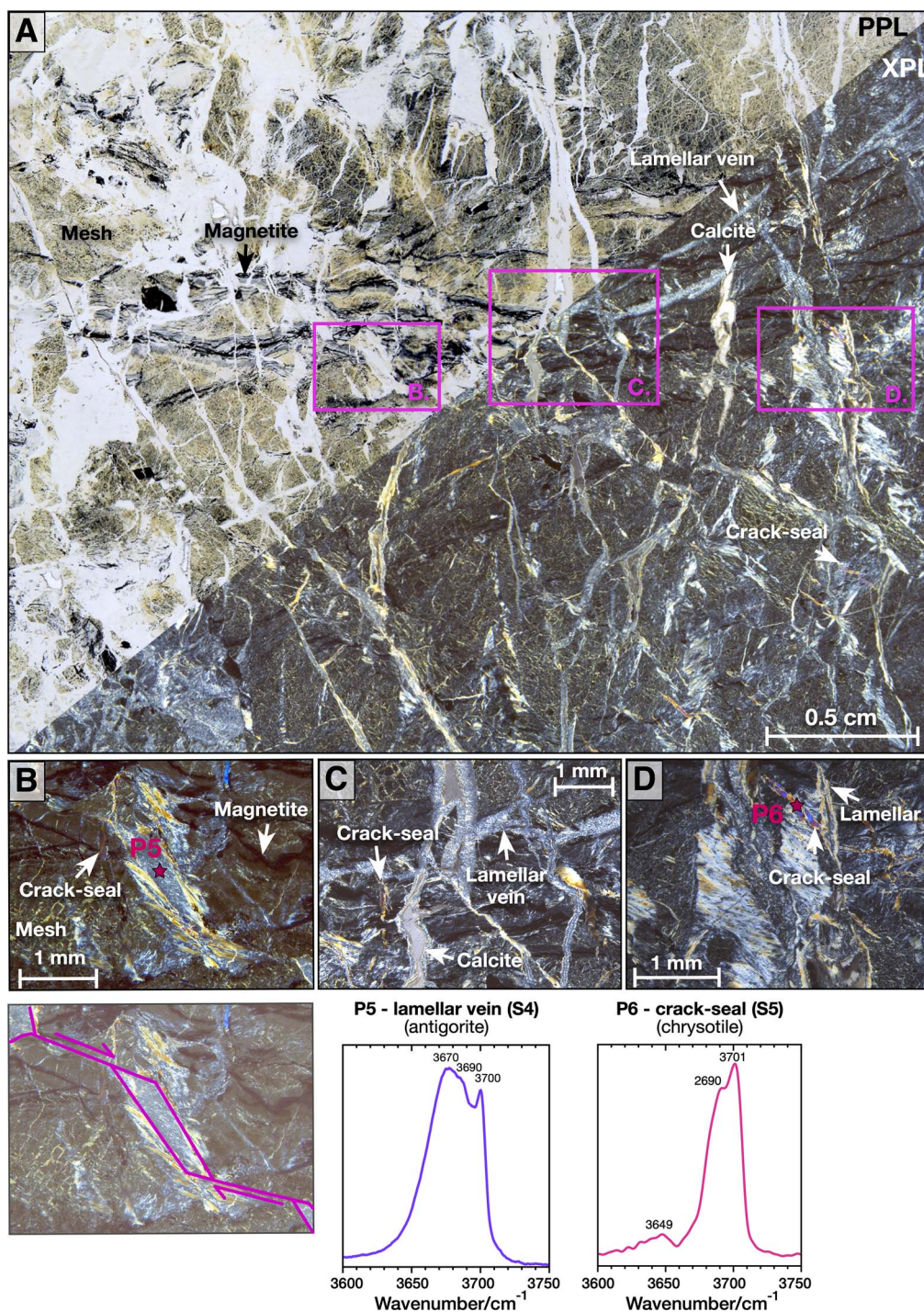
Fig. 7. (A) Microphotography under plane polarized ligth (PPL) and cross polarized light (XPL) of a serpentinite sample from the lower Platta unit (Fal 18–06) showing the primary mesh texture (S1) crosscut by successive generations of serpentine veins. (B) Focus on the primary serpentine mesh (S1) and associated magnetite grains crosscut by a thick fracture opened in pull-apart mode and filled by antigorite (S4) with a typical lamellar texture. (C–D) Focus of (A) showing the chronology of formation of serpentine polysomes between lizardite mesh (S1), lamellar antigorite vein (S4), chrysotile crack-seal (S5) and late calcite veins.

the distal domain, and usually several generations of serpentine veins in the proximal domain. We have identified four main generations of serpentine veins representing a serpentinization sequence.

Spherical serpentine (S2): The second generation of serpentine, here referred to as 'spherical serpentine S2', was occasionally observed in partially serpentinized samples from Totalp and Tasna and barely in fully serpentinized samples from Upper Platta. It forms a typical spherical texture that is characterized in microscopic view in crossed-polarized light by an extinction cross in the polarization directions (Fig. 6 E, F, H). Such typical spherical texture and the Raman signature (Fig. 6) are robust features in favor of a polyhedral serpentine. This serpentine polysome occurs in a few of our samples, mainly in clinopyroxene cleavages (Fig. 6E, F) and occasionally as veins crosscutting the previous serpentine mesh and bastite S1 (Fig. 6H). The occurrence
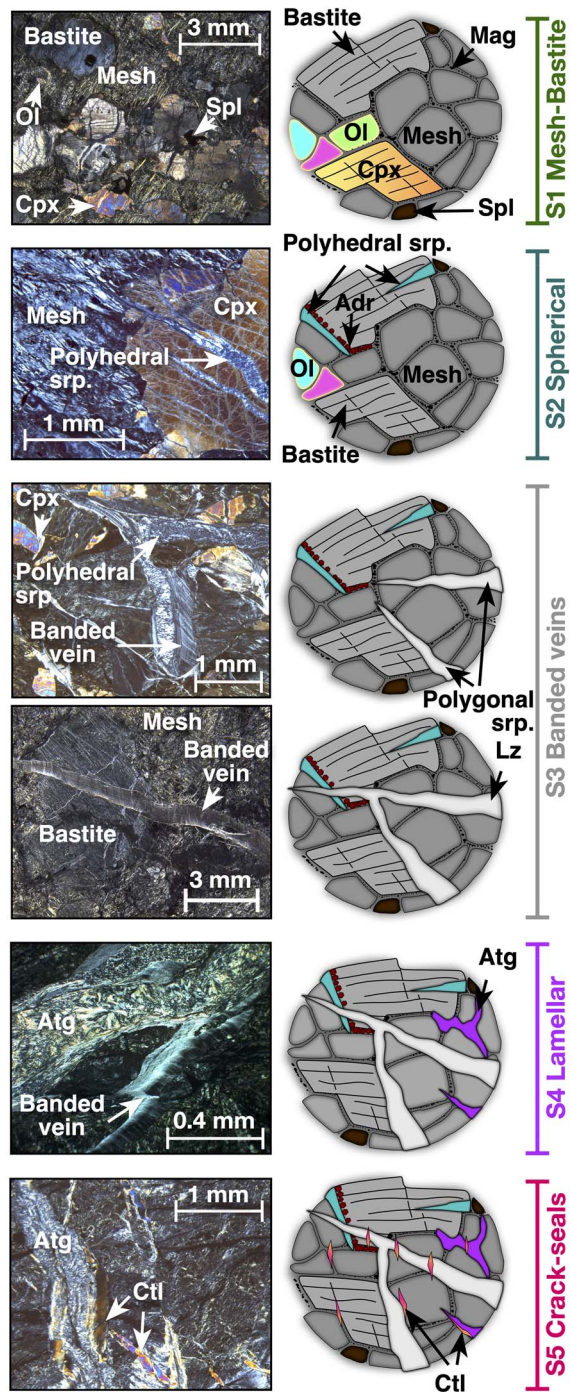
Fig. 8. Representative microphotographs and schematical representations of the five different types of serpentines described in this study.

of small andradite grains (~10 μm diameter) is closely associated to polyhedral serpentine veins, almost exclusively at the vicinity of clinopyroxenes (Fig. 6F, H).

Banded veins (S3): The third generation of serpentine (S3, Fig. 6G), is usually observed in serpentinites from proximal domains and very sparsely and rarely in serpentinites from the distal part (Lower Platta). It consists of veins ranging from tens of μm- to cm-thick. The centimetric veins are observable at the macroscopic scale and are characterized by a fibrous green texture (e.g. Fig. 5A). These veins are made of finely spaced bands

of low birefringence that alternate between white and black colors under the cross-polarized light (Fig. 6G, H). All bands are parallel to each other and mimic the irregular shape of the vein margins, preserving the initial geometry of the fracture. The Raman spectra shows that serpentine polysomes filling these banded veins are diverse. Although recent studies have shown that the distinction between lizardite and polygonal serpentine is not obvious using Raman spectroscopy (Tarling *et al.,* 2018; Compagnoni *et al.,* 2021). Based on the Raman spectra, most of the banded veins exhibiting the typical OH stretching bands at 3685 cm^{-1} and 3707 cm^{-1} are filled by lizardite. Other spectra showing two peaks at 3692 cm^{-1} and 3700 cm^{-1} (Fig. 6) rather correspond to polygonal serpentine, whereas only rare occurrences of chrysotile were observed (main peaks at 3689 cm^{-1} and 3699 cm^{-1}).

Lamellar veins (S4): The fourth generation of serpentine (S4) is exclusively observed at Tasna and Upper Platta (proximal domains). Only one has been observed in a sample from Lower Platta (distal domain) and none from Totalp (proximal domain). It consists of disoriented serpentine lamellae with a first order grey to pale yellow birefringence under the cross-polarized light. It occurs mostly as veins crosscutting the pseudomorphic mesh and bastite and serpentine veins, which are highlighted by magnetite grains at the serpentine vein rims (Fig. 7). Lamellar veins are typically between 50- and 150-μm-thick, but they can also form large patches interconnected by veins of the same textures (Fig. 7). Lamellar veins appear to spread within the mesh textures, resulting in blurred rims (Fig. 7D). The Raman spectral signature indicates that these lamellar veins are made of a mixture of antigorite and chrysotile, with peaks at 3670 cm^{-1}, 3690 cm^{-1} and 3700 cm^{-1} (Fig. 7). Occasionally, some of these veins and patches display an additional peak at 3685 cm^{-1}, which likely indicates the local presence of small lizardite grains. Some carbonates, identified as calcite, are occasionally observed inside some of these lamellar veins (Fig. 7C).

Fibrous veins (S5): The last generation of serpentine (S5) is systematically observed in samples from Lower Platta and regularly observed in the other units. It forms crack-seal structures characterized by lens-shape extending along several mm-long and tens of μm width (Fig. 7 D). This serpentine polysome displays a typical fibrous aspect. The fibers are preferentially oriented perpendicular to the vein edge and are characterized by a high birefringence under cross-polarized light. The characteristic shoulder at 3690 cm^{-1} preceding a peak at 3701 cm^{-1} matches the Raman spectral signature of chrysotile in high wavelength domain (Fig. 7D).

To sum up, the different serpentine textures and polysomes described in this section are presented as an evolutionary sequence, comprised of five stages of serpentinization (Fig. 8).

Bulk-rock geochemistry

Most samples show typical concentrations of SiO$_2$ and MgO for serpentinites (41.33 wt % and 38.96 wt % in average, respectively; Fig. 9). They cover a wide range of concentrations in CaO (0.04–4.1 wt %) and Al$_2$O$_3$ (0.21–7.73 wt %). The presence of clinopyroxene and/or plagioclase in the samples can explain the high CaO measured in bulk, while higher Al$_2$O$_3$ content attests of the presence of spinel or plagioclase. Fig. 10 presents the MgO/SiO$_2$ and Al$_2$O$_3$/SiO$_2$ ratios of serpentinites from Totalp, Tasna, Upper and Lower Platta (Jagoutz *et al.,* 1979; Hart & Zindler, 1986). The serpentinized peridotites plot along the terrestrial mantle array. Most samples display fertile compositions (Al$_2$O$_3$/SiO$_2$ > 0.05) while only few samples derive from a refractory protolith. Mg# is around 0.94 for most serpentinites (Fig. 10), close to the Mg#
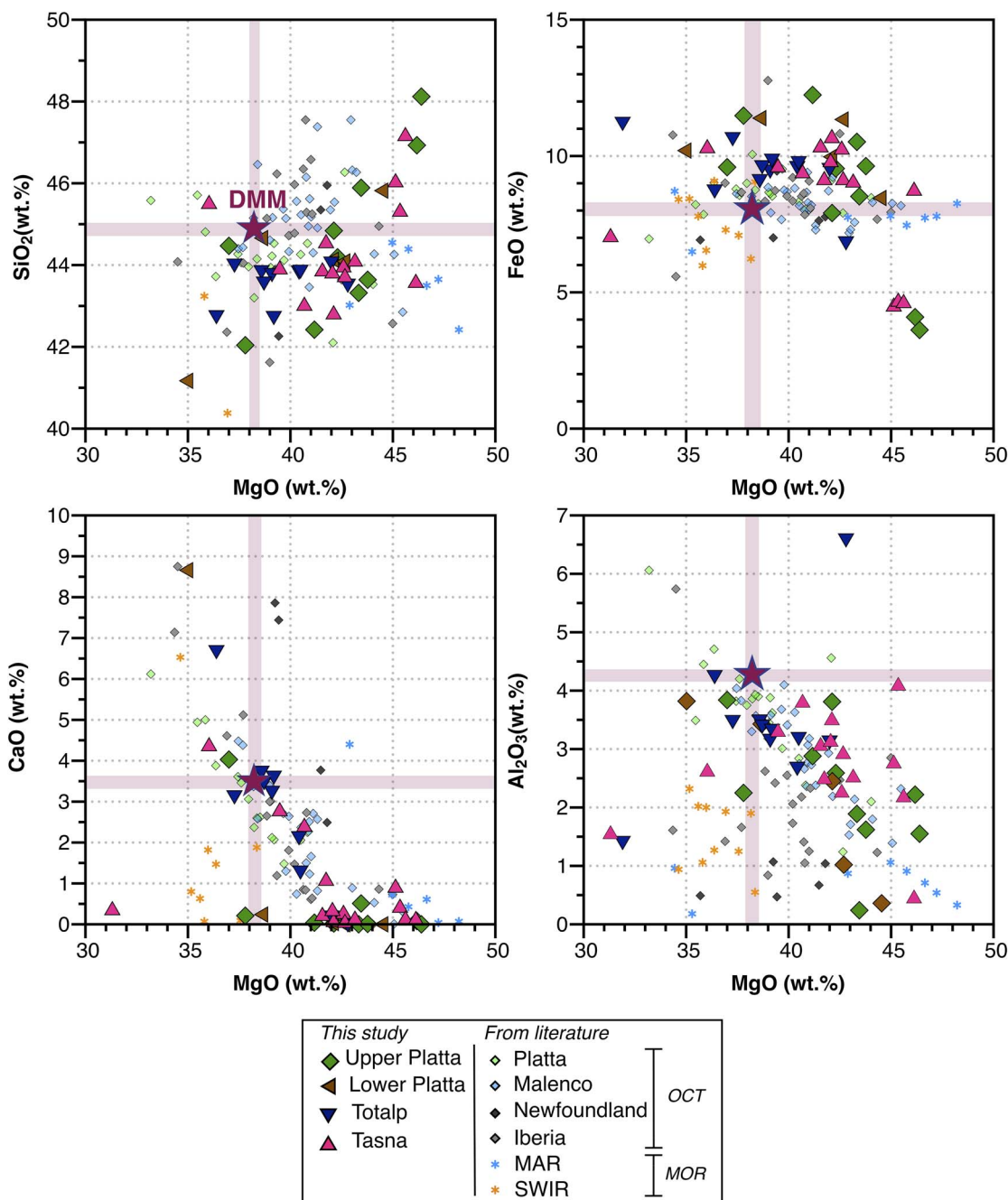
Fig. 9. Binary diagrams of bulk-rock compositions of serpentinites (recalculated in anhydrous basis) from Upper and Lower Platta, Tasna and Totalp showing MgO versus (A) SiO_2, (B) Fe_2O_3, (C) CaO and (D) Al_2O_3. Our data are compared to serpentinized peridotites from Platta and Malenco (Müntener *et al., 2010*), the Iberia Margin (Kodolányi *et al., 2012*; Albers *et al., 2021*), Newfoundland, Mid Atlantic Ridge (MAR) and Hess Deep (Kodolányi *et al., 2012*). South West Indian Ridge (SWIR; Rouméjon *et al., 2015*). DMM: Depleted MORB Mantle Salters & Stracke (2004).

values of initial peridotites (Müntener *et al., 2010*). Ni and Cr concentrations are mainly in the range 1500 to 2500 μg/g and 2000 to 3500 μg/g, respectively (Fig. 11). Interestingly, samples with abundant veining are characterized by high Mg# (up to 0.96, corresponding to samples with low FeO_{tot}, <5 wt %; Figs. 8 and 10) and very low Cr and Ni concentrations (<500 μg/g Table 2; Fig. 11).

Bulk-rock serpentinites normalized to Chondrite-C1 display homogeneous patterns, characterized by flat Heavy to Middle rare earth elements (REE) with relatively fertile compositions with $HREE_N$ > 2 and depletion in Light (L)REE (($La/Sm)_N$ = 0.80, in average n = 40; Fig. 12). Some samples from Tasna and Platta differ

from the overall trends by highly depleted HREE concentrations ($HREE_N$ ~ 0.1–1 C1-Chondrite; Fig. 12) and positive Eu anomalies (Eu/Eu^* = 1.41 in average, n = 40). Spider diagrams show enrichment in fluid mobile elements (FME), as highlighted by positive anomalies in Cs, B and Li. Locally, a slight enrichment in U is observed (up to 10 times PM in Tasna serpentinites), Pb and Sr (0.1–1 time PM in Upper and Lower Platta and Tasna serpentinites).

Serpentine geochemistry
Major elements

In average, serpentine mesh contains 40.91 wt% SiO_2 (Si = 1.91 apfu), 1.40 wt% Al_2O_3 (Al = 0.08 apfu), 38.87 wt% MgO (Mg = 2.74

Table 2: Bulk-rock major and trace element concentrations of the 40 serpentinized peridotites collected in the different units.

Unit	Upper Platta										Lower Platta				
Sample	Fal 18-02a	Fal 18-02b	Fal 18-03	Fal 18-04	Fal 18-05	Fal 18-06	Fal 18-07	Fal 18-08	Fal 18-09	Fal 18-10	Fal 18-11	Fal 18-12	Fal 18-13	Fal 18-14	Mar 18-01
SiO_2	40.18	36.13	38.52	41.13	38.82	39.71	39.85	38.15	39.21	38.09	39.91	35.50	39.06	38.84	38.20
TiO_2	0.098	0.096	0.133	0.025	0.077	0.008	0.254	0.040	0.066	0.038	0.022	0.174	0.059	0.066	0.018
Al_2O_3	1.903	2.453	2.261	1.328	2.079	0.209	3.439	1.662	3.332	1.411	0.317	3.289	3.003	2.160	0.884
Fe_2O_3	3.498	10.421	8.316	3.092	10.602	7.372	8.594	9.262	6.916	8.407	7.372	8.793	9.964	8.777	9.824
MnO	0.065	0.123	0.173	0.079	0.176	0.121	0.115	0.102	0.121	0.126	0.100	0.126	0.170	0.120	0.154
MgO	39.53	35.06	36.86	39.65	34.89	37.60	33.15	38.17	36.83	38.20	38.80	30.19	33.82	37.08	36.99
CaO	0.065	0.031	0.106	0.004	0.197	0.439	3.615	0.004	0.021	0.012	0.004	7.464	0.210	0.030	0.000
K_2O	b.d.l	b.d.l	b.d.l	b.d.l	b.d.l	b.d.l	0.006	b.d.l	b.d.l	b.d.l	b.d.l	b.d.l	b.d.l	b.d.l	b.d.l
Na_2O	0.242	0.084	0.108	0.116	0.078	0.489	0.000	0.056	0.205	0.170	0.163	0.041	0.455	0.241	0.033
Cr_2O_3	0.013	0.482	0.421	0.018	0.488	0.327	0.364	0.379	0.454	0.521	0.426	0.408	0.437	0.419	0.291
NiO	0.021	0.285	0.259	0.035	0.270	0.262	0.221	0.255	0.294	0.303	0.000	0.222	0.275	0.272	0.247
LOI	14.74	13.34	13.75	15.02	13.20	13.80	10.51	12.84	13.06	13.58	12.74	13.84	13.20	12.84	13.84
Total	100.4	98.5	100.9	100.5	100.9	100.3	100.1	100.9	100.5	100.9	99.9	100.0	100.7	100.8	100.5
Mg#	0.953	0.857	0.888	0.958	0.854	0.901	0.873	0.880	0.905	0.890	0.904	0.860	0.858	0.883	0.870
Trace (ppm)															
Li	8.200	11.90	21.80	5.700	3.000	7.200	10.40	4.600	7.300	2.400	15.40	10.40	10.60	11.30	2.800
B	15.11	40.42	98.49	26.74	25.98	82.74	113.8	56.45	66.79	73.04	54.42	42.42	152.4	50.76	46.75
V*	9.177	48.73	45.59	7.881	61.11	0.997	75.22	23.27	99.26	21.42	1.087	73.41	105.5	52.86	6.68
Cr	33.40	3170	2480	566.0	364.0	2440	2170	2440	2750	3020	3070	2270	2760	2320	1840
Mn	b.d.l	b.d.l	b.d.l	b.d.l	b.d.l	b.d.l	b.d.l	b.d.l	b.d.l	b.d.l	b.d.l	b.d.l	b.d.l	b.d.l	b.d.l
Co	47.40	116.0	99.10	29.00	33.20	95.10	82.10	94.80	117.0	98.40	105.0	163.0	104.0	101.0	91.90
Ni	147.0	2050	1810	316.0	347.0	1850	1370	1650	1940	1840	2030	1540	1910	1780	1780
Ni*	166.5	2242	2036	272.7	2192	2062	1736	2004	2307	2379	2362	1742	2164	2141	1940
Cu	0.860	9.920	13.60	5.880	1.160	5.360	16.50	10.80	16.80	12.70	8.890	7.830	14.30	18.80	13.30
Zn	11.30	43.50	39.20	26.50	23.40	27.40	38.80	46.50	38.10	52.10	50.10	40.40	59.90	51.70	104.0
As	b.d.l	b.d.l	8.000	b.d.l	b.d.l	2.100	b.d.l	b.d.l	17.000	b.d.l	b.d.l	38.000	b.d.l	10.00	2.000
Rb	0.090	0.170	0.390	0.175	0.090	0.450	0.960	0.120	0.550	0.070	0.120	0.580	1.240	0.440	0.590
Sr	0.700	2.400	6.100	0.900	0.500	4.100	13.400	1.600	3.500	1.400	1.500	13.500	5.000	2.000	4.400
Y	0.350	1.190	1.690	0.330	1.360	0.251	3.060	0.627	1.250	0.487	0.293	2.300	1.350	1.370	0.336
Zr	1.710	2.910	3.000	6.270	2.280	0.730	5.970	1.130	0.760	0.840	0.610	2.860	0.800	0.510	0.370
Nb	1.200	0.855	0.519	0.096	0.372	0.269	0.304	0.156	0.145	0.085	0.130	0.132	0.033	0.026	0.109
Mo	0.260	0.320	0.240	0.020	0.140	0.240	0.160	0.180	0.070	0.160	0.130	b.d.l	b.d.l	b.d.l	b.d.l
Cd	b.d.l	0.013	0.032	0.009	0.081	0.007	0.054	0.007	0.072	0.020	0.080	0.015	0.018	0.020	0.010
Sn	0.160	0.140	0.130	0.050	0.140	0.180	0.230	0.060	0.100	0.050	0.013	0.110	0.110	0.030	0.420
Sb	0.100	0.150	0.120	0.037	0.060	0.080	b.d.l	b.d.l	0.220	0.080	0.100	0.100	0.070	0.070	0.100
Cs	0.150	0.410	0.960	0.268	0.020	1.250	1.740	0.080	0.640	0.030	0.110	0.100	2.970	0.580	0.520
Ba	0.734	2.500	2.840	1.580	1.160	1.320	3.260	1.160	2.210	0.821	0.250	1.050	1.920	0.839	1.610
La	0.037	0.078	0.070	0.050	0.041	0.070	0.179	0.056	0.009	0.036	0.458	1.600	0.009	b.d.l	0.228
Ce	0.080	0.239	0.258	0.110	0.126	0.198	0.661	0.122	0.037	0.071	0.167	0.581	0.013	0.011	0.409
Pr	0.018	0.045	0.052	0.015	0.026	0.032	0.125	0.015	0.007	0.012	0.024	0.086	b.d.l	b.d.l	0.044
Nd	0.065	0.253	0.328	0.077	0.164	0.166	0.793	0.071	0.064	0.041	0.124	0.486	0.042	0.055	0.178
Sm	0.032	0.104	0.142	0.025	0.084	0.045	0.313	0.029	0.051	0.020	0.040	0.198	0.051	0.059	0.036
Eu	0.020	0.050	0.110	0.016	0.030	0.070	0.140	0.058	0.030	0.020	0.030	0.090	0.060	0.040	0.100
Gd	0.044	0.166	0.220	0.037	0.162	0.044	0.478	0.013	0.120	0.042	0.060	0.312	0.126	0.136	0.043
Tb	0.014	0.031	0.043	0.008	0.033	0.007	0.084	0.013	0.027	0.014	0.011	0.059	0.029	0.030	0.008
Dy	0.060	0.223	0.313	0.053	0.250	0.041	0.608	0.113	0.220	0.078	0.058	0.431	0.238	0.244	0.051
Ho	0.019	0.054	0.069	0.013	0.059	0.006	0.131	0.026	0.051	0.023	0.011	0.096	0.057	0.054	0.009
Er	0.048	0.165	0.209	0.041	0.180	0.017	0.388	0.091	0.166	0.071	0.030	0.287	0.181	0.174	0.030
Tm	0.012	0.026	0.032	0.006	0.027	b.d.l	0.057	0.014	0.026	0.014	b.d.l	0.043	0.029	0.026	b.d.l
Yb	0.053	0.180	0.224	0.044	0.178	0.021	0.389	0.112	0.194	0.093	0.031	0.302	0.212	0.191	0.047
Lu	0.013	0.030	0.035	0.008	0.026	b.d.l	0.057	0.017	0.031	0.017	b.d.l	0.048	0.031	0.029	0.007
Hf	0.173	0.210	0.181	2.320	0.143	0.049	0.273	0.058	0.063	0.175	0.132	0.202	0.116	0.085	0.053
Ta	0.041	0.039	0.029	0.038	0.025	0.023	0.024	0.020	0.021	0.035	0.029	0.024	0.022	0.018	0.019
Pb	0.081	0.176	0.260	0.835	2.460	0.290	0.299	0.065	1.020	0.987	0.169	0.483	0.177	0.168	0.424
Th	0.550	0.250	0.150	0.200	0.110	0.080	0.090	0.060	0.050	0.400	0.120	0.090	0.050	0.040	0.030
U	b.d.l	b.d.l	b.d.l	0.032	b.d.l	b.d.l	b.d.l	b.d.l	b.d.l	b.d.l	b.d.l	0.505	b.d.l	b.d.l	b.d.l

Table 2: Continued

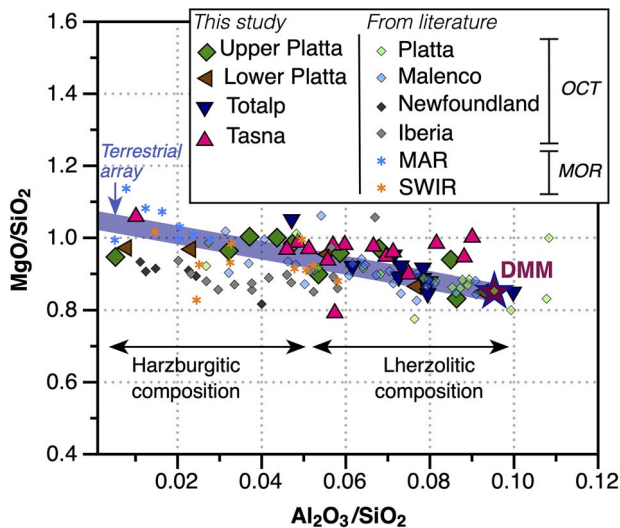| Unit	Totalp										Tasna															
Sample	Tot 19-01	Tot 19-02	Tot 19-03a	Tot 19-03b	Tot 19-04	Tot 19-05	Tot 19-07	Tot 19-09	Tot 19-10a	Tot 19-10b	Tas 19-01	Tas 19-02	Tas 19-03	Tas 19-04	Tas 19-05	Tas 19-06a	Tas 19-06b	Tas 19-07	Tas 19-08	Tas 19-09	Tas 19-10	Tas 19-11	Tas 19-12	Tas 19-13	Tas 19-14	Tas 19-15
SiO_2	38.66	38.20	38.41	38.00	38.65	38.13	38.90	38.36	37.20	38.52	n.d	37.50	38.73	37.03	38.52	40.22	38.44	39.57	38.61	40.70	38.71	38.27	38.54	38.79	39.98	37.81
TiO_2	0.153	0.190	0.087	0.007	0.171	0.186	0.203	0.176	0.164	0.164	n.d	0.092	0.128	0.122	0.125	0.016	0.073	0.011	0.085	0.031	0.082	0.127	0.120	0.065	0.118	0.020
Al_2O_3	3.090	3.810	2.366	5.771	2.803	2.988	3.093	2.805	2.919	2.755	n.d	3.306	2.906	3.018	2.679	2.402	1.870	3.566	1.975	1.875	2.155	2.549	2.744	2.207	2.292	0.381
Fe_2O_3	8.069	7.834	8.440	6.003	8.385	8.460	9.455	8.580	8.619	8.361	n.d	8.162	8.456	9.218	9.063	3.911	8.502	4.064	8.991	3.971	7.920	7.978	8.600	7.938	9.031	7.571
MnO	0.127	0.123	0.130	0.075	0.122	0.120	0.132	0.111	0.137	0.122	n.d	0.126	0.132	0.111	0.117	0.068	0.128	0.066	0.134	0.097	0.125	0.126	0.120	0.084	0.117	0.082
MgO	34.00	32.49	35.38	37.35	34.50	33.85	32.92	35.38	34.09	36.69	n.d	35.48	34.84	36.44	36.52	39.45	37.94	39.62	37.43	39.36	36.29	37.36	37.01	37.97	31.66	40.03
CaO	3.317	5.993	1.895	0.024	2.885	3.067	2.788	1.154	3.169	0.190	n.d	2.079	2.433	0.045	0.180	0.779	0.411	0.350	0.222	0.096	0.918	0.024	0.281	0.099	3.825	0.090
K_2O	b.d.l	b.d.l	b.d.l	b.d.l	b.d.l	b.d.l	b.d.l	b.d.l	b.d.l	0.000	n.d	b.d.l	b.d.l	b.d.l	b.d.l	b.d.l	b.d.l	b.d.l	b.d.l	b.d.l	b.d.l	b.d.l	b.d.l	b.d.l	b.d.l	b.d.l
Na_2O	0.029	0.000	0.149	0.000	0.072	0.083	0.141	0.102	0.028	0.000	n.d	0.054	0.178	0.095	0.225	0.522	0.128	0.076	0.000	0.136	0.155	0.503	0.000	0.187	0.066	0.198
Cr_2O_3	0.441	0.468	0.429	0.013	0.398	0.354	0.452	0.375	0.413	0.341	n.d	0.410	0.443	0.453	0.446	0.038	0.296	0.031	0.439	0.045	0.327	0.493	0.357	0.409	0.466	0.353
NiO	0.219	0.173	0.256	0.019	0.240	0.219	0.243	0.222	0.213	0.215	n.d	0.000	0.000	0.000	0.000	0.000	33.383	0.000	0.000	0.000	0.254	0.141	0.239	0.248	0.321	0.267
LOI	12.04	10.87	12.17	13.24	11.92	12.66	11.82	12.74	13.08	13.52	n.d	12.72	11.67	14.07	12.74	13.05	12.73	13.07	12.81	14.07	13.19	13.22	12.91	12.89	12.30	13.30
Total	100.1	100.1	99.7	100.5	100.1	100.1	100.1	100.0	100.0	100.9	n.d	99.9	99.9	100.6	100.6	100.5	133.9	100.4	100.7	100.4	100.1	100.8	100.9	100.1	100.2	100.1
Mg#	0.882	0.881	0.882	0.917	0.880	0.877	0.861	0.880	0.876	0.887	n.d	0.886	0.880	0.876	0.878	0.947	0.888	0.946	0.881	0.946	0.891	0.893	0.885	0.895	0.862	0.904
Trace (ppm)																										
Li	4.500	3.800	2.800	2.400	0.900	5.100	10.80	10.40	24.70	24.60	14.30	10.70	1.300	7.400	8.500	5.900	3.600	1.200	2.000	b.d.l	3.900	4.900	38.00	7.000	11.80	1.300
B	6.510	5.950	n.d	n.d	n.d	13.31	106.73	68.55	48.40	42.99	52.93	39.55	37.12	43.14	31.29	4.250	20.69	4.810	15.81	9.030	12.28	38.98	92.90	90.87	115.6	100.8
V*	65.22	78.94	72.08	3.381	62.28	62.89	70.06	63.29	57.55	58.76	59.60	62.20	66.26	62.18	62.24	3.398	23.56	11.26	19.89	8.504	37.15	58.11	62.23	28.37	57.91	4.650
Cr	2630	2790	1290	29.00	2610	2300	2420	2230	2300	1950	2340	2420	2600	2420	2850	166.0	1780	124.0	2370	109.0	2010	2650	2840	2150	2070	2310
Mn	909.0	912.0	629.0	441.0	931.0	887.0	873.0	833.0	962.0	862.0	806.0	881.0	771.0	854.0	831.0	452.0	832.0	394.0	824.0	521.0	853.0	852.0	786.0	593.0	790.0	687.0
Co	96.70	88.60	56.30	14.20	105.00	98.50	94.90	106.0	93.00	94.90	101.0	86.50	112.0	89.70	104.0	8.04	100.0	6.030	94.40	11.90	83.80	66.80	105.0	92.20	88.60	106.0
Ni	1650	1470	942.0	120.0	1940	1700	1773	1742	1660	1720	1840	1610	2100	1660	1900	223.0	1968	110.0	1800	483.0	1770	1000	2140	1780	1660	2060
Ni*	1717	1358	1538	145.9	1887	1724	1912	1912	1675	1689	1905	1673	1839	2245	2030	236.6	2053	138.2	2166	602.1	1998	1108	1879	1948	2526	2100
Cu	36.10	25.90	16.90	10.50	30.80	27.30	25.80	25.70	15.80	25.10	13.10	2.900	26.60	21.80	23.30	2.700	8.500	0.900	7.580	8.350	10.80	11.70	28.90	10.80	20.70	2.280
Zn	59.20	51.00	28.50	28.50	54.60	47.90	51.20	50.50	51.50	40.00	47.10	41.90	48.10	40.70	55.50	39.00	38.40	25.90	55.60	25.60	40.90	61.40	41.60	37.40	37.50	48.90
As	b.d.l	0.021	0.012	0.040	0.049	0.188	0.750	0.557	0.104	0.153	0.578	b.d.l	0.167	b.d.l	0.305	0.080	b.d.l	0.040	0.015	0.079	0.028	0.031	0.358	0.039	b.d.l	b.d.l
Rb	0.131	0.130	0.140	0.050	0.320	0.130	0.130	0.160	0.150	0.130	0.034	0.056	0.036	0.039	0.057	0.020	0.051	0.008	0.015	0.012	0.017	0.035	0.047	0.026	0.042	0.150
Sr	8.940	5.470	1.050	0.360	9.610	12.400	13.900	4.710	3.560	1.950	18.80	28.40	1.620	2.820	5.050	0.500	1.600	0.400	0.800	0.540	1.330	1.590	17.000	3.740	3.680	1.020
Y	2.500	3.720	1.460	0.129	2.880	2.800	2.820	2.590	2.510	2.280	1.710	1.590	2.180	2.090	2.550	0.235	0.942	0.139	0.838	0.238	1.290	0.978	1.380	1.110	1.560	0.152
Zr	2.790	3.940	2.770	0.570	3.130	3.970	6.300	4.730	4.820	3.320	7.860	1.040	5.950	0.840	1.380	0.480	1.220	1.310	0.450	0.180	0.470	0.840	1.380	0.670	1.560	0.530
Nb	0.014	0.016	0.018	0.019	0.082	0.192	0.089	0.076	0.086	0.072	0.052	0.041	0.050	b.d.l	0.880	0.020	b.d.l	0.020	b.d.l	0.019	0.010	0.008	0.041	0.015	b.d.l	0.013
Mo	0.040	0.030	0.030	0.030	0.070	0.050	0.080	0.070	0.070	0.080	0.060	0.050	0.050	0.040	0.280	0.030	0.050	0.020	0.050	0.030	0.040	0.020	0.060	0.090	0.030	0.050
Cd	0.003	0.031	b.d.l	0.056	0.013	0.002	0.020	0.018	0.021	0.030	0.030	0.022	0.016	0.019	0.017	0.020	0.011	0.017	0.008	0.024	0.032	0.017	0.025	0.011	0.010	0.008
Sn	0.060	0.130	0.140	0.050	0.140	0.130	0.130	0.160	0.150	0.130	0.100	0.110	0.090	0.110	0.170	0.090	0.040	0.070	0.050	0.060	0.070	0.090	0.140	0.060	0.070	0.150
Sb	b.d.l	b.d.l	b.d.l	b.d.l	b.d.l	b.d.l	0.011	0.029	0.080	0.089	0.157	0.045	0.038	0.039	0.082	0.012	b.d.l	0.009	0.005	0.007	0.006	0.090	0.057	0.112	0.012	0.150
Cs	0.013	0.003	b.d.l	0.002	0.028	0.115	0.190	0.176	0.029	0.042	1.060	1.340	0.129	0.293	0.247	b.d.l	0.023	b.d.l	0.011	0.007	0.005	0.008	0.966	0.101	0.150	b.d.l
Ba	0.090	b.d.l	0.870	1.710	0.320	0.620	b.d.l	0.990	1.030	0.620	2.710	1.520	0.870	0.580	1.590	1.000	0.300	0.900	0.330	2.450	1.940	1.930	5.310	2.670	1.230	0.140
La	0.027	0.040	0.052	0.068	0.104	0.555	0.107	0.082	0.147	0.108	0.034	0.056	0.036	0.013	1.630	0.071	0.051	0.026	0.008	0.118	0.017	0.028	0.047	0.026	0.013	0.042
Ce	0.189	0.253	0.237	0.174	0.409	1.430	0.440	0.361	0.449	0.393	0.051	0.122	0.079	0.043	2.770	0.100	0.081	0.045	0.018	0.143	0.024	0.035	0.197	0.079	0.018	0.186
Pr	0.053	0.068	0.054	0.018	0.082	0.192	0.089	0.076	0.086	0.072	0.008	0.019	0.017	0.018	0.279	0.013	0.010	0.006	0.005	0.027	0.007	0.011	0.041	0.016	0.008	0.038
Nd	0.380	0.518	0.335	0.077	0.541	0.937	0.571	0.507	0.536	0.455	0.071	0.134	0.154	0.173	1.060	0.065	0.079	0.031	0.059	0.121	0.083	0.099	0.275	0.122	0.101	0.222
Sm	0.185	0.273	0.133	0.019	0.237	0.284	0.245	0.215	0.215	0.188	0.067	0.080	0.108	0.126	0.230	0.019	0.045	0.012	0.043	0.030	0.071	0.068	0.129	0.063	0.087	0.056
Eu	0.081	0.108	0.120	0.006	0.096	0.107	0.092	0.086	0.119	0.050	0.036	0.030	0.045	0.073	0.057	0.017	0.013	0.006	0.015	0.007	0.018	0.023	0.062	0.026	0.042	0.018
Gd	0.285	0.413	0.186	0.020	0.348	0.378	0.383	0.336	0.339	0.306	0.157	0.163	0.219	0.239	0.332	0.034	0.101	0.019	0.085	0.040	0.152	0.123	0.207	0.118	0.187	0.041
Tb	0.061	0.086	0.036	0.003	0.071	0.073	0.071	0.065	0.061	0.055	0.036	0.036	0.044	0.048	0.059	0.006	0.018	0.003	0.018	0.006	0.030	0.024	0.039	0.024	0.037	0.005
Dy	0.432	0.640	0.261	0.004	0.511	0.510	0.506	0.466	0.442	0.417	0.283	0.290	0.370	0.371	0.434	0.037	0.156	0.023	0.147	0.043	0.228	0.181	0.289	0.197	0.303	0.032
Ho	0.096	0.143	0.056	0.004	0.111	0.109	0.108	0.101	0.094	0.091	0.068	0.065	0.083	0.083	0.096	0.007	0.033	0.004	0.033	0.008	0.051	0.040	0.062	0.044	0.068	0.006
Er	0.299	0.451	0.171	0.010	0.350	0.343	0.350	0.314	0.302	0.285	0.216	0.214	0.274	0.265	0.307	0.022	0.116	0.015	0.110	0.024	0.163	0.124	0.201	0.141	0.217	0.020
Tm	0.043	0.066	0.024	0.001	0.049	0.048	0.050	0.047	0.042	0.041	0.033	0.032	0.039	0.039	0.046	0.003	0.017	0.002	0.016	0.003	0.023	0.018	0.027	0.022	0.033	0.003
Yb	0.305	0.450	0.171	0.012	0.344	0.333	0.350	0.311	0.303	0.293	0.245	0.234	0.291	0.273	0.341	0.026	0.133	0.018	0.121	0.025	0.168	0.130	0.208	0.158	0.246	0.029
Lu	0.046	0.067	0.025	0.004	0.049	0.050	0.052	0.048	0.046	0.044	0.037	0.035	0.041	0.041	0.052	0.004	0.020	0.003	0.018	0.004	0.028	0.020	0.030	0.024	0.040	0.005
Hf	0.274	0.348	0.169	0.036	0.180	0.211	0.890	0.409	0.350	0.142	0.340	0.132	0.893	0.073	0.074	0.090	0.680	0.400	0.032	0.013	0.042	0.124	0.067	0.029	0.301	0.020
Ta	0.006	0.005	0.004	b.d.l	0.049	0.029	0.014	0.003	0.004	0.004	0.028	0.003	0.022	0.039	0.038	b.d.l	b.d.l	0.005	b.d.l	b.d.l	b.d.l	b.d.l	b.d.l	b.d.l	b.d.l	b.d.l
Pb	0.005	0.077	0.048	6.010	0.096	0.072	b.d.l	0.122	0.296	0.118	0.207	0.166	0.215	0.237	0.162	0.580	b.d.l	0.530	0.056	0.306	0.041	0.274	0.515	0.413	b.d.l	0.132
Th	0.057	0.048	0.040	0.036	0.036	0.072	0.020	0.052	0.034	0.018	0.101	0.025	0.078	0.014	0.104	0.030	0.010	0.010	0.009	0.013	0.009	0.009	0.005	0.010	0.012	0.132
U	0.003	0.001	b.d.l	0.007	b.d.l	0.019	0.001	0.002	0.005	0.002	0.004	0.008	b.d.l	0.003	0.049	0.053	b.d.l	0.013	0.001	0.032	0.111	0.003	-b.d.l	0.006	0.001	0.028

Fig. 10. Bulk rock major element ratios of Al_2O_3/SiO_2 (anhydrous) versus MgO/SiO_2 (anhydrous) of serpentinites. The blue line corresponds to the Terrestrial array (Jagoutz *et al.*, 1979; Hart & Zindler, 1986). References are the same as in Fig. 9.
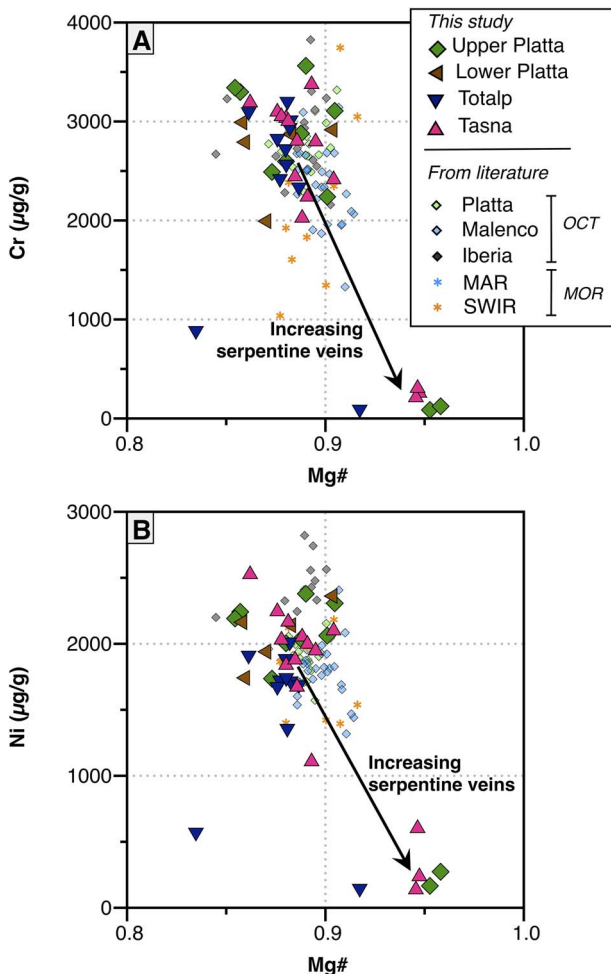

Fig. 11. Mg# versus bulk-rock Ni (A) and Cr (B) concentrations (in μg/g) of serpentinites from Upper and Lower Platta, Tasna and Totalp. References are the same as in Fig. 9.

apfu) and 5.30 wt% FeO_{tot} ($Fe_{tot} = 0.21$ apfu), giving a Mg# of ∼0.93. Bastite texture slightly differs in composition relative to mesh texture, with less SiO_2 (39.81 wt%; Si = 1.9 apfu), MgO (37.49 wt%;

Mg = 2.6 apfu) and FeO_{tot} (4.74 wt%; $Fe_{tot} = 0.18$ apfu) and more Al_2O_3 (4.12 wt%; Al = 0.23 apfu), because they retain part of Al from primary pyroxene (Table 3). Consequently, serpentine mesh plots close to the Mg-pure lizardite or chrysotile end-members in the Si versus Mg + Fe diagram (Fig. 13A), whereas bastite composition extends along the Tschermak trend (Al replacing an octahedral and tetrahedral cation; Fig. 13A, B). Bastite has Mg# near identical to mesh textures (0.94 in average, Table 3; Fig. 14).

The polyhedral serpentine (S2) is generally characterized by lower FeO_{tot} content (4.19 wt%, Fe_{tot} ∼0.16 apfu) at given SiO_2 and MgO concentrations relative to serpentine mesh (S1; 3A). As a consequence, this second generation of serpentine has higher Mg# values (>0.94 in average; Fig. 14). It is also characterized by relatively high Al_2O_3 concentrations (2.84 wt%, Al = 0.16 apfu) and thus plots between mesh and bastite serpentines along the Tschermak trend (Fig. 13A, B).

The banded serpentine veins (S3) mainly plot within the field defined by serpentine mesh (S1) in the Si versus Mg + Fe diagram (Fig. 13C, Table 3). However, these banded veins can be distinguished by higher Mg# values (>0.95 Table 3, Fig. 14) due to lower Fe_{tot} content relative to the two previous generations. More specifically, the banded veins can be subdivided into two groups based on their Mg# and Raman signature (Figs. 14 and 15): the first group made of polygonal serpentine is characterized by Mg# of ∼0.95 ($Fe_{tot} = 0.07$–0.28 apfu, Mg = 2.6–2.8 apfu), whereas the second group made of lizardite has Mg# >0.97 ($Fe_{tot} < 0.10$ apfu, Mg = 2.7–2.9 apfu). The banded veins also contain Al apfu higher than the serpentine mesh S1 at a given Si apfu (Al ∼0.1 versus ∼0.05, respectively at Si ∼1.95 apfu). Some veins even extend along the Tschermak trend towards the bastite field (Fig. 13C, D).

The lamellar antigorite veins and patches (S4) display the highest SiO_2 concentrations of all serpentine generations (42.48 ± 1.08 wt%, Si = 1.99 apfu), and Mg + Fe in the range of 9.79–2.93, close to the pure antigorite end-member (Fig. 13C). Interestingly, unlike the gradual increase in Mg# described in previous generations of serpentine from the initial mesh, antigorite veins have lower Mg# (<0.95 in average) due to higher Fe concentrations ($FeO_{tot} = 4.15$ wt% in average, $Fe_{tot} = 0.16$ apfu, Fig. 14). Al_2O_3 concentrations are low (1.15 ± 1.07 wt %, Al = 0.06 apfu).

The last generation of serpentine veins (crack-seal filled by chrysotile; S5) have Mg + Fe content within the range of previous generations of serpentine veins, with nevertheless slightly higher MgO = 39.76 ± 0.97 wt % and lower $FeO_{tot} = 3.99 ± 1.18$ wt % concentrations (Mg = 2.79 apfu, $Fe_{tot} = 0.16$ apfu, Mg# = 0.95; Figs. 13C and 14). They also show very similar SiO_2 and Al_2O_3 concentrations to those of the antigorite ($SiO_2 = 42.17 ± 0.94$ wt %, Si = 1.98 apfu; $Al_2O_3 = 0.76 ± 0.62$ wt %, Al = 0.04 apfu; Fig. 13D).

Interestingly, none of the serpentine composition plots along the brucite trend (Fig. 13). This is consistent with the fact that brucite was never observed in our samples, neither on microscopic observations nor through the different techniques used (i.e. XRD and Raman spectroscopy).

Trace elements

The representative trace element concentrations of each serpentine generation are given in Table 4, Figs. 16 and 17. REE and spider diagrams of all samples analyzed in this study are given in supplementary materials. The REE concentrations of serpentine polysomes (Figs. 16 and 17) vary between 0.001 and < 10 times the chondrite C1 and mimic the REE pattern of their respective bulk-rocks. They are similar in shape and concentration to exhumed
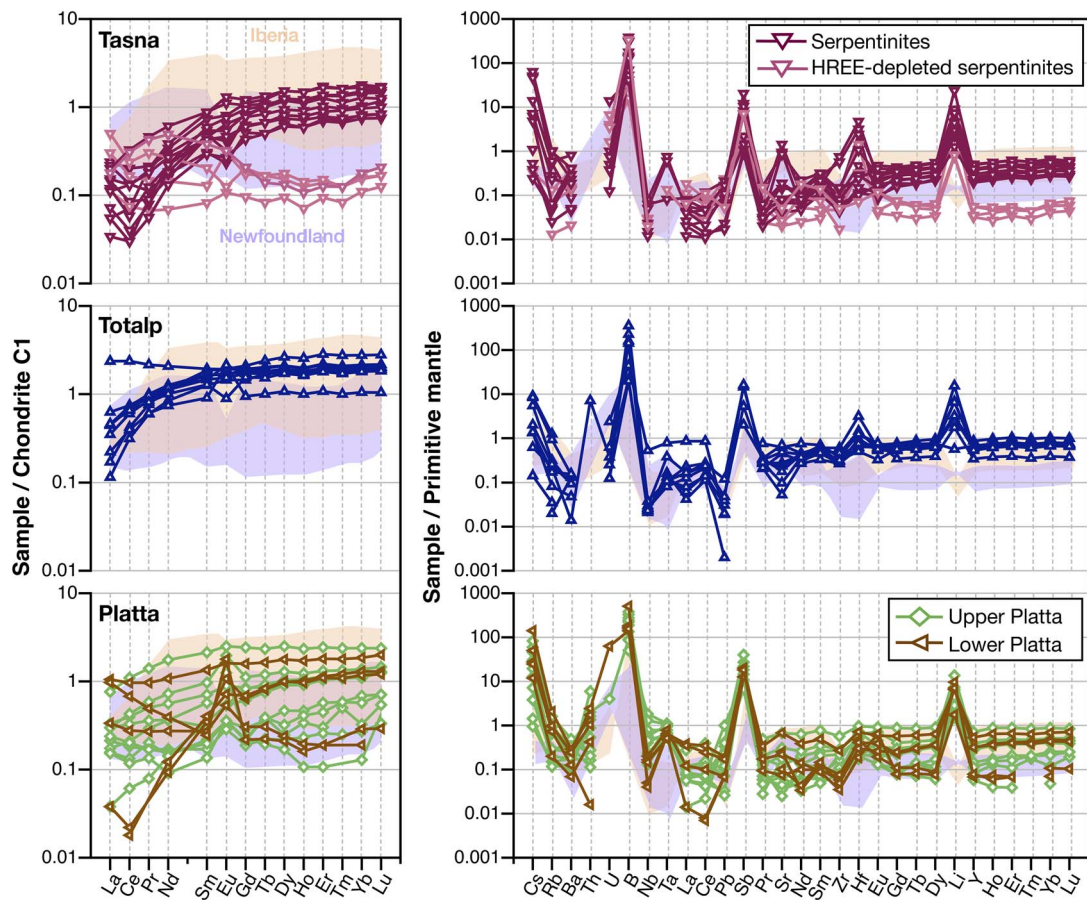
Table 3: Representative major element concentrations (in wt %) of serpentine minerals and veins measured by μXRF

Unit	Upper Platta					Lower Platta					Totalp				Tasna			
Sample / Texture	Fal 18-06 mesh (S1)	Fal 18-02 bastite (S1)	Fal 18-03 banded vein (S3)	Fal 18-06 lamellar vein (S4)	Fal 18-06 fibrous vein (S5)	Mar 18-01 mesh (S1)	Mar 18-01 bastite (S1)	Mar 18-01 banded vein (S3)	Mar 18-01 lamellar vein (S4)	Mar 18-01 fibrous vein (S5)	Tot 19-02 mesh (S1)	Tot 19-02 bastite (S1)	Tot 19-02 spherical vein (S2)	Tot 19-07 banded vein (S3)	Tas 19-02 mesh (S1)	Tas 19-03 bastite (S1)	Tas 19-08 banded vein (S3)	Tas 19-02 lamellar vein (S4)
Type	lizardite	lizardite	polygonal	antigorite	chrysotile	lizardite	lizardite	lizardite	antigorite	chrysotile	lizardite	lizardite	polyhedral	polygonal	lizardite	lizardite	lizardite	antigorite
Primary minerals	ol	opx	-	-	-	ol	opx	-	-	-	ol	cpx	-	-	ol	cpx	-	-
SiO_2	41.54	39.40	41.24	42.87	41.41	40.52	40.14	42.10	42.26	42.28	40.57	38.67	40.70	42.51	42.05	40.68	42.50	43.29
TiO_2	0.028	0.088	0.660	0.026	0.020	0.035	0.035	0.035	0.028	0.030	0.027	0.090	0.030	0.040	0.245	0.100	0.040	0.054
Al_2O_3	0.265	4.704	2.123	0.233	0.290	1.335	1.180	0.665	0.965	0.880	1.977	5.515	3.530	0.890	0.640	2.790	1.500	0.974
Fe_2O_3	5.135	3.907	4.010	4.574	4.600	5.023	4.995	3.055	4.258	3.820	4.900	4.635	2.787	2.530	4.020	4.135	1.570	3.465
MnO	0.125	0.090	0.200	0.206	0.160	0.155	0.135	0.120	0.272	0.180	0.117	0.110	0.093	0.110	0.155	0.105	0.070	0.133
MgO	39.80	38.12	38.39	38.94	41.09	39.59	39.90	41.07	38.93	39.84	39.17	37.52	39.59	40.83	39.42	38.22	40.75	38.38
CaO	0.088	0.175	0.607	0.063	0.180	0.063	0.055	0.065	0.064	0.080	0.147	0.535	0.443	0.210	0.565	0.845	1.190	0.431
K_2O	b.d.l	b.d.l	b.d.l	b.d.l	b.d.l	b.d.l	b.d.l	b.d.l	b.d.l	b.d.l	b.d.l	b.d.l	b.d.l	b.d.l	b.d.l	b.d.l	b.d.l	b.d.l
Na_2O	b.d.l	b.d.l	b.d.l	b.d.l	b.d.l	b.d.l	b.d.l	b.d.l	b.d.l	b.d.l	b.d.l	b.d.l	b.d.l	b.d.l	b.d.l	b.d.l	b.d.l	b.d.l
Cr_2O_3	0.090	0.786	0.143	0.031	0.060	0.483	0.905	0.073	0.049	0.070	0.027	0.210	0.017	0.030	0.070	0.355	0.010	0.051
NiO	0.323	0.058	0.020	0.083	0.050	0.195	0.135	0.025	0.079	0.050	0.427	0.090	b.d.l	b.d.l	0.150	0.060	0.020	0.097
Total	87.39	87.29	87.39	87.02	87.32	87.38	87.47	87.21	86.91	87.22	87.36	87.32	87.19	87.16	87.32	87.27	87.20	86.88
p.f.u																		
Si	1.968	1.855	1.941	1.978	1.953	1.922	1.907	1.971	1.947	1.985	1.922	1.829	1.904	1.984	1.981	1.920	1.980	1.980
Ti	0.001	0.003	0.024	0.001	0.001	0.001	0.001	0.001	0.001	0.001	0.001	0.003	0.001	0.001	0.009	0.004	0.001	0.002
Al	0.015	0.261	0.118	0.013	0.016	0.075	0.066	0.037	0.051	0.049	0.110	0.308	0.195	0.049	0.036	0.155	0.058	0.053
Fe^{2+}	0.180	0.154	0.105	0.164	0.144	0.189	0.162	0.120	0.174	0.150	0.194	0.184	0.109	0.099	0.110	0.162	0.020	0.116
Fe^{3+}	0.022	0.000	0.048	0.011	0.014	0.009	0.034	0.000	0.000	0.000	0.000	0.000	0.000	0.000	0.044	0.001	0.038	0.015
Mn	0.005	0.004	0.008	0.008	0.007	0.006	0.006	0.005	0.012	0.007	0.005	0.005	0.003	0.005	0.006	0.004	0.003	0.005
Mg	2.811	2.678	2.694	2.679	2.889	2.799	2.826	2.867	2.663	2.789	2.766	2.646	2.762	2.841	2.768	2.689	2.830	2.617
Ca	0.004	0.009	0.031	0.003	0.009	0.003	0.003	0.003	0.002	0.004	0.007	0.027	0.022	0.011	0.029	0.043	0.059	0.021
K	.	.	.	.	.	.	.	.	.	.	.	.	.	.	.	.	.	.
Na	.	.	.	.	.	.	.	.	.	.	0.001	0.001	0.001	0.001	0.003	0.014	0.000	0.002
Cr	0.003	0.029	0.005	0.001	0.002	0.019	0.034	0.003	0.000	0.003	0.016	0.008	0.000	0.000	0.006	0.002	0.001	0.004
Ni	0.012	0.002	0.001	0.003	0.002	0.008	0.006	0.001	0.001	0.002		0.001						
Mg#	0.940	0.946	0.963	0.942	0.953	0.937	0.946	0.960	0.939	0.949	0.934	0.935	0.962	0.966	0.962	0.943	0.993	0.958
Fe^{3+}/Fe_T	0.107	0.000	0.314	0.053	0.053	0.045	0.174	0.000	0.000	0.000	0.000	0.000	0.000	0.000	0.286	0.006	0.655	0.117

The structural formula for all serpentine minerals and veins have been calculated on the basis of 7 oxygens, except for antigorite for which calculations have been done on the basis of 6.823 oxygen, corresponding to m = 17 in the antigorite general formulae $Mg_{3m-3}Si_{2m}O_{5m}(OH)_{4m-6}$.

Fig. 12. Representative rare earth element (REE) patterns normalized the Chondrite C1 (left) and Primitive Mantle (PM)-normalized extended trace element patterns (right) of bulk-rock serpentinites from Tasna, Totalp and Platta (green: Upper Platta, brown: Lower Platta), in comparison with bulk-rock serpentinites from Iberia (orange field) and Newfoundland (purple field), data from Kodolányi et al., (2012).

mantle peridotites from other places in the Alps (e.g. the Chenaillet unit, Lafay et al., 2017). At sample scale, the REE patterns of the diverse serpentine polysomes are similar in shape: LREE-depleted ($(La/Sm)_N \sim 0.35$), with relatively flat middle (MREE) to HREE patterns. Noteworthy a progressive depletion from the first to the last serpentine generation is documented. Two samples from the Lower and Upper Platta units exhibit very different REE concentrations, both forming a U-shaped pattern characterized by enrichment of LREE and HREE over MREE and strong positive Eu anomalies (Eu/Eu* > 2; Figs. 16 and 17).

At sample scale, the primitive mantle-normalized patterns of serpentine minerals and veins exhibit similar shapes, with a global depletion relative to the PM. As for concentrations in bulk-rock, all serpentines are enriched in FME with positive anomalies in Cs, B, As, Sr and Li (concentrations between 0.1 and > 100 times the PM; Figs. 16 and 17). Additionally, a significant enrichment in U relative to Th is observed (U/Th = 14.84 in average; N = 183).

DISCUSSION

In this study, we report a sequence of four stages of serpentinization with distinct five serpentine textures and specific chemical compositions (Fig. 8). These stages are likely indicative of a variety of fluid–rock interactions during mantle exhumation along the OCT of the Alpine Tethys. In the following, we first discuss each of the serpentinization stages in terms of local variations of temperature, pressure, fluid/rock ratio and fluid chemistry with

the aim to determine the variation of fluid–rock interactions from initial to more advance mantle exhumation, recorded from proximal to distal parts across the OCT (Fig. 19). Finally, we compare serpentinization sequences as documented at OCTs with serpentinization sequences observed at present-day MORs.

Serpentinization as a tape recorder of multi-stage mantle exhumation
Stage 1: Formation of mesh and bastite textures (serpentine S1)

Pseudomorphic serpentine mesh and bastite textures, here referred to as serpentine S1 (Fig. 8), are not only the oldest, but also the most common textures found in serpentinites from OCTs. Previous studies proposed that serpentinization at magma-poor rifted margins likely begins when the subcontinental lithospheric mantle is still capped by a thin, <6 km thick hyperextended continental crust (Manatschal, 2004; Epin et al., 2019; Hochscheid et al., 2022). Serpentinizing fluids at OCTs are assumed to reach down to ~6 km depth below seafloor through circulation along high-angle normal faults, as indicated by refraction seismic experiments (Boddupalli et al., 2022). At such depth, a combination of anisotropic thermal contraction and tectonic stresses induce micro-fractures into the mantle rocks allowing the channeling of fluids necessary for serpentinization (Rouméjon & Cannat, 2014). These micro-fractures are at the origin of a connected porosity allowing the transport of hydrothermal fluids resulting in a typical mesh texture even at low fluid/rock ratio (<F/R mass

Table 4: Representative trace element concentrations (in ppm) of serpentine minerals measured by HR-LA-ICP-MS.

Unit	Upper Platta				Lower Platta					Totalp				Tasna			
Sample	Fal 18-06 ua23	Fal 18-06 ua15	Fal 18-06 ua35	Fal 18-06 ca6	Mar 18-01 ua39	Mar 18-01 ua36	Mar 18-01 ua46	Mar 18-01 ua50	Mar 18-01 ca16	Tot 19-02 vb6	Tot 19-02 ca 49	Tot 19-02 ca.50	Tot 19-07 cb25	Tas 19-02 ub1	Tas 19-03 ub21	Tas 19-02 ub8	Tas 19-08 cb6
Texture	mesh (S1)	bastite (S1)	lamellar vein (S4)	crack-seal (S5)	mesh (S1)	bastite (S1)	banded vein (S3)	lamellar vein (S4)	crack-seal (S5)	mesh (S1)	relic cpx	spherical vein (S2)	banded vein (S3)	mesh (S1)	bastite (S1)	lamellar vein (S4)	banded vein (S3)
Type	lizardite	lizardite	antigorite	chrysotile	lizardite	lizardite	lizardite	antigorite	chrysotile	lizardite	lizardite	polyhedral	polygonal	lizardite	lizardite	antigorite	lizardite
Primary minerals	ol	opx	-	-	ol	opx	-	-	-	ol	cpx	-	-	ol	cpx	-	-
Li	2.852	13.79	11.15	13.71	3.977	2.708	4.957	2.542	12.32	0.213	3.900	2.238	1.656	7.331	26.86	6.134	0.360
B	48.30	36.63	94.50	37.92	43.63	30.92	34.86	37.34	35.25	19.43	15.16	18.49	46.74	25.12	52.70	23.74	15.94
V	5.893	76.84	10.23	4.371	17.20	85.45	17.33	29.26	9.754	6.558	163.7	7.064	7.789	111.9	129.1	18.24	18.28
Cr	136.2	3465	2.115	303.8	553.8	4809	358.4	38.20	253.0	8.755	2853	32.82	78.57	2665	4054	43.96	74.98
Co	111.0	14.58	6.678	43.83	73.56	52.54	9.357	10.96	8.970	162.3	10.79	1.272	2.187	56.96	53.00	35.88	147.6
Ni	2951	1019	210.4	708.5	1977	1053	187.5	223.6	233.2	2987	179.8	16.57	20.37	1663	909.2	1222	2897
Zn	19.17	24.32	19.00	18.16	59.07	65.87	52.24	68.98	38.80	21.99	9.710	7.109	5.471	26.82	34.97	24.24	21.39
As	2.854	0.147	1.326	0.952	1.665	1.057	0.103	0.219	0.195	n.d	0.128	0.130	0.061	0.093	0.063	<0.05	0.040
Rb	0.101	0.178	1.510	0.167	0.748	0.379	0.556	1.352	1.070	0.069	0.026	0.047	0.189	0.508	1.612	1.484	0.010
Sr	1.994	5.386	1.250	3.159	4.103	3.087	2.878	2.053	4.220	1.896	17.43	0.616	4.934	3.291	2.159	1.557	1.264
Y	0.374	2.001	0.136	0.324	0.281	0.176	0.200	0.110	0.338	0.433	12.85	0.142	0.423	1.362	1.281	0.851	0.782
Zr	0.107	3.951	0.066	0.301	0.116	0.086	0.125	0.244	0.106	0.531	10.81	0.258	1.958	0.253	0.770	0.374	0.459
Nb	0.018	0.033	0.010	0.018	0.101	0.094	0.069	0.038	0.061	0.001	0.012	0.004	0.002	0.016	0.010	0.011	0.001
Cs	0.276	0.545	4.999	0.162	0.549	0.329	0.464	1.378	0.725	n.d	0.010	0.013	0.046	1.108	1.401	4.294	0.003
Ba	0.812	3.474	0.589	1.276	1.218	0.863	0.738	0.545	1.151	0.099	0.136	0.091	0.625	0.992	0.364	0.914	0.204
La	0.064	0.057	0.041	0.049	0.299	0.155	0.151	0.071	0.126	0.008	0.108	0.003	0.008	0.031	0.002	0.019	0.001
Ce	0.197	0.252	0.144	0.143	0.397	0.308	0.293	0.153	0.235	0.056	0.774	0.011	0.035	0.078	0.018	0.066	0.007
Pr	0.031	0.040	0.021	0.028	0.039	0.025	0.029	0.015	0.024	0.013	0.212	0.003	0.007	0.012	0.010	0.010	0.004
Nd	0.149	0.233	0.116	0.144	0.136	0.087	0.110	0.045	0.095	0.065	1.605	0.025	0.044	0.097	0.074	0.062	0.054
Sm	0.042	0.115	0.028	0.054	0.029	0.026	0.010	0.011	0.024	0.028	0.865	0.007	0.020	0.049	0.060	0.032	0.041
Eu	0.062	0.054	0.039	0.081	0.088	0.050	0.054	0.033	0.081	0.008	0.346	0.010	0.010	0.020	0.039	0.017	0.014
Gd	0.065	0.226	0.031	0.085	0.032	0.019	0.019	0.009	0.042	0.045	1.393	0.033	0.044	0.111	0.119	0.100	0.090
Tb	0.008	0.049	0.004	0.018	0.004	0.003	0.004	0.002	0.009	0.010	0.302	0.009	0.009	0.031	0.028	0.016	0.016
Dy	0.055	0.354	0.016	0.071	0.034	0.019	0.021	0.018	0.043	0.059	2.158	0.024	0.066	0.232	0.195	0.129	0.107
Ho	0.010	0.080	0.004	0.010	0.007	0.005	0.005	0.003	0.010	0.015	0.485	0.005	0.019	0.057	0.048	0.032	0.027
Er	0.029	0.251	0.014	0.034	0.021	0.009	0.013	0.006	0.025	0.045	1.470	0.017	0.049	0.186	0.135	0.104	0.096
Tm	0.003	0.037	0.001	0.007	0.003	0.003	0.003	0.001	0.005	0.009	0.220	0.003	0.008	0.025	0.028	0.018	0.015
Yb	0.022	0.298	0.008	0.032	0.037	0.022	0.018	0.013	0.033	0.062	1.435	0.013	0.071	0.194	0.213	0.103	0.089
Lu	0.004	0.049	0.001	0.011	0.007	0.004	0.004	0.002	0.007	0.012	0.214	0.006	0.012	0.029	0.035	0.020	0.019
Hf	<0.003	0.145	<0.003	0.001	0.005	<0.002	0.003	0.003	0.001	0.023	0.453	0.006	0.057	0.033	0.052	0.033	0.030
Ta	<0.001	0.003	<0.001	0.006	0.002	0.001	0.002	0.002	0.037	<0.0002	0.003	<0.002	0.000	<0.0010	<0.0006	<0.0008	<0.0002
Pb	0.261	0.019	<0002	0.057	0.520	0.165	0.010	0.011	0.001	0.142	0.064	0.038	0.144	0.071	0.051	0.006	0.033
Th	0.000	0.007	0.000	0.000	0.000	0.001	0.002	0.001	0.001	0.000	0.000	0.002	0.000	0.000	0.000	0.001	0.000
U	0.001	0.002	<0.001	0.006	0.001	0.000	0.001	0.003	0.000	0.002	0.000	<0.0002	0.001	0.004	0.000	0.009	0.000
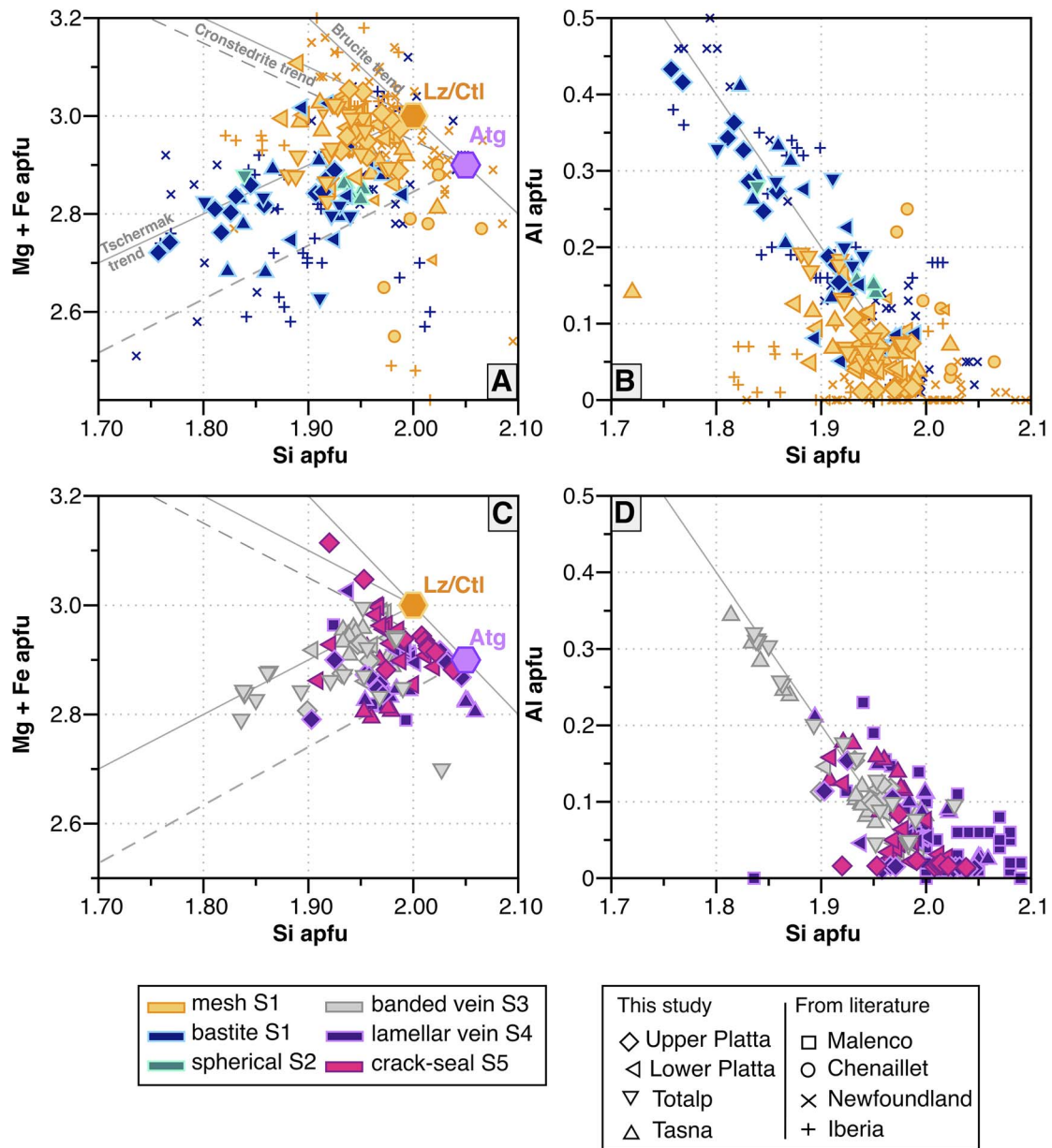
Fig. 13. A-C) Plots of Mg + Fe versus Si and B-D) Al versus Si. All cations are given in per formula units and are calculated based on 7 oxygen atoms in the serpentine formula, except for antigorite, which was calculated based on 6.823 oxygens and converted to 7 oxygens for comparison with other serpentine polysomes. Lz/Ctl: pure Mg lizardite/chrysotile endmember. Atg: pure Mg antigorite endmember. Data of Chenaillet serpentinites are from Schwartz et al., (2013) and those of Malenco antigorites are from Liu et al., (2020). Data from Iberia and newfoundland margin are from Vesin et al., (2023).

ratio 1; e.g. Moody, 1976; Wicks & Whittaker, 1977; Rouméjon & Cannat, 2014). This is evidenced by trace element patterns that mimic those of the primary minerals showing lower trace element concentrations (Fig. 16D, H). In addition, compared to mineral precursor serpentine minerals are also enriched in up to several orders of magnitude in FME (Cs, B, Li, ± Rb), evidencing an imprint of oceanic hydration. The FME enrichments in serpentine minerals from the Alpine OCT are similar to those of serpentinites from the Iberia and Newfoundland rifted margins (Kodolányi et al., 2012; Vesin et al., 2023). Experimental studies have shown that the hydrolysis of olivine is optimal at temperature <300°C, whereas orthopyroxene react faster than olivine at greater temperatures (Martin & Fyfe, 1970; Janecky & Seyfried, 1986; Allen & Seyfried Jr., 2003; Bach et al., 2004). In our partially serpentinized samples from Totalp and Tasna, relics of clinopyroxene are preserved in

both units, olivine relics are frequently observed at Totalp while it is rarely preserved in other units (Fig. 6). Similar observations were also reported by Müntener et al. (2010) for serpentinized peridotites from Upper and Lower Platta, where some relics of clinopyroxene were observed while olivine is completely serpentinized. In addition, spinel is almost free of chlorite aureoles, indicating low temperatures of serpentinization as the alteration of spinel to chlorite typically occurs at temperature above 400°C. Therefore, based on petrological evidence and the temperatures of serpentinization estimated for Iberia-Newfoundland passive margins and the Mid-Atlantic Ridge (15°20'N Fracture zone and Hess Deep; see Vesin et al., (2024) and references therein), we propose that an uppermost temperature limit of ±300°C can be assumed for this initial stage of serpentinization.
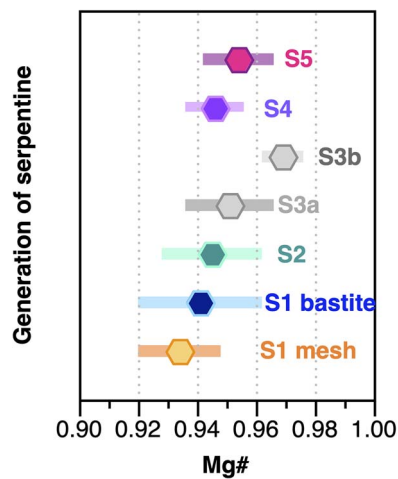
Fig. 14. Comparison of Mg# values in the suite of serpentine minerals and veins from this study, independently of their respective locations. The thick bars illustrate the typical variation range of Mg# for each serpentine polysomes.
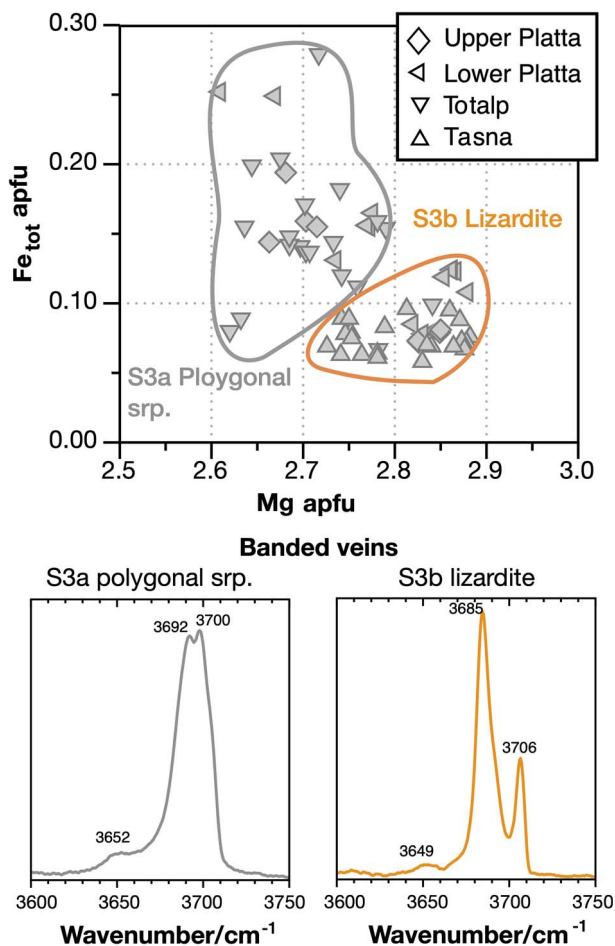
Fig. 15. Fe_{tot} versus Mg of serpentine banded veins showing two tendencies depending on the nature of the serpentine polysomes (polygonal serpentine versus lizardite).

Stage 2: Serpentine veining (serpentine S2 and S3)

Formation of polyhedral serpentine veins (S2): The first generation of veins coincides with the formation of polyhedral serpentine (S2, Fig. 8) that exhibits a typical spherical texture (Fig. 6). These veins

are mainly located in clinopyroxene relics and bastite cleavages, where a systematic association with andradite grains is reported. The S2 veins mostly occur in partially serpentinized samples, especially at Totalp, while in fully serpentinized samples S2 veins are scarce. The polyhedral serpentine (S2) veins contain significant Al (~0.16 apfu in average; Table 3). Such Al enrichment together with precipitation of andradite are consistent with the alteration of Al-rich mineral phases like clinopyroxene. Spinel and plagioclase are also important Al carriers in peridotites but the textural vicinity of polyhedral serpentine–andradite assemblage with clinopyroxene rather indicates that the latter is the source of Al. In addition, hydrothermal alteration turns spinel into ferritchromite rims and chlorite aureoles, where all Al released from spinel is consumed by the formation of chlorite (e.g. Mellini et al., 2005). Similarly, in plagioclase lherzolite from the Lower Platta unit, Al derived from plagioclase is consumed by the formation of chlorite as evidenced by petrographic observations (e.g. Müntener et al., 2010). Most trace element concentrations are significantly depleted (except for boron) in polyhedral S2 veins showing 1 to 2 orders of magnitude lower concentrations relative to bastite (S1) and primary clinopyroxene precursors (Fig. 16D, H). This suggests a high fluid/rock ratio. Therefore, it is likely that the saturation degree of the serpentinizing fluids forming polyhedral S2 veins is low. Our results agree with Andreani et al. (2008), who proposed that the formation of polyhedral serpentine veins require: (i) an open space, (ii) a temperature <200–300°C, and (iii) Al content >0.1 apfu.

Relatively to bastite (S1), polyhedral serpentine (S2) veins are enriched in Si and Mg and depleted in Ca and Fe (Fig. 13; Table 3). This may be explained by the preferential absorption of Ca and Fe by andradite (Plümper et al., 2014). The absence of magnetite associated to polyhedral serpentine (S2) veins is thus likely a consequence of andradite formation, since andradite consumes the Fe that is released either during pyroxenes serpentinization or after magnetite dissolution. Plümper et al., (2014) assume that andradite forms as a consequence of a Ca-metasomatism process in which the addition of Ca, here likely released after clinopyroxene serpentinization, destabilizes the magnetite. In addition, the oxidation of Fe for incorporation into andradite likely contributes to decrease fO_2, as proposed by Beard & Hopkinson (2000) in serpentinites from Hole 1068 (Abyssal Plain). This lowered fO_2 likely affects the stability of magnetite, which allow proposing that magnetite dissolution in favor to andradite resulted from both processes. Plümper et al., (2014) also showed that no additional source of Ca is required if the protolith contains between 8 and 12% of clinopyroxene. The subcontinental mantle exposed in the Platta, Tasna and Totalp nappes was originally composed of fertile, i.e. clinopyroxene-rich lherzolites (Müntener et al., 2010). Therefore, it is likely that serpentinization of these spinel or plagioclase lherzolites released enough Ca and Fe to form andradite synchronously with polyhedral serpentine. According to Frost & Beard (2007), the andradite + serpentine assemblage is strongly dependent on silica and calcium activities and on pH rather than temperature. However, these authors claim that a temperature range of 200–230°C is most favorable for the formation of andradite, which becomes the main Ca-bearing phase in serpentinites as long as CO_2 activity remains low, inhibiting the formation of calcite (Beard & Hopkinson, 2000; Kodolányi et al., 2012). This temperature range is consistent with that reported by Plümper et al., (2014), who showed that clinopyroxene can be replaced by an assemblage of serpentine + andradite at temperatures <280°C and low pressure (<0.5 kbar). As mentioned above, andradite is systematically observed at the rims of polyhedral serpentine, the
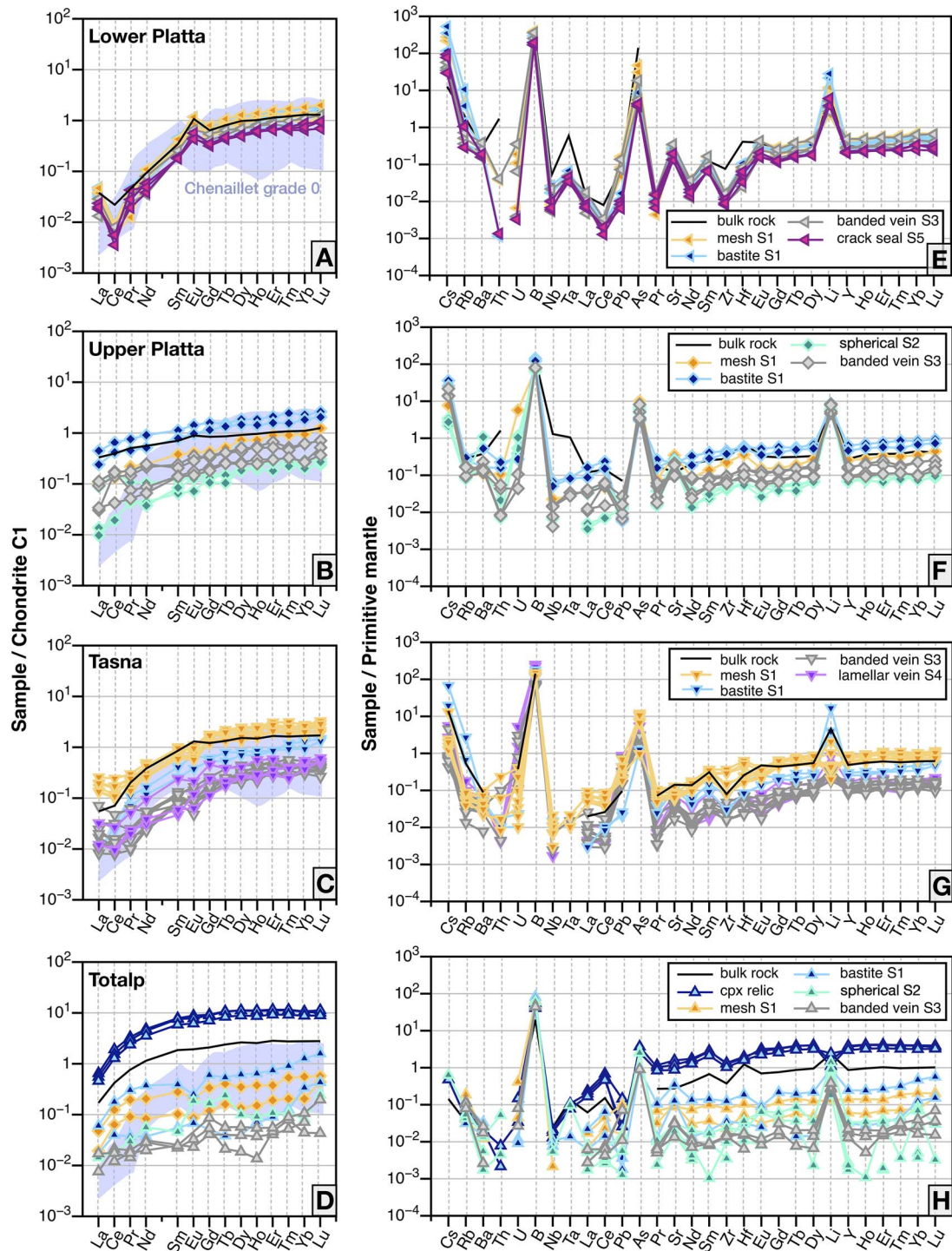
Fig. 16. Representative rare earth element (REE) patterns normalized to C1-Chondrite (left) and PM-normalized extended trace element patterns (right) of serpentine minerals and veins depending on their localities. Blue field correspond to serpentinites Grade 0 (sub-greenschist facies conditions) from the Chenaillet (data from Lafay et al., 2013).

latter mostly occurring in clinopyroxene and cpx-bastite cleavages (Fig. 6F, G).

Considering that serpentine S1 formed at ±300°C and at ≤6 km depth, serpentine S2 most likely formed shallower and under lower temperature (± 280°C, and < 5 km). The presence of andradite closely associated to polyhedral serpentine (S2) is indicative for reducing conditions as iron oxidation prior incorporation into andradite keeps fO_2 of the serpentinizing fluid relatively low and can be accompanied by considerable generation of molecular

hydrogen (Plümper *et al.*, 2014). Even if textural and chemical evidence suggests that polyhedral serpentine (S2) formed under slightly lower temperatures than serpentine S1, serpentine S2 is nevertheless assumed to develop during an early stage of fluid–rock interaction, likely soon after or simultaneously to pseudomorphic mesh and bastite S1 formation (Fig. 19B – S2).

Formation of banded veins (S3): Banded veins S3 are frequently observed crosscutting the previous serpentine generations (S1 and S2 Fig. 6, Table 1). Similar occurrences of banded veins have
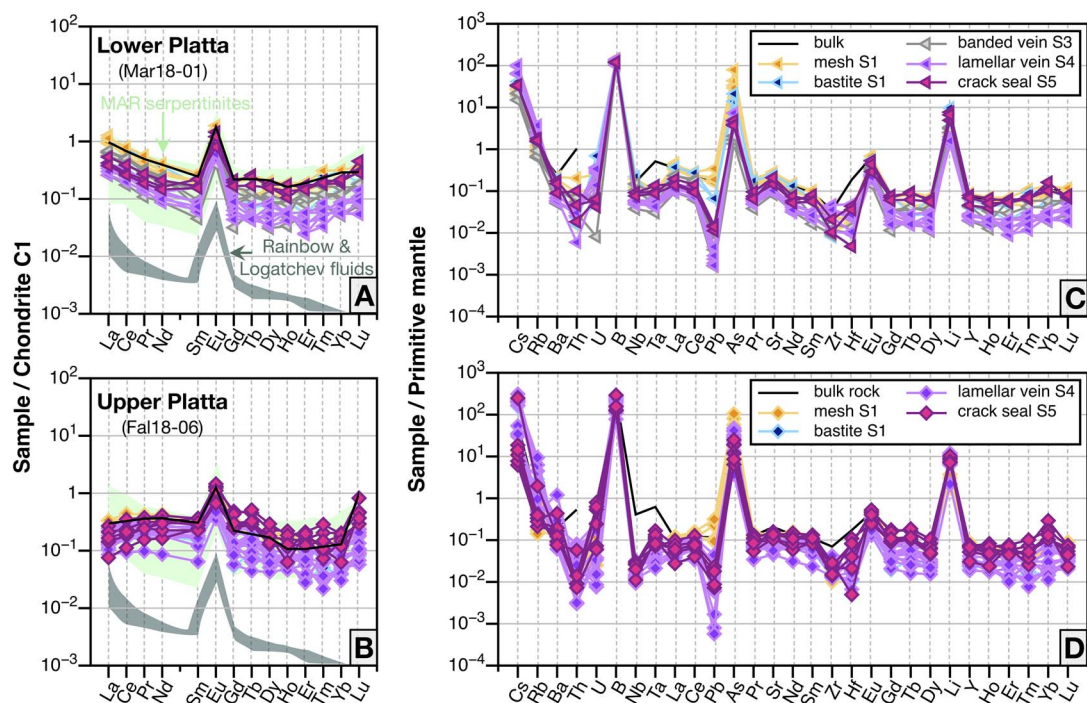
Fig. 17. Rare earth element (REE) patterns normalized to C1-Chondrite (A-C), and extended trace elements patterns normalized to Primitive mantle (B-D) of serpentine minerals and veins of two serpentinite samples for the Lower (Mar 18-01) and the Upper Platta (Fal 18-06) units, showing U-shaped patterns with strong Eu positive anomaly. The compositions of MARK serpentinites (Hole 1268A, Atlantic ridge) and hydrothermal fluids from Rainbow and Logatchev are shown for comparison (Paulick *et al.,* 2006).

been reported in oceanic serpentinites (e.g. Andreani *et al.,* 2004; Andréani *et al.,* 2007; Rouméjon *et al.,* 2015). The nature of the filling serpentine polysomes, however, can evolve from an unstable (proto-serpentine, chrysotile, polygonal) to a more stable serpentine polymorph (lizardite) as suggested by experimental studies of Grauby *et al.* (1998) and Normand *et al.* (2002) and recently strengthened by Raman spectroscopy on naturals samples (Tarling *et al.,* 2021). At sufficient degree of supersaturation (i.e. open system), several metastable phases like chrysotile may crystallize (Normand *et al.,* 2002). However, if the degree of supersaturation of the fluid is not maintained sufficiently high, the transition from a metastable to a more stable form (i.e. chrysotile - > polygonal - > lizardite) can occur spontaneously (Viti & Mellini, 1997; Normand *et al.,* 2002).

In our samples, banded veins (S3) are mostly made of lizardite and polygonal serpentine, whereas chrysotile remains scarce. The banded veins made of polygonal serpentine contains more Fe_{tot} and less Mg than banded veins made of lizardite (Fig. 14). Therefore, we attribute this isochemical evolution to the decreasing degree of supersaturation of the solution with respect to serpentine in a response to an increase of fluid/rock ratios, and a longer interaction time with the serpentinizing fluid as proposed by Normand *et al.* (2002) and Andréani *et al.* (2007). This is also supported by lower concentrations of most trace elements compared to the primary mesh and bastite S1, accompanied by an increase in FME like B (Fig. 16). According to Andréani *et al.* (2007), we propose that the formation of these banded veins (S3) begins when the ultramafic rocks are almost fully serpentinized, at shallower depth than the first two serpentine generations (S1 and S2), likely at <3 km depth along a detachment fault (Gillard *et al.,* 2019). At this point, there is not enough results to discriminate if the banded veins attested of crack opening due to: i) an accommodation of volume expansion due to serpentinization, or ii) the

incremental stress release during unroofing of serpentinites (e.g. Ramsay, 1980; O'Hanley, 1992; Andreani *et al.,* 2004).

Stage 3: Local overpressure and/or SiO_2-rich fluid circulation – Formation of antigorite (S4)

Antigorite (S4) was identified in some fully serpentinized samples from Upper Platta, Tasna and in one sample from Lower Platta. It mostly occurs as patches, replacing the mesh texture, or as veins opening in all directions (Fig. 7A). Locally, these veins opened in pull-apart mode, showing a close relation with small chrysotile fibers (Fig. 7B). This is highlighted by the Raman spectra signature of antigorite (S4), which is systematically a mixture between serpentine chrysotile and antigorite, with typical peaks at 3670 cm^{-1}, 3690 cm^{-1} and 3700 cm^{-1} (Fig. 7). In addition, antigorite (S4) is frequently crosscut by later chrysotile crack-seal (S5) (Fig. 7D). Those antigorite veins may have been initially filled with chrysotile, suggesting the replacement of the latter by the former. Such replacement was also documented in samples from MORs (Hébert *et al.,* 1991; Kodolányi *et al.,* 2012; Klein *et al.,* 2017; Ribeiro Da Costa *et al.,* 2008; Rouméjon *et al.,* 2015, 2019) and the Guatemala forearc (Kodolányi & Pettke, 2011). In Alpine ophiolites, antigorite is mostly considered as a fingerprint of Alpine prograde metamorphism (Dietrich, 1969; Burkhard & O'Neil, 1988; Scambelluri *et al.,* 1995; Früh-Green *et al.,* 2001; Debret *et al.,* 2013; Lafay *et al.,* 2013; Piccardo, 2013; Liu *et al.,* 2020), and was, for long time, considered to be an evidence of HT-HP conditions of formation of serpentine (e.g. Ulmer & Trommsdorff, 1995; Wunder & Schreyer, 1997; Evans, 2004). Thus, high fluid–rock interaction temperatures and an additional heat source linked to melt emplacement (e.g. Beard *et al.,* 2009; Frassi *et al.,* 2022) have been invoked to explain antigorite at spreading ridges. However, neither evidence for the former nor the latter have been found at the Tasna and Upper Platta. At both units, where antigorite is observed, magmatic

additions are extremely rare and are not observed in the vicinity of the sample locations. In contrast, at lower Platta, where numerous gabbroic bodies and mafic dikes intruded the mantle, antigorite is absent, except of one sample. Therefore, the antigorite formation in our samples can hardly be attributed to the heat released by melt intrusions.

Alternatively, antigorite occurrences at Hess Deep (East Pacific Rise; Rouméjon *et al.,* 2019), Atlantis Massif (Mid-Atlantic Ridge, MAR; Rouméjon *et al.,* 2018, 2019), Puerto Rico Trench (Klein *et al.,* 2017) and the Southwest Indian Ridge (SWIR; Rouméjon *et al.,* 2015) were explained by interaction of the predating serpentine with Si-rich hydrothermal fluids derived from the alteration of mafic bodies (dikes and gabbros) or pyroxenes. Linking the antigorite formation to Si-metasomatism of mafic magmatic additions is hardly reconciled with observations and data from Tasna and Upper Platta, since such rocks are not observed in the field. However, peridotites from both Tasna and Upper Platta are pyroxene-rich, and at both sites pyroxenes are largely replaced by serpentine (Fig. 6). Therefore, the silica released after pyroxene alteration may have contributed to the formation of antigorite, which is consistent with the fact that some samples plot below the peridotite melting residue line in Fig. 10. Kodolányi & Pettke (2011) provided a detailed study on the major role played by SiO_2 during the chrysotile to antigorite transition. The authors suggest that if no brucite is produced during antigorite formation, either SiO_2 addition or Mg and Fe removal are needed to balance antigorite growth at the expense of chrysotile. This can explain the absence of brucite in our samples. Another hypothesis is that the chrysotile/lizardite-to-antigorite transition is linked to deformation or fluid infiltration. Ribeiro Da Costa *et al.,* (2008) argued that chrysotile could be replaced by antigorite through a dissolution-recrystallization process favored by intense shearing stress at relatively low temperatures (<300°C). Alternatively, Kodolányi & Pettke (2011) proposed also that the replacement of chrysotile by antigorite occurred by dissolution (and precipitation) at T ~ 300°C due to fluid infiltration (i.e. fluid-assisted chrysotile–antigorite transition). The recent discovery of seismic events in the footwall of oceanic core complexes showing compressional focal mechanisms (Parnell-Turner *et al.,* 2017) may reflect a small amount of shortening due to the plate unbending at very shallow levels along an exhumed detachment fault (see also model of Sandiford *et al.,* 2021). Therefore, we can barely exclude that local shortening during unbending of the downward concave detachment resulting in local overpressure did not affect the replacement of lizardite/chrysotile by antigorite, although we agree that this transition is rather promoted by (SiO_2-rich) fluid circulation.

The transition from oceanic serpentine to antigorite formed in subduction zones is accompanied by a strong mobility of some trace elements, in particular fluid mobile elements (FME) like B, Li, Cs and Sr (e.g. Deschamps *et al.,* 2012; Peters *et al.,* 2017, Pettke & Bretscher, 2022). A loss of such elements was documented in several places in the Alps, such as the Lanzo Massif (Debret *et al.,* 2013) or the Piedmont zone (Chenaillet–Queyras–Montviso; Lafay *et al.,* 2013) of the Western Alps. These elements are transferred to the mantle wedge during the lizardite to antigorite transition. The ophiolitic nappes in Eastern Switzerland and Northern Italy, i.e. Totalp, Platta and Malenco discussed here (Fig. 1C), recorded a prograde and increasing Alpine metamorphism from north to south (Peters & Mathews, 1963; Dietrich, 1969, 1970; Vils *et al.,* 2011). These units remained, however, in the hanging wall of the subduction zone and were not subducted, preserving them from high P–T conditions. This suggests that Alpine serpentinization, if it existed in any of these units, remained rare (Manatschal
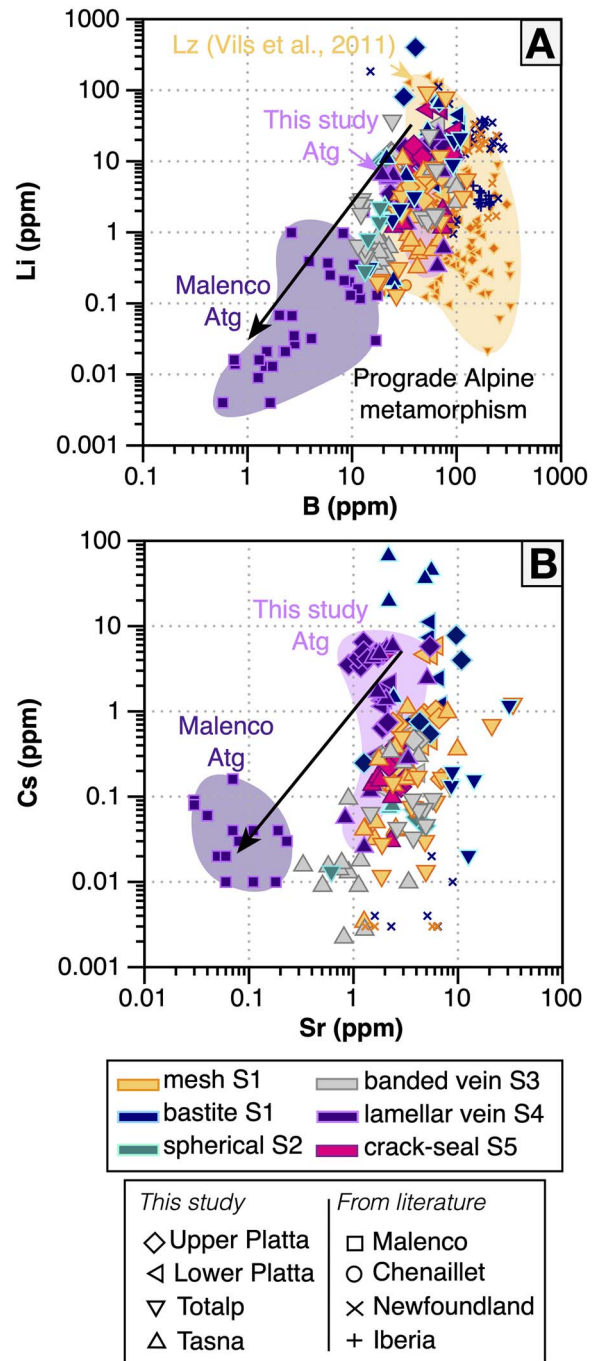
Fig. 18. (A) Li versus B and (B) Cs versus Sr (μg/g) in the suite of serpentine minerals and veins from this study compared to other serpentinites from the Alps (Malenco Liu *et al.,* (2020), Chenaillet Lafay *et al.,* (2013) and from Iberia margin and Newfoundland margin from (Kodolányi *et al.,* 2012 and Vesin *et al.,* 2023). The two black arrows illustrate the depletion trend of FME during the prograde Alpine metamorphism.

and Müntener, 2006; Picazo *et al.,* 2013). This may explain why antigorite from Upper Platta and Tasna displays no depletion in FME in contrast to the subducted serpentinites, and why it shows concentrations of B, Li, Cs and Sr within the range of earlier serpentines (S1 to S3; Fig. 18). In addition, the shapes of the antigorite spider-diagrams are also comparable to patterns of serpentine mesh within a sample, albeit with an order of magnitude of depletion (Figs. 16 and 17).

These results are much in favor of a formation of the antigorite by recrystallization of earlier serpentine generations during mantle exhumation, promoted by SiO_2-rich fluid circulation, as stated above, rather than a subduction-derived origin. This recrystallization may be accompanied by magnetite dissolution, which could explain why magnetite is so scarce in association with antigorite (Fig. 7A). Based on constant Mg# measured in serpentine mesh and antigorite in abyssal peridotites, Rouméjon et al., (2019) postulated that antigorite does not integrate additional iron, even if magnetite is dissolved with mesh. However, a constant increase in Mg# is observed in our samples from S1 to S3 (Fig. 14), while Mg# decreases in antigorite (S4), suggesting that slight amount of iron may be integrated in antigorite veins and patches during serpentine mesh recrystallization.

Stage 4: Stress relaxation—Formation of crack-seal (S5)

Chrysotile crack-seal (S5) are the last generation of serpentine veins and are ubiquitous in our samples. They are also commonly recognized as the latest serpentinization event during mantle exhumation at MORs (e.g. Andréani et al., 2007; Rouméjon et al., 2015, 2018). Evans (2004) proposed that formation of cross-fiber chrysotile (i.e. crack-seal S5) is not really different from slip-fiber chrysotile (i.e. banded veins S3), although the latter is promoted by the presence of fluids rather than shear stress. We propose that the formation of chrysotile crack-seal (S5) occurred mainly at shallower depths than banded veins, but probably in similar levels than antigorite (S4). They are certainly formed as the consequence of late strain release during mantle exhumation at seafloor.

Serpentine REE compositions: Evidence of fluid-dominated systems

Serpentine REE compositions mostly reflect those of their magmatic mineral precursors (olivine, clinopyroxene and orthopyroxene; see Figs. 16 and 17 and supplementary materials). Regarding the REE compositions of serpentinite whole rocks, they cover the range of peridotite compositions reported by Müntener et al. (2010). The variation of the $(La/Sm)_N$ ratio from primitive-like to highly depleted signatures is due to variable degrees of partial melting or refertilization by syn-rift melt percolation (case of Lower Platta peridotites). It is a pre-serpentinization feature, consistently with what was documented along the Iberia passive margin (Kodolányi et al., 2012; Vesin et al., 2023). Hence, REE contents of serpentinite samples are inherited from the magmatic processes that affected the subcontinental mantle prior its exhumation at seafloor. Interestingly, two samples from the Lower and the Upper Platta units show particular U-shaped REE patterns with a strong positive Eu anomaly (Fig. 17). Similar patterns were reported in oceanic serpentinites, and two main processes have been proposed in the literature: (i) plagioclase crystallization during melt percolation (i.e. refertilization process; Müntener et al., 2004, 2010; Rampone et al., 1998, 2020); or (ii) large fluid-fluxes during serpentinization (Paulick et al., 2006). Regarding the first assumption, the crystallization of melt-derived plagioclase could be consistent with the formation of LREE-enriched serpentinites in the Lower Platta unit since the latter was largely impregnated by melts during Jurassic rifting (Müntener et al., 2004). However, this explanation cannot account for serpentinites from the Upper Platta, since this unit remained preserved from syn-rift melt percolation (Müntener et al., 2010). Therefore, serpentinization was likely responsible of the U-shape REE pattern which, by comparison, resembles those black smokers (e.g. Rainbow and Logatchev, Fig. 17; Klinkhammer et al., 1994; Douville et al., 2002).

Paulick et al., (2006) proposed that such shapes in serpentines are only possible under very high fluid/rock ratios so that the LREE concentration is entirely controlled by the fluid, erasing the LREE-depleted character of the protolith. At the opposite, HREE are less affected since their concentrations in hydrothermal fluids are negligible relative to the initial peridotite. Accordingly, the U-shape patterns observed in two serpentinites may resulted from intense fluid–rock interactions, similar to some mature hydrothermal systems described along MOR (Paulick et al., 2006). This inference is consistent with the recent discovery of a well-preserved fossil ultramafic-hosted hydrothermal system, namely the Marmorera-Cotschen hydrothermal system in the Lower Platta unit (i.e. distal domain; Coltat et al., 2019, 2021; Hochscheid et al., 2022).

Serpentinization across the OCT

Contrasting serpentinization from proximal to distal domains in the OCT

An important result of this study is that the full sequence of all serpentine generations (S1 to S5) is only observed in the proximal part of the OCT at Upper Platta and Tasna (Fig. 19C). In contrast, at the Lower Platta, which is derived from a more distal part of the OCT, only serpentine (S1) and chrysotile crack-seal (S5) can be observed (Fig. 19C). Interestingly, serpentinites from the Chenaillet unit, which is interpreted to be located more oceanward (distal) than the Lower Platta unit (see Fig. 1D), is dominated by mesh ± bastite textures (S1) and devoid of serpentine veins (Lafay et al., 2013; Schwartz et al., 2013). This suggests that intensity of veining in serpentinites decreases oceanwards. Possible controlling factors are: (i) mantle composition, which changes from proximal to distal from spinel to plagioclase lherzolites (Müntener et al., 2004, 2010), and (ii) thermal gradients and presence of magma, which increase from proximal to distal. Both may account for a different rheology of the serpentinized basement and different composition of secondary minerals (e.g. Klein et al., 2013). Likewise, local magmatic intrusions could potentially increase the temperature of serpentinization and change the serpentinization rates (e.g. Rimstidt et al., 2012) and thus the degree of serpentinization at the distal domain. However, there is no difference in mineralogy nor degree of serpentinization between samples from the proximal and distal OCT, allowing us to propose that mantle composition and temperature seem not to be the main factors controlling the presence of serpentine generations. Alternatively, intensity of veining and the occurrence of serpentine generations (S1 to S5) may be linked to the mechanism of mantle exhumation. Indeed, Sauter et al. (2013), Epin & Manatschal (2018); Epin et al. (2019), Reston (2018), and Gillard et al. (2019) showed that mantle exhumation processes differ from proximal to distal domains of the OCT and at MORs. While at proximal OCTs mantle exhumation is mainly controlled by large offset detachment faults, at distal domains fault offsets tend to decrease and a transition to out-of-sequence detachments, and flip-flop faulting is observed. As a consequence, in the proximal domain (e.g. Tasna and Upper Platta) continuous mantle exhumation sequences, favor the development of all serpentine generations S1 to. In contrast, sequential flip-flop faulting or out of sequence detachment faulting at distal domains (i.e. Lower Platta) have the tendency to omit the development of intermediary serpentine generations (S2, S3 S4), allowing solely the development of the initial (S1) and final (S5) serpentine generations (Fig. 19B). It is, therefore, conceivable that the local absence of the intermediate serpentine (S2 to S4) at more distal domains (e.g. Chenaillet; proto-oceanic domain, Fig. 1D) reflects the involvement of flip-flop detachment

faults (i.e. flip-flop exhumation mode, Fig. 19A). This is also in line with the studies of Reston & McDermott, (2011), Epin *et al.* (2019), Gillard *et al.* (2019) and Theunissen & Huismans (2022) showing evidence that mantle exhumation processes are undoubtedly more complex and discontinuous at distal parts of OCTs. Our simple model shown in Fig. 19 proposes that occurrence of all serpentine generations S1 to S5 indicates exhumation along one single exhumation fault, while complicated, polyphase flip-flop systems have the tendency to omit intermediate generations (S2 to S4).

Exceptions to this model may exist. At Totalp, that belongs to the proximal OCT, not all serpentine generations are observed. The mantle rocks in this unit are particularly well preserved, displaying serpentinization degrees ~60%. This is expected to occur for peridotites located near a fossil hydration front, in a rock-dominated hydration system. Serpentines consist essentially of lizardite in pseudomorphic mesh and bastite (S1), polyhedral serpentine (S2) inside orthopyroxene cleavages and few banded veins (S3). The low degree of serpentinization may also indicate that only small amounts of fluid penetrated the mantle, which could explain the absence of some serpentine generations (S3 to S5, Fig. 19C). Limited fluid–rock interactions at Totalp are also evidenced by very low FME concentrations (except B, Sb and Li) in bulk rock (Fig. 11).

Serpentinization at OCT and MOR: Similarities and differences

Mantle exhumation is a common process at slow and ultra-slow spreading centers and at OCTs of magma-poor rifted margins (e.g. Cannat, 1993; Blackman *et al.*, 2002; Cannat *et al.*, 2009; Sauter *et al.*, 2013). Recent studies have proposed that at ultra-slow MOR settings, mantle exhumation involves successive detachment faults (flip-flop model; Sauter *et al.*, 2013 along the SWIR) similarly to distal parts of OCTs (e.g. Iberia-Newfoundland; Reston & McDermott, 2011, Theunissen & Huismans, 2022), Australia-Antarctica (Gillard *et al.*, 2016) and Lower Platta (Epin *et al.*, 2019). In contrast to ultra-slow spreading systems and distal OCTs, at slow spreading MORs and proximal OCTs flip-flop detachment systems have not so far been identified (Cannat *et al.*, 2019; Epin *et al.*, 2019).

Similarities in hydrothermal processes and conditions of serpentinization at slow to ultra-slow MORs and OCT are suggested by the occurrence of similar serpentine polysomes. Studies at 30°N (Atlantis massif; Rouméjon *et al.*, 2018), 23°N (the Kane fracture zone, MARK area Dilek *et al.*, 1997; Andréani *et al.*, 2007), and along the (slow) MAR, at 62–65°E, as well as along the SWIR corresponding to a magma-poor end-member of an ultra-slow MOR (Rouméjon & Cannat, 2014; Rouméjon *et al.*, 2015) show similarities with observations made at serpentinites from the Iberian OCT (Agrinier *et al.*, 1996; Beard & Hopkinson, 2000, Kodolányi *et al.*, 2012; Vesin *et al.*, 2023). All studies revealed that serpentinites recorded multiple serpentinization events, involving a large variety of serpentine veins, textures and polysomes. However, the proportion, morphology and texture of serpentine veins can differ depending on the setting. Along the SWIR 62–65°E and the Atlantis Massif (hole M0076B; Rouméjon *et al.*, 2015, 2018) described very similar serpentine sequences with the same serpentine polysomes to those reported at proximal OCT domains (Upper Platta, Tasna) reported in this study. This supports the idea that the presence or absence of serpentine generations are not controlled by the conditions of serpentinization (temperature and composition of mantle peridotites) but more likely by the mecha-

nisms of mantle exhumation, i.e. exhumation along a single large offset fault vs along flip-flop faults (see model in Fig. 19). This is also supported by observations made along the SWIR, where mantle exhumation occurred during the past 7–10 Myr by flip-flop faulting (Sauter *et al.*, 2013). As predicted by our model, only a minor part (~25%) of the analyzed samples are overprinted by several serpentine veins (Rouméjon *et al.*, 2015, 2018) with most of the samples composed only by pseudomorphic mesh and bastite textures (S1). Similar observations were also reported from the Atlantis Massif (Rouméjon *et al.*, 2015, 2018).

Polyhedral serpentine: A fingerprint of OCTs?

A substantial difference between OCTs and MORs is the composition of the peridotites undergoing serpentinization. The nature of mantle constituting the OCT typically consists of spinel and plagioclase lherzolites, while at MORs the mantle is mostly harzburgitic (e.g. Andréani *et al.*, 2007; Rouméjon *et al.*, 2018). One notable difference in the serpentine paragenesis between OCT and MOR settings is the occurrence of polyhedral serpentine. In our samples, polyhedral serpentine occurs either in veins crosscutting the mesh texture or in alteration of pyroxenes, while it was not reported in Atlantis massif serpentinites and expected to occur rarely (<15%) in latest serpentine veins at SWIR (Rouméjon *et al.*, 2015, 2018). In serpentinites from MARK, however, serpentine polyhedral is described as the latest generation of veins (Andréani *et al.*, 2007; Andreani *et al.*, 2008). According to Andreani *et al.* (2008), all Fe in polyhedral serpentine is ferrous, which is in favor of a formation under reducing conditions. This is, therefore, more consistent with a formation at depth rather than close to the seafloor, where oxidizing conditions are more likely. Its close association with andradite, as reported above, is also in favor of reducing conditions (Plümper *et al.*, 2014).

The reason why polyhedral serpentine formed deeper in OCT serpentinites relative to those at MOR is thus unclear. A possible explanation could be the availability of Al that may control the formation of polyhedral serpentine (Andreani *et al.*, 2008). The nature of the protolith may thus play a role in the early crystallization of polyhedral serpentine. The OCT peridotites from the Alps are fertile lherzolites that are up to three to four times more enriched in Al than the harzburgites that outcrop mainly at MAR and SWIR (Fig. 9). In lherzolite, Al is mainly stored in clinopyroxene, spinel and occasionally plagioclase. As in the distal OCT lherzolite was refertilized by melt percolation, forming secondary clinopyroxene-plagioclase assemblage. As stated above (section 5.1.2), we postulate that Al released during spinel and plagioclase alteration is unlikely to contribute to the formation of polyhedral serpentine. Rather, we assume that clinopyroxene contains enough Al to form polyhedral serpentine. This is consistent with the systematic observation of polyhedral at the vicinity of clinopyroxene relics. Consequently, we assume that OCT lherzolites are more suitable to form polyhedral serpentine and associated andradite at early time of serpentinization relative to MOR harzburgites where Al and Ca are significantly more depleted. The distribution of serpentine generations (S1 to S5) occurring in exhumed mantle rocks depend on the exhumation mode (e.g. long-offset vs flip-flop). The development of polyhedral serpentine in the early stages of serpentinization may be related to the fertility of the protolith.

CONCLUSION

In this study, we present new petrological and geochemical investigations of 18 serpentinized peridotites out of a set of 40 samples
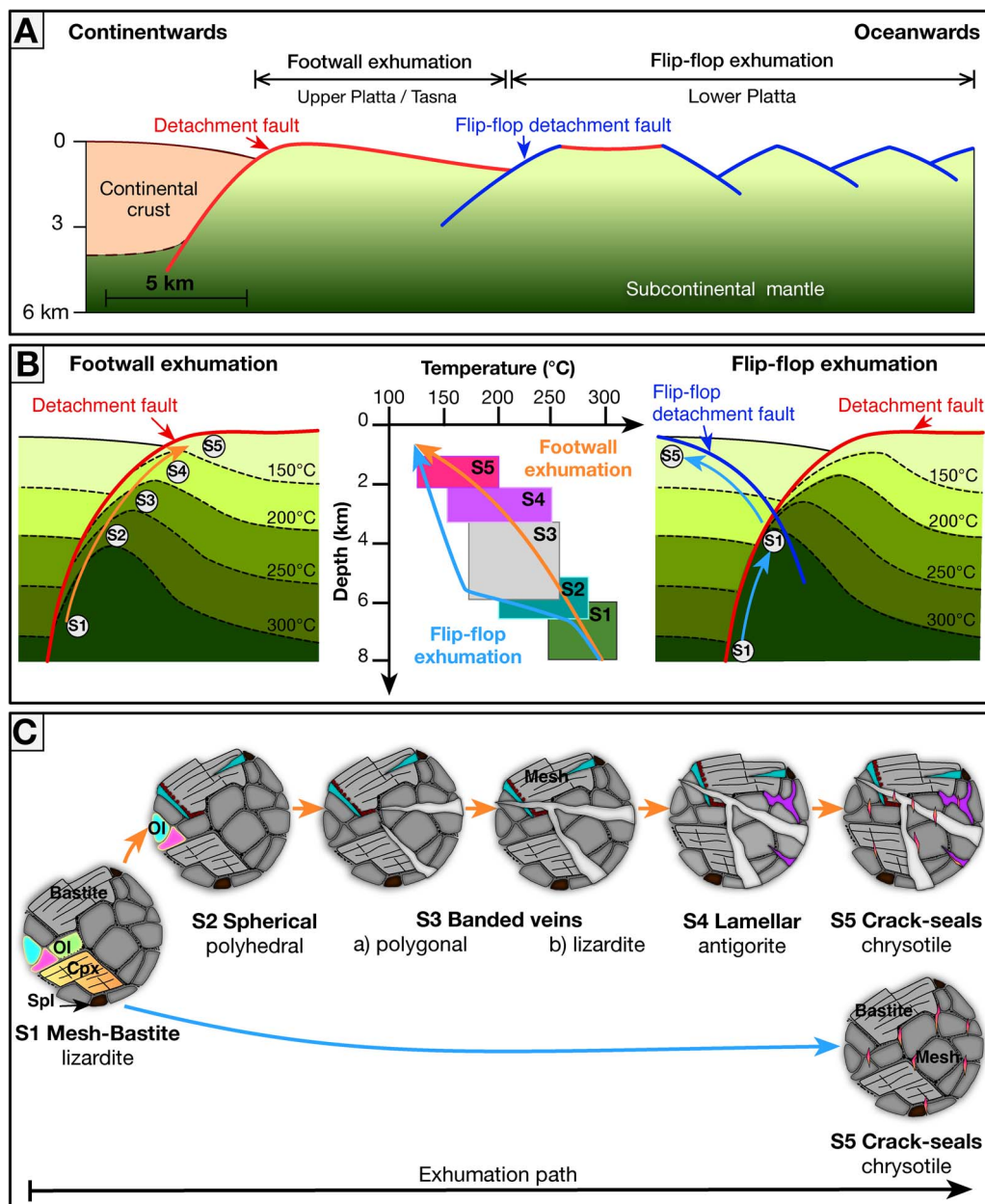
Fig. 19. (A) Simplified cross-section across an ocean continent transition (OCT) highlighting a long detachment fault continentwards (red) and flip-flop faults (blue) oceanwards (Figure modified from Gillard et al., 2016). (B) Conceptual model proposed for the footwall vs. flip-flop mantle exhumation in OCT and the related (C) type sequence of serpentinization: At proximal domains of the OCT, mantle exhumed along a continuous detachment fault, from ±6 km depth up to the seafloor, favors intense fluid–rock interactions and the development of a complete serpentinization sequence. At distal domains of the OCT, the mantle is exhumed discontinuously through asymmetric detachment faults (flip-flop). At this setting, one or more serpentine generations are missing, forming an incomplete serpentinization sequence.

collected in the OCT of the former Alpine Tethys, nowadays exposed in the Central Alps in SE Switzerland. Our results show that serpentinites record complex serpentinization sequences, resulting of successive episodes of fluid–rock interactions related to the progressive mantle exhumation. Four stages of serpentinization are identified giving rise to five serpentine generations with first pseudomorphic serpentine mesh and bastite made of lizardite (S1), which are then crosscut by several serpentine veins with different vein textures and serpentine polysomes (S2 to S5). These include spherical polyhedral serpentine (S2), banded (chrysotile ± polygonal ± lizardite) serpentine veins (S3), lamellar antigorite veins and patches (S4) and chrysotile crack-seal (S5). A major observation is that while in proximal (i.e. continentwards)

parts of the OCT all serpentine sequences were formed (S1 to S5), in distal domains (i.e. oceanwards) of the OCT only the initial and final serpentine generations (S1 and S5) can be found. We explain this observation with a simple model (Fig. 19), suggesting that omission of intermediate serpentinization stages (S2 to S4) is reflecting a change in the mechanisms of mantle exhumation. In this model, a complete serpentinization sequence (S1 to S5) is formed, if the mantle is exhumed continuously along a single large offset detachment fault, as is the case at proximal domains of OCTs or at some oceanic core complexes at slow-spreading ridges. At the opposite, an incomplete serpentinization sequence (S1 and S5) is recorded where mantle exhumation process is discontinuous and controlled by either out-of-sequence

detachments or flip-flop faults as is the case at distal OCTs or ultra-slow spreading centers. Our model can explain why serpentinization sequences observed at proximal OCTs present close similarities with those observed at large offset faults at slow MORs as well as the similar observations made at distal OCTs and ultra-slow MORs. Our study suggest that formation of serpentine generations is controlled by the mode of exhumation (i.e. continuous vs discontinuous), while the formation of each serpentine generation is controlled by the conditions of serpentinization, (i.e. temperature and pressure, composition of mantle peridotites, fluid rock ratios).

SUPPLEMENTARY DATA

Supplementary data are available at Journal of Petrology online.

DATA AVAILABILITY

The data underlying this article are available in the article and in its online supplementary material.

REFERENCES

Agrinier, P. & Cannat, M. (1997). Oxygen-isotope constraints on serpentinization processes in ultramafic rocks from the mid-Atlantic ridge (23 N). *Notes* **47**, 95–91.

Agrinier, P., Cornen, G., Beslier, M. O. & Whitmarsh, R. B. (1996) Mineralogical and oxygen isotopic features of serpentinites recovered from the ocean/continent transition in the Iberia Abyssal Plain. In: *Proceedings-Ocean Drilling Program, 149 Scientific Results*. College Station, TX, USA, 541–552.

Albers, E., Bach, W., Pérez-Gussinyé, M., McCammon, C. & Frederichs, T. (2021). Serpentinization-driven H2 production from continental break-up to mid-ocean ridge spreading: unexpected high rates at the West Iberia margin. *Frontiers in Earth Science* **9**, 673063. https://doi.org/10.3389/feart.2021.673063.

Allen, D. E. & Seyfried, W. E., Jr. (2003). Compositional controls on vent fluids from ultramafic-hosted hydrothermal systems at mid-ocean ridges: an experimental study at 400 C, 500 bars. *Geochimica*

et Cosmochimica Acta **67**(8), 1531–1542. https://doi.org/10.1016/S0016-7037(02)01173-0.

Amann, M., Ulrich, M., Manatschal, G., Pelt, E., Epin, M. E., Autin, J. & Sauter, D. (2020). Geochemical characteristics of basalts related to incipient oceanization: the example from the Alpine-Tethys OCTs. *Terra Nova* **32**(1), 75–88. https://doi.org/10.1111/ter.12438.

Andreani, M., Baronnet, A., Boullier, A. M. & Gratier, J. P. (2004). A microstructural study of a "crack-seal" type serpentine vein using SEM and TEM techniques. *European Journal of Mineralogy* **16**(4), 585–595. https://doi.org/10.1127/0935-1221/2004/0016-0585.

Andréani, M., Mével, C., Boullier, A. M. & Escartin, J. (2007). Dynamic control on serpentine crystallization in veins: constraints on hydration processes in oceanic peridotites. *Geochemistry, Geophysics, Geosystems* **8**(2). https://doi.org/10.1029/2006GC001373.

Andreani, M., Grauby, O., Baronnet, A. & Muñoz, M. (2008). Occurrence, composition and growth of polyhedral serpentine. *European Journal of Mineralogy* **20**(2), 159–171. https://doi.org/10.1127/0935-1221/2008/0020-1801.

Aumento, F., & Loubat, H. (1971). The Mid-Atlantic ridge near 45 N. XVI. Serpentinized ultramafic intrusions. *Canadian Journal of Earth Sciences*, **8**(6), 631–663.

Auzende, A. L., Daniel, I., Reynard, B., Lemaire, C. & Guyot, F. (2004). High-pressure behaviour of serpentine minerals: a Raman spectroscopic study. *Physics and Chemistry of Minerals* **31**, 269–277. https://doi.org/10.1007/s00269-004-0384-0.

Bach, W., Garrido, C. J., Paulick, H., Harvey, J. & Rosner, M. (2004). Seawater-peridotite interactions: first insights from ODP Leg 209, MAR 15 N. *Geochemistry, Geophysics, Geosystems* **5**(9). https://doi.org/10.1029/2004GC000744.

Bach, W., Paulick, H., Garrido, C. J., Ildefonse, B., Meurer, W. P. & Humphris, S. E. (2006). Unraveling the sequence of serpentinization reactions: petrography, mineral chemistry, and petrophysics of serpentinites from MAR 15 N (ODP Leg 209, Site 1274). *Geophysical Research Letters* **33**(13). https://doi.org/10.1029/2006GL025681.

Bach, W., Rosner, M., Jöns, N., Rausch, S., Robinson, L. F., Paulick, H. & Erzinger, J. (2011). Carbonate veins trace seawater circulation during exhumation and uplift of mantle rock: results from ODP Leg 209. *Earth and Planetary Science Letters* **311**(3–4), 242–252. https://doi.org/10.1016/j.epsl.2011.09.021.

Barnes, J. D., Paulick, H., Sharp, Z. D., Bach, W. & Beaudoin, G. (2009). Stable isotope (δ18O, δD, δ37Cl) evidence for multiple fluid histories in mid-Atlantic abyssal peridotites (ODP Leg 209). *Lithos* **110**(1–4), 83–94. https://doi.org/10.1016/j.lithos.2008.12.004.

Beard, J. S. & Frost, B. R. (2017). The stoichiometric effects of ferric iron substitutions in serpentine from microprobe data. *International Geology Review* **59**(5–6), 541–547. https://doi.org/10.1080/00206814.2016.1197803.

Beard, J. S. & Hopkinson, L. (2000). A fossil, serpentinization-related hydrothermal vent, Ocean Drilling Program Leg 173, site 1068 (Iberia Abyssal Plain): some aspects of mineral and fluid chemistry. *Journal of Geophysical Research: Solid Earth* **105**(B7), 16527–16539. https://doi.org/10.1029/2000JB900073.

Beard, J. S., Frost, B. R., Fryer, P., McCaig, A., Searle, R., Ildefonse, B. & Sharma, S. K. (2009). Onset and progression of serpentinization and magnetite formation in olivine-rich troctolite from IODP Hole U1309D. *Journal of Petrology* **50**(3), 387–403. https://doi.org/10.1093/petrology/egp004.

Bernoulli, D. & Weissert, H. (1985). Sedimentary fabrics in Alpine ophicalcites, south Pennine Arosa zone, Switzerland. *Geology* **13**(11), 755–758. https://doi.org/10.1130/0091-7613(1985)13<755:SFIAOS>2.0.CO;2.

Beslier, M. O., Royer, J. Y., Girardeau, J., Hill, P. J., Boeuf, E., Buchanan, C. & Thomas, S. (2004). A wide ocean-continent transition along

the south-west Australian margin: first results of the MAR-GAU/MD110 cruise. *Bulletin de la Société Géologique de France* **175**(6), 629–641. https://doi.org/10.2113/175.6.629.

Blackman, D. K., Karson, J. A., Kelley, D. S., Cann, J. R., Früh-Green, G. L., Gee, J. S. & Williams, E. A. (2002). Geology of the Atlantis Massif (Mid-Atlantic Ridge, 30 N): implications for the evolution of an ultramafic oceanic core complex. *Marine Geophysical Researches* **23**, 443–469. https://doi.org/10.1023/B:MARI.0000018232.14085.75.

Boccaletti, M., Elter, P., & Guazzone, G. (1971). Plate tectonic models for the development of the Western Alps and Northern Apennines. *Nature Physical Science*, **234**(49), 108–111.

Boddupalli, B., Minshull, T. A., Bayrakci, G., Lymer, G., Klaeschen, D. & Reston, T. J. (2022). Insights into exhumation and mantle hydration processes at the deep Galicia margin from a 3D high-resolution seismic velocity model. *Journal of Geophysical Research: Solid Earth* **127**(7), e2021JB023220.

Boillot, G., Grimaud, S., Mauffret, A., Mougenot, D., Kornprobst, J., Mergoil-Daniel, J. & Torrent, G. (1980). Ocean-continent boundary off the Iberian margin: a serpentinite diapir west of the Galicia Bank. *Earth and Planetary Science Letters* **48**(1), 23–34. https://doi.org/10.1016/0012-821X(80)90166-1.

Boillot, G., Féraud, G., Recq, M. & Girardeau, J. (1989). Undercrusting by serpentinite beneath rifted margins. *Nature* **341**(6242), 523–525. https://doi.org/10.1038/341523a0.

Bonatti, E. (1968). Ultramafic rocks from the mid-Atlantic ridge. *Nature* **219**(5152), 363–364. https://doi.org/10.1038/219363a0.

Bonatti, E. (1976). Serpentinite protrusions in the oceanic crust. *Earth and Planetary Science Letters*, **32**(2), 107–113.

Bousquet, R., Oberhänsli, R., Goffé, B., Wiederkehr, M., Koller, F., Schmid, S. M., Schuster, R., Engi, M., Berger, A. & Martinotti, G. (2008). Metamorphism of metasediments at the scale of an orogen: a key to the tertiary geodynamic evolution of the Alps. *Geological Society, London, Special Publications* **298**(1), 393–411. https://doi.org/10.1144/SP298.18.

Burkhard, D. J. & O'Neil, J. R. (1988). Contrasting serpentinization processes in the Eastern Central Alps. *Contributions to Mineralogy and Petrology* **99**(4), 498–506. https://doi.org/10.1007/BF00371940.

Cann, J. R., Blackman, D., Smith, D., McAllister, E., Janssen, B., Mello, S., Avgerinos, E., Pascoe, A. & Escartin, J. (1997). Corrugated slip surfaces formed at ridge-transform intersections on the Mid-Atlantic Ridge. *Nature* **385**(6614), 329–332. https://doi.org/10.1038/385329a0.

Cannat, M. (1993). Emplacement of mantle rocks in the seafloor at mid-ocean ridges. *Journal of Geophysical Research: Solid Earth* **98**(B3), 4163–4172. https://doi.org/10.1029/92JB02221.

Cannat, M., Manatschal, G., Sauter, D. & Peron-Pinvidic, G. (2009). Assessing the conditions of continental breakup at magma-poor rifted margins: what can we learn from slow spreading mid-ocean ridges? *Comptes Rendus Geoscience* **341**(5), 406–427. https://doi.org/10.1016/j.crte.2009.01.005.

Cannat, M., Sauter, D., Lavier, L., Bickert, M., Momoh, E. & Leroy, S. (2019). On spreading modes and magma supply at slow and ultraslow mid-ocean ridges. *Earth and Planetary Science Letters* **519**, 223–233. https://doi.org/10.1016/j.epsl.2019.05.012.

Chauvel, C., Bureau, S. & Poggi, C. (2011). Comprehensive chemical and isotopic analyses of basalt and sediment reference materials. *Geostandards and Geoanalytical Research* **35**(1), 125–143. https://doi.org/10.1111/j.1751-908X.2010.00086.x.

Christensen, N. I. (1972). The abundance of serpentinites in the oceanic crust. *The Journal of Geology* **80**(6), 709–719. https://doi.org/10.1086/627796.

Christensen, N. I. (2004). Serpentinites, peridotites, and seismology. *International Geology Review* **46**(9), 795–816. https://doi.org/10.2747/0020-6814.46.9.795.

Coltat, R., Branquet, Y., Gautier, P., Rodriguez, H. C., Poujol, M., Pelleter, E., McClenaghan, S., Manatschal, G. & Boulvais, P. (2019). Unravelling the root zone of ultramafic-hosted black smokers-like hydrothermalism from an Alpine analog. *Terra Nova* **31**, 549–561. https://doi.org/10.1111/ter.12427.

Coltat, R., Boulvais, P., Riegler, T., Pelleter, E. & Branquet, Y. (2021). Element distribution in the root zone of ultramafic-hosted black smoker-like systems: constraints from an Alpine analog. *Chemical Geology* **559**, 119916. https://doi.org/10.1016/j.chemgeo.2020.119916.

Compagnoni, R., Cossio, R. & Mellini, M. (2021). Raman anisotropy in serpentine minerals, with a caveat on identification. *Journal of Raman Spectroscopy* **52**(7), 1334–1345. https://doi.org/10.1002/jrs.6128.

Debret, B., Andreani, M., Godard, M., Nicollet, C., Schwartz, S. & Lafay, R. (2013). Trace element behavior during serpentinization/de-serpentinization of an eclogitized oceanic lithosphere: a LA-ICPMS study of the Lanzo ultramafic massif (Western Alps). *Chemical Geology* **357**, 117–133. https://doi.org/10.1016/j.chemgeo.2013.08.025.

Deschamps, F., Godard, M., Guillot, S., Chauvel, C., Andreani, M., Hattori, K., ... & France, L. (2012). *Behavior of fluid-mobile elements in serpentines from abyssal to subduction environments: Examples from Cuba and Dominican Republic. Chemical Geology*, **312**, 93–117.

Desmurs, L., Manatschal, G. & Bernoulli, D. (2001). The Steinmann Trinity revisited: mantle exhumation and magmatism along an ocean-continent transition: the Platta nappe, Eastern Switzerland. *Contributions to Mineralogy and Petrology* **144**, 365–382.

Dietrich, V. J. (1969) *Die Ophiolithe des Oberhalbsteins (Graubünden) und das Ophiolithmaterial der ostschweizerischen Molasseablagerungen: ein petrographischer*, Vergleich Doctoral dissertation. ETH Zurich.

Dietrich, V. (1970) Die Stratigraphie der Platta-Decke: Fazielle Zusammenhänge zwischen Oberpenninikum und Unterostalpin. In: *Geologisches Institut der Eidg. Technischen Hochschule und der Universität Zürich*.

Dilek, Y., Coulton, A. & Hurst, S. D. (1997) Serpentinization and hydrothermal veining in peridotites at site 920 in the Mark area. In: *Proceedings of the Ocean Drilling Program, 153 Scientific Results*. Ocean Drilling Program, pp.35–60.

Doebelin, N. & Kleeberg, R. (2015). Profex: a graphical user interface for the rietveld refinement program BGMN. *Journal of Applied Crystallography* **48**(5), 1573–1580. https://doi.org/10.1107/S1600576715014685.

Douville, E., Charlou, J. L., Oelkers, E. H., Bienvenu, P., Colon, C. F. J., Donval, J. P., Fouquet, Y., Prieur, D. & Appriou, P. (2002). The Rainbow vent fluids (36°14N, MAR): the influence of ultramafic rocks and phase separation on trace metal content in Mid-Atlantic Ridge hydro-thermal fluids. *Chemical Geology* **184**, 37–48. https://doi.org/10.1016/S0009-2541(01)00351-5.

Epin, M.-E. & Manatschal, G. (2018). Three-dimensional architecture, structural evolution, and role of inheritance controlling detachment faulting at a hyperextended distal margin: the example of the Err detachment system (SE Switzerland). *Tectonics* **37**(12), 4494–4514. https://doi.org/10.1029/2018TC005125.

Epin, M. E., Manatschal, G., Amman, M., Ribes, C., Clausse, A., Guffon, T. & Lescanne, M. (2019). Polyphase tectono-magmatic evolution during mantle exhumation in an ultra-distal, magma-poor rift domain: example of the fossil Platta ophiolite, SE Switzerland.

International Journal of Earth Sciences **108**, 2443–2467. https://doi.org/10.1007/s00531-019-01772-0.

Escartin, J., Hirth, G. & Evans, B. (1997). Effects of serpentinization on the lithospheric strength and the style of normal faulting at slow-spreading ridges. *Earth and Planetary Science Letters* **151**(3–4), 181–189. https://doi.org/10.1016/S0012-821X(97)81847-X.

Escartin, J., Hirth, G. & Evans, B. (2001). Strength of slightly serpentinized peridotites: implications for the tectonics of oceanic lithosphere. *Geology* **29**(11), 1023–1026. https://doi.org/10.1130/0091-7613(2001)029<1023:SOSSPI>2.0.CO;2.

Evans, B. W. (2004). The serpentinite multisystem revisited: chrysotile is metastable. *International Geology Review* **46**(6), 479–506. https://doi.org/10.2747/0020-6814.46.6.479.

Florineth, D. & Froitzheim, N. (1994) Transition from continental to oceanic basement in the Tasna Nappe: Evidence for Early Cretaceous opening of the Valais Ocean. *Schweizerische Mineralogische Und Petrographische Mitteilungen*, **74**, 437–448.

Frassi, C., Chighine, G., Mauro, D., Biagioni, C., Zaccarini, F. & Marroni, M. (2022). Pervasive crystallization of antigorite in northern apennine ophiolites: the example of Montecarelli peridotites (Tuscany, Central Italy). *Ofioliti* **47**(1).

Frey, M. & Ferreiro Mählmann, R. (1999). Alpine metamorphism of the Central Alps. *Schweizerische Mineralogische und Petrographische Mitteilungen* **79**(1), 135–154.

Froitzheim, N. & Manatschal, G. (1996). Kinematics of Jurassic rifting, mantle exhumation, and passive-margin formation in the Austroalpine and Penninic nappes (Eastern Switzerland). *Geological Society of America Bulletin* **108**(9), 1120–1133. https://doi.org/10.1130/0016-7606(1996)108<1120:KOJRME>2.3.CO;2.

Froitzheim, N. & Rubatto, D. (1998). Continental breakup by detachment faulting: field evidence and geochronological constraints (Tasna nappe, Switzerland). *Terra Nova* **10**(4), 171–176. https://doi.org/10.1046/j.1365-3121.1998.00187.x.

Froitzheim, N., Schmid, S. & Conti, P. (1994). Repeated change from crustal shortening to orogen-parallel extension in the Austroalpine units of Graubunden. *Eclogae Geologicae Helvetiae* **87**(2), 559–612.

Frost, B. R. & Beard, J. S. (2007). On silica activity and serpentinization. *Journal of Petrology* **48**(7), 1351–1368. https://doi.org/10.1093/petrology/egm021.

Früh-Green, G. L., Weissert, H. & Bernoulli, D. (1990). A multiple fluid history recorded in Alpine ophiolites. *Journal of the Geological Society* **147**(6), 959–970. https://doi.org/10.1144/gsjgs.147.6.0959.

Früh-Green, G. L., Plas, A. & Lécuyer, C. (1996) Petrologic and stable isotope constraints on hydrothermal alteration and serpentinization of the EPR shallow mantle at Hess Deep (Site 895). In: *Proceedings-Ocean Drilling Program, Scientific Results*, **47**, 255–292.

Früh-Green, G. L., Scambelluri, M. & Vallis, F. (2001). O–H isotope ratios of high pressure ultramafic rocks: implications for fluid sources and mobility in the subducted hydrous mantle. *Contributions to Mineralogy and Petrology* **141**(2), 145–159. https://doi.org/10.1007/s004100000228.

Früh-Green, G. L., Connolly, J. A., Plas, A., Kelley, D. S. & Grobéty, B. (2004). Serpentinization of oceanic peridotites: implications for geochemical cycles and biological activity. *The subseafloor biosphere at mid-ocean ridges* **144**, 119–136. https://doi.org/10.1029/144GM08.

Gillard, M., Autin, J. & Manatschal, G. (2016). Fault systems at hyperextended rifted margins and embryonic oceanic crust: structural style, evolution and relation to magma. *Marine and Petroleum Geology* **76**, 51–67. https://doi.org/10.1016/j.marpetgeo.2016.05.013.

Gillard, M., Tugend, J., Müntener, O., Manatschal, G., Karner, G. D., Autin, J., Sauter, D., Figueredo, P. H. & Ulrich, M. (2019). The role of serpentinization and magmatism in the formation of decoupling interfaces at magma-poor rifted margins. *Earth-Science Reviews* **196**, 102882. https://doi.org/10.1016/j.earscirev.2019.102882.

Govindaraju, K. (1982). Report (1967–1981) on four ANRT rock reference samples: diorite DR-N, serpentine UB-N, bauxite BX-N and disthene DT-N. *Geostandards Newsletter* **6**(1), 91–159. https://doi.org/10.1111/j.1751-908X.1982.tb00347.x.

Grauby, O., Baronnet, A., Devouard, B., Schoumacker, K. & Demirdjian, L. (1998) The chrysotile-polygonal serpentine-lizardite suite synthesized from a 3MgO-2SiO2-excess H2O gel. In: *The 7th International Symposium on Experimental Mineralogy, Petrology, and Geochemistry, Orléans, Abstracts. Terra Nova, supplement* **1**, 24.

Groppo, C., Rinaudo, C., Cairo, S., Gastaldi, D. & Compagnoni, R. (2006). Micro-raman spectroscopy for a quick and reliable identification of serpentine minerals from ultramafics. *European Journal of Mineralogy* **18**(3), 319–329. https://doi.org/10.1127/0935-1221/2006/0018-0319.

Guillong, M., Meier, D. L., Allan, M. M., Heinrich, C. A., Yardley, B. W. *et al.* (2008). Appendix a6: Sills: a Matlab-based program for the reduction of laser ablation ICP-MS data of homogeneous materials and inclusions. *Mineralogical Association of Canada Short Course* **40**, 328–333.

Hart, S. R. & Zindler, A. (1986). In search of a bulk-earth composition. *Chemical Geology* **57**(3–4), 247–267. https://doi.org/10.1016/0009-2541(86)90053-7.

Hébert, R., Constantin, M., Robinson, P. *et al.* (1991) Primary mineralogy of leg 118 gabbroic rocks and their place in the spectrum of oceanic mafic igneous rocks. In: *Proceedings of the Ocean Drilling Program, Scientific Results*, **118**, 3–20.

Hochscheid, F., Coltat, R., Ulrich, M., Munoz, M., Manatschal, G. & Boulvais, P. (2022). The Sr isotope geochemistry of oceanic ultramafic-hosted mineralizations. *Ore Geology Reviews* **144**, 104824. https://doi.org/10.1016/j.oregeorev.2022.104824.

Hopkinson, L., Beard, J. & Boulter, C. (2004). The hydrothermal plumbing of a serpentinite- hosted detachment: evidence from the West Iberia non-volcanic rifted continental margin. *Marine Geology* **204**(3–4), 301–315. https://doi.org/10.1016/S0025-3227(03)00374-8.

Jagoutz, E., Palme, H., Baddenhausen, H., Blum, K., Cendales, M., Dreibus, G., Spettel, B., Lorenz, V. & Wänke, H. (1979) The abundances of major, minor and trace elements in the earth's mantle as derived from primitive ultramafic nodules. In: *Lunar and Planetary Science Conference, 10th, Houston, 1979*, **10**, 2013–2050.

Janecky, D. & Seyfried, W. (1986). Hydrothermal serpentinization of peridotite within the oceanic crust: experimental investigations of mineralogy and major element chemistry. *Geochimica et Cosmochimica Acta* **50**(7), 1357–1378. https://doi.org/10.1016/0016-7037(86)90311-X.

Jarosewich, E., Nelen, J. & Norberg, J. A. (1980). Reference samples for electron microprobe analysis. *Geostandards Newsletter* **4**(1), 43–47. https://doi.org/10.1111/j.1751-908X.1980.tb00273.x.

Karson, J. A. & Rona, P. A. (1990). Block-tilting, transfer faults, and structural control of magmatic and hydrothermal processesin the tag area, Mid-Atlantic Ridge 26°N. *Geological Society of America Bulletin* **102**(12), 1635–1645. https://doi.org/10.1130/0016-7606(1990)102<1635:BTTFAS>2.3.CO;2.

Klein, F. & Roux, V. L. (2020). Quantifying the volume increase and chemical exchange during serpentinization. *Geology* **48**, 552–556. https://doi.org/10.1130/G47289.1.

Klein, F., Bach, W. & McCollom, T. M. (2013). Compositional controls on hydrogen generation during serpentinization

ultramafic rocks. *Lithos* **178**, 55–69. https://doi.org/10.1016/j.lithos.2013.03.008.

Klein, F., Marschall, H. R., Bowring, S. A., Humphris, S. E. & Horning, G. (2017). Mid-ocean ridge serpentinite in the Puerto Rico trench: from seafloor spreading to subduction. *Journal of Petrology* **58**(9), 1729–1754. https://doi.org/10.1093/petrology/egx071.

Klinkhammer, G., Elderfield, H., Edmond, J. & Mitra, A. (1994). Geochemical implications of rare earth element patterns in hydrothermal fluids from mid-ocean ridges. *Geochimica et Cosmochimica Acta* **58**(23), 5105–5113. https://doi.org/10.1016/0016-7037(94)90297-6.

Kodolányi, J. & Pettke, T. (2011). Loss of trace elements from serpentinites during fluid-assisted transformation of chrysotile to antigorite—an example from Guatemala. *Chemical Geology* **284**(3–4), 351–362. https://doi.org/10.1016/j.chemgeo.2011.03.016.

Kodolányi, J., Pettke, T., Spandler, C., Kamber, B. S. & Gméling, K. (2012). Geochemistry of ocean floor and fore-arc serpentinites: constraints on the ultramafic input to subduction zones. *Journal of Petrology* **53**(2), 235–270. https://doi.org/10.1093/petrology/egr058.

Lafay, R., Deschamps, F., Schwartz, S., Guillot, S., Godard, M., Debret, B. & Nicollet, C. (2013). High-pressure serpentinites, a trap-and-release system controlled by metamorphic conditions: example from the Piedmont zone of the Western Alps. *Chemical Geology* **343**, 38–54. https://doi.org/10.1016/j.chemgeo.2013.02.008.

Lafay, R., Baumgartner, L. P., Stephane, S., Suzanne, P., German, M.-H. & Torsten, V. (2017). Petrologic and stable isotopic studies of a fossil hydrothermal system in ultramafic environment (Chenaillet ophicalcites, Western Alps, France): processes of carbonate cementation. *Lithos* **294**, 319–338.

Lagabrielle, Y. & Bodinier, J.-L. (2008). Submarine reworking of exhumed subcontinental mantle rocks: field evidence from the lherz peridotites, french pyrenees. *Terra Nova* **20**(1), 11–21. https://doi.org/10.1111/j.1365-3121.2007.00781.x.

Lavier, L. L., Roger Buck, W. & Poliakov, A. N. (1999). Self-consistent rolling-hinge model for the evolution of large-offset low-angle normal faults. *Geology* **27**(12), 1127–1130. https://doi.org/10.1130/0091-7613(1999)027<1127:SCRHMF>2.3.CO;2.

Liu, W., Cao, Y., Zhang, J., Zhang, Y., Zong, K. & Jin, Z. (2020). Thermo-structural evolution of the Val Malenco (Italy) peridotite: a petrological, geochemical and microstructural study. *Minerals* **10**(11), 962. https://doi.org/10.3390/min10110962.

Manatschal, G. (2004). New models for evolution of magma-poor rifted margins based on a review of data and concepts from West Iberia and the Alps. *International Journal of Earth Sciences* **93**, 432–466.

Manatschal, G. & Müntener, O. (2009). A type sequence across an ancient magma-poor ocean-continent transition: the example of the Western Alpine Tethys ophiolites. *Tectonophysics* **473**(1–2), 4–19. https://doi.org/10.1016/j.tecto.2008.07.021.

Manatschal, G. & Nievergelt, P. (1997). A continent-ocean transition recorded in the Err and Platta nappes (Eastern Switzerland). *Eclogae Geologicae Helvetiae* **90**(1), 3–28.

Manatschal, G., Engström, A., Desmurs, L., Schaltegger, U., Cosca, M., Müntener, O. & Bernoulli, D. (2006). What is the tectono-metamorphic evolution of continental break-up: the example of the Tasna Ocean–Continent Transition. *Journal of Structural Geology* **28**(10), 1849–1869. https://doi.org/10.1016/j.jsg.2006.07.014.

Martin, B. & Fyfe, W. (1970). Some experimental and theoretical observations on the kinetics of hydration reactions with particular reference to serpentinization. *Chemical Geology* **6**, 185–202. https://doi.org/10.1016/0009-2541(70)90018-5.

Mellini, M., Trommsdorff, V. & Compagnoni, R. (1987). Antigorite polysomatism: behaviour during progressive metamorphism. *Contributions to Mineralogy and Petrology* **97**(2), 147–155. https://doi.org/10.1007/BF00371235.

Mellini, M., Rumori, C. & Viti, C. (2005). Hydrothermally reset magmatic spinels in retrograde serpentinites: formation of "ferritchromit" rims and chlorite aureoles. *Contributions to Mineralogy and Petrology* **149**, 266–275. https://doi.org/10.1007/s00410-005-0654-y.

Minshull, T. A. (2009). Geophysical characterisation of the ocean-continent transition at magma-poor rifted margins. *Comptes Rendus Geoscience* **341**(5), 382–393.

Morrow, C., Moore, D. E. & Lockner, D. (2000). The effect of mineral bond strength and adsorbed water on fault gouge frictional strength. *Geophysical Research Letters* **27**(6), 815–818. https://doi.org/10.1029/1999GL008401.

Müntener, O. & Piccardo, G. B. (2004). Melt migration in ophiolitic peridotites: the message from Alpine–Apennine peridotites and implications for embryonic ocean basins. *Geological Society Special Publication* **218**, 69–89.

Müntener, O., Pettke, T., Desmurs, L., Meier, M. & Schaltegger, U. (2004). Refertilization of mantle peridotite in embryonic ocean basins: trace element and Nd isotopic evidence and implications for crust-mantle relationships. *Earth and Planetary Science Letters* **221**(1–4), 293–308. https://doi.org/10.1016/S0012-821X(04)00073-1.

Müntener, O., Manatschal, G., Desmurs, L. & Pettke, T. (2010). Plagioclase peridotites in ocean- continent transitions: refertilized mantle domains generated by melt stagnation in the shallow mantle lithosphere. *Journal of Petrology* **51**(1–2), 255–294. https://doi.org/10.1093/petrology/egp087.

Nicholls, I., Ferguson, J., Jones, H., Marks, G. & Mutter, J. (1981). Ultramafic blocks from the ocean floor southwest of Australia. *Earth and Planetary Science Letters* **56**, 362–374. https://doi.org/10.1016/0012-821X(81)90140-0.

Normand, C., Williams-Jones, A. E., Martin, R. F. & Vali, H. (2002). Hydrothermal alteration of olivine in a flow-through autoclave: nucleation and growth of serpentine phases. *American Mineralogist* **87**(11–12), 1699–1709. https://doi.org/10.2138/am-2002-11-1220.

O'Hanley, D. S. (1992). Solution to the volume problem in serpentinization. *Geology* **20**(8), 705–708. https://doi.org/10.1130/0091-7613(1992)020<0705:STTVPI>2.3.CO;2.

Parnell-Turner, R., Sohn, R. A., Peirce, C., Reston, T. J., MacLeod, C. J., Searle, R. C. & Simão, N. M. (2017). Oceanic detachment faults generate compression in extension. *Geology* **45**(10), 923–926. https://doi.org/10.1130/G39232.1.

Paulick, H., Bach, W., Godard, M., De Hoog, J., Suhr, G. & Harvey, J. (2006). Geochemistry of abyssal peridotites (Mid-Atlantic Ridge, 15°N, ODP leg 209): implications for fluid/rock interaction in slow spreading environments. *Chemical Geology* **234**(3–4), 179–210. https://doi.org/10.1016/j.chemgeo.2006.04.011.

Pearce, N. J., Perkins, W. T., Westgate, J. A., Gorton, M. P., Jackson, S. E., Neal, C. R. & Chenery, S. P. (1997). A compilation of new and published major and trace element data for NIST SRM 610 and NIST SRM 612 glass reference materials. *Geostandards Newsletter* **21**(1), 115–144. https://doi.org/10.1111/j.1751-908X.1997.tb00538.x.

Peters, T. (1965). A water-bearing andradite from the Totalp serpentine (Davos, Switzerland). *American Mineralogist: Journal of Earth and Planetary Materials* **50**(9), 1482–1486.

Peters, P. C. & Mathews, J. (1963). Gravitational radiation from point masses in a keplerian orbit. *Physical Review* **131**(1), 435–440. https://doi.org/10.1103/PhysRev.131.435.

Peters, T. & Stettler, A. (1987a). Radiometric age, thermobarometry and mode of emplacement of the Totalp peridotite in the Eastern Swiss Alps. *Schweizerische Mineralogische und Petrographische Mitteilungen* **67**(3), 285–294.

Peters, T. & Stettler, A. (1987b). Time, physico-chemical conditions, mode of emplacement and geologic setting of the Totalp peridotite in the Eastern Swiss Alps. *Schweizerische Mineralogische und Petrographische Mitteilungen* **67**, 285–294.

Peters, D., Bretscher, A., John, T., Scambelluri, M., & Pettke, T. (2017). Fluid-mobile elements in serpentinites: Constraints on serpentinisation environments and element cycling in subduction zones. *Chemical geology*, **466**, 654–666.

Pettke, T. & Bretscher, A. (2022). Fluid-mediated element cycling in subducted oceanic lithosphere: the orogenic serpentinite perspective. *Earth-Science Reviews* **225**, 103896. https://doi.org/10.1016/j.earscirev.2021.103896.

Pettke, T., Oberli, F., Audétat, A., Guillong, M., Simon, A. C., Hanley, J. J. & Klemm, L. M. (2012). Recent developments in element concentration and isotope ratio analysis of individual fluid inclusions by laser ablation single and multiple collector icp-ms. *Ore Geology Reviews* **44**, 10–38. https://doi.org/10.1016/j.oregeorev.2011.11.001.

Picazo, S., Manatschal, G., Cannat, M. & Andréani, M. (2013). Deformation associated to exhumation of serpentinized mantle rocks in a fossil Ocean Continent Transition: the Totalp unit in SE Switzerland. *Lithos* **175**, 255–271.

Picazo, S., Müntener, O., Manatschal, G., Bauville, A., Karner, G. & Johnson, C. (2016). Mapping the nature of mantle domains in Western and Central Europe based on clinopyroxene and spinel chemistry: evidence for mantle modification during an extensional cycle. *Lithos* **266-267**, 233–263. https://doi.org/10.1016/j.lithos.2016.08.029.

Piccardo, G. B. (2013). Subduction of a fossil slow–ultraslow spreading ocean: a petrology-constrained geodynamic model based on the Voltri Massif, Ligurian Alps, Northwest Italy. *International Geology Review* **55**(7), 787–803. https://doi.org/10.1080/00206814.2012.746806.

Plümper, O., Beinlich, A., Bach, W., Janots, E. & Austrheim, H. (2014). Garnets within geode-like serpentinite veins: implications for element transport, hydrogen production and life-supporting environment formation. *Geochimica et Cosmochimica Acta* **141**, 454–471. https://doi.org/10.1016/j.gca.2014.07.002.

Raleigh, C. & Paterson, M. (1965). Experimental deformation of serpentinite and its tectonic implications. *Journal of Geophysical Research* **70**(16), 3965–3985. https://doi.org/10.1029/JZ070i016p03965.

Rampone, E., Hofmann, A. W. & Raczek, I. (1998). Isotopic contrasts within the internal Liguride Ophiolite (N. Italy): the lack of a genetic mantle-crust link. *Earth and Planetary Science Letters* **163**, 175–189. https://doi.org/10.1016/S0012-821X(98)00185-X.

Rampone, E., Borghini, G. & Basch, V. (2020). Melt migration and melt-rock reaction in the Alpine-Apennine peridotites: insights on mantle dynamics in extending lithosphere. *Geoscience Frontiers* **11**(1), 151–166. https://doi.org/10.1016/j.gsf.2018.11.001.

Ramsay, J. G. (1980). The crack-seal mechanism of rock deformation. *Nature* **284**(5752), 135–139. https://doi.org/10.1038/284135a0.

Reinen, L. A., Weeks, J. D. & Tullis, T. E. (1994). The frictional behavior of lizardite and antigorite serpentinites: experiments, constitutive models, and implications for natural faults. *Pure and Applied Geophysics* **143**, 317–358. https://doi.org/10.1007/BF00874334.

Reston, T. (2018). Flipping detachments: the kinematics of ultraslow spreading ridges. *Earth and Planetary Science Letters* **503**, 144–157. https://doi.org/10.1016/j.epsl.2018.09.032.

Reston, T. J. & McDermott, K. G. (2011). Successive detachment faults and mantle unroofing at magma-poor rifted margins. *Geology* **39**(11), 1071–1074. https://doi.org/10.1130/G32428.1.

Ribeiro Da Costa, I., Barriga, F. J., Viti, C., Mellini, M. & Wicks, F. J. (2008). Antigorite in deformed serpentinites from the Mid-Atlantic Ridge. *European Journal of Mineralogy* **20**(4), 563–572. https://doi.org/10.1127/0935-1221/2008/0020-1808.

Ribes, C., Petri, B., Ghienne, J.-F., Manatschal, G., Galster, F., Karner, G. D., Figueredo, P. H., Johnson, C. A. & Karpoff, A.-M. (2020). Tectono-sedimentary evolution of a fossil ocean-continent transition: Tasna nappe, Central Alps (SE Switzerland). *GSA Bulletin* **132**(7–8), 1427–1446. https://doi.org/10.1130/B35310.1.

Rimstidt, J. D., Brantley, S. L. & Olsen, A. A. (2012). Systematic review of forsterite dissolution rate data. *Geochimica et Cosmochimica Acta* **99**, 159–178. https://doi.org/10.1016/j.gca.2012.09.019.

Rouméjon, S. & Cannat, M. (2014). Serpentinization of mantle-derived peridotites at mid- ocean ridges: mesh texture development in the context of tectonic exhumation. *Geochemistry, Geophysics, Geosystems* **15**(6), 2354–2379. https://doi.org/10.1002/2013GC005148.

Rouméjon, S., Cannat, M., Agrinier, P., Godard, M. & Andreani, M. (2015). Serpentinization and fluid pathways in tectonically exhumed peridotites from the Southwest Indian Ridge (62–65 E). *Journal of Petrology* **56**(4), 703–734. https://doi.org/10.1093/petrology/egv014.

Rouméjon, S., Williams, M. J. & Früh-Green, G. L. (2018). In-situ oxygen isotope analyses in serpentine minerals: constraints on serpentinization during tectonic exhumation at slow-and ultraslow-spreading ridges. *Lithos* **323**, 156–173. https://doi.org/10.1016/j.lithos.2018.09.021.

Rouméjon, S., Andreani, M. & Früh-Green, G. L. (2019). Antigorite crystallization during oceanic retrograde serpentinization of abyssal peridotites. *Contributions to Mineralogy and Petrology* **174**(7), 1–25.

Salters, V. J. & Stracke, A. (2004). Composition of the depleted mantle. *Geochemistry, Geophysics, Geosystems* **5**(5). https://doi.org/10.1029/2003GC000597.

Sandiford, D., Brune, S., Glerum, A., Naliboff, J. & Whittaker, J. M. (2021). Kinematics of foot-wall exhumation at oceanic detachment faults: solid-block rotation and apparent unbending. *Geochemistry, Geophysics, Geosystems* **22**(4), e2021GC009681. https://doi.org/10.1029/2021GC009681.

Sauter, D., Cannat, M., Rouméjon, S., Andreani, M., Birot, D., Bronner, A., Brunelli, D., Carlut, J., Delacour, A., Guyader, V., MacLeod, C. J., Manatschal, G., Mendel, V., Ménez, B., Pasini, V., Ruellan, E. & Searle, R. (2013). Continuous exhumation of mantle-derived rocks at the Southwest Indian Ridge for 11 million years. *Nature Geoscience* **6**(4), 314–320. https://doi.org/10.1038/ngeo1771.

Scambelluri, M., Muïntener, O., Hermann, J., Piccardo, G. B., & Trommsdorff, V. (1995). Subduction of water into the mantle: history of an Alpine peridotite. *Geology*, **23**(5), 459–462.

Schaltegger, U., Desmurs, L., Manatschal, G., Müntener, O., Meier, M., Frank, M. & Bernoulli, D. (2002). The transition from rifting to sea-floor spreading within a magma-poor rifted margin: field and isotopic constraints. *Terra Nova* **14**(3), 156–162. https://doi.org/10.1046/j.1365-3121.2002.00406.x.

Schwartz, S., Guillot, S., Reynard, B., Lafay, R., Debret, B., Nicollet, C., Lanari, P. & Auzende, A. L. (2013). Pressure-temperature estimates of the lizardite/antigorite transition in high pressure serpentinites. *Lithos* **178**, 197–210. https://doi.org/10.1016/j.lithos.2012.11.023.

Schwarzenbach, E. M., Früh-Green, G. L., Bernasconi, S. M., Alt, J. C. & Plas, A. (2013). Serpentinization and carbon sequestration:

a study of two ancient peridotite-hosted hydrothermal systems. *Chemical Geology* **351**, 115–133. https://doi.org/10.1016/j.chemgeo.2013.05.016.

Schwarzenbach, E. M., Caddick, M. J., Beard, J. S. & Bodnar, R. J. (2016). Serpentinization, element transfer, and the progressive development of zoning in veins: evidence from a partially serpentinized harzburgite. *Contributions to Mineralogy and Petrology* **171**, 1–22.

Schwarzenbach, E. M., Vogel, M., Früh-Green, G. L. & Boschi, C. (2021). Serpentinization, carbonation, and metasomatism of ultramafic sequences in the northern Apennine Ophiolite (NW Italy). *Journal of Geophysical Research: Solid Earth* **126**.

Smith, D. K., Cann, J. R. & Escartín, J. (2006). Widespread active detachment faulting and core complex formation near 13 N on the Mid-Atlantic Ridge. *Nature* **442**(7101), 440–443. https://doi.org/10.1038/nature04950.

Tarling, M. S., Rooney, J. S., Viti, C., Smith, S. A. & Gordon, K. C. (2018). Distinguishing the Raman spectrum of polygonal serpentine. *Journal of Raman Spectroscopy* **49**(12), 1978–1984. https://doi.org/10.1002/jrs.5475.

Tarling, M. S., Smith, S. A., Rooney, J. S., Viti, C. & Gordon, K. C. (2021). A common type of mineralogical banding in serpentine crack-seal veins. *Earth and Planetary Science Letters* **564**, 116930. https://doi.org/10.1016/j.epsl.2021.116930.

Theunissen, T. & Huismans, R. S. (2022). Mantle exhumation at magma-poor rifted margins controlled by frictional shear zones. *Nature Communications* **13**(1), 1–12.

Tichadou, C., Godard, M., Muñoz, M., Labaume, P., Vauchez, A., Gaucher, E. C. & Calassou, S. (2021). Mineralogical and geochemical study of serpentinized peridotites from the North-Western Pyrenees: new insights on serpentinization along magma-poor continental passive margins. *Lithos* **406-407**, 106521. https://doi.org/10.1016/j.lithos.2021.106521.

Trommsdorff, V. (1983). Metamorphose magnesiumreicher Gesteine: kristallischer Vergleich von Natur, experiment und thermodynamischer Datenbasis. *Fortschritte der Mineralogie* **61**(2), 283–308.

Trommsdorff, V. & BW, E. (1974) Alpine metamorphism of peridotitic rocks. *Schweizerische Mineralogische und Petrologische Mitteilungen*, **54**, 333–352.

Trommsdorff, V. & Evans, B. W. (1977). Antigorite-ophicarbonates: contact metamorphism in valmalenco, Italy. *Contributions to Mineralogy and Petrology* **62**(3), 301–312. https://doi.org/10.1007/BF00371017.

Trümpy, R. & Dössegger, R. (1972) Permian o f Switzerland. In: *Rotliegend, Essays on European Lower Permian. International sedimentary petrographical series* **15**, 189–215.

Ulmer, P. & Trommsdorff, V. (1995). Serpentine stability to mantle depths and subduction-related magmatism. *Science* **268**(5212), 858–861. https://doi.org/10.1126/science.268.5212.858.

Ulrich, M., Muñoz, M., Boulvais, P., Cathelineau, M., Cluzel, D., Guillot, S. & Picard, C. (2020). Serpentinization of New Caledonia peridotites: from depth to (sub-)surface. *Contributions to Mineralogy and Petrology* **175**(9), 1–25.

Vesin, C., Rubatto, D., Pettke, T. & Deloule, E. (2023). Multistage hydration during oceanic serpentinisation revealed by in situ oxygen isotope and trace element analyses. *Geochimica et Cosmochimica Acta* **355**, 13–31. https://doi.org/10.1016/j.gca.2023.06.032.

Vesin, C., Rubatto, D. & Pettke, T. (2024). The history of serpentinisation at mid-ocean ridges: insights from in situ trace elements coupled with oxygen and boron isotopes. *Chemical Geology* **654**, 122060. https://doi.org/10.1016/j.chemgeo.2024.122060.

Vils, F., Müntener, O., Kalt, A. & Ludwig, T. (2011). Implications of the serpentine phase transition on the behaviour of beryllium and lithium-boron of subducted ultramafic rocks. *Geochimica et Cosmochimica Acta* **75**(5), 1249–1271. https://doi.org/10.1016/j.gca.2010.12.007.

Viti, C. & Mellini, M. (1997). Contrasting chemical compositions in associated lizardite and chrysotile in veins from Elba. *European Journal of Mineralogy* **9**(3), 585–596. https://doi.org/10.1127/ejm/9/3/0585.

Weissert, B. J. H. & Bernoulli, D. (1985). A transform margin in the Mesozoic Tethys: evidence from the Swiss Alps. *Geologische Rundschau* **74**, 665–679. https://doi.org/10.1007/BF01821220.

Whitmarsh, R., Manatschal, G. & Minshull, T. (2001). Evolution of magma-poor continental margins from rifting to seafloor spreading. *Nature* **413**(6852), 150–154. https://doi.org/10.1038/35093085.

Wicks, F. J. & Whittaker, E. (1977). Serpentine textures and serpentinization. *The Canadian Mineralogist* **15**(4), 459–488.

Wunder, B. & Schreyer, W. (1997). Antigorite: high-pressure stability in the system MgO–SiO2–H2O (MSH). *Lithos* **41**(1–3), 213–227. https://doi.org/10.1016/S0024-4937(97)82013-0.

Deltech Furnaces

Sustained operating temperatures to 1800° Celsius

www.deltechfurnaces.com

Gas Mixing System

An ISO 9001:2015 certified company

Custom Vertical Tube

ASME NQA-1 2008 Nuclear Quality Assurance

Standard Vertical Tube

Control systems are certified by Intertek UL508A compliant

Bottom Loading Vertical Tube